uOttawa

L'Université canadienne
Canada's university

FACULTÉ DES ÉTUDES SUPÉRIEURES ET POSTOCTORALES

uOttawa

L'Université canadienne
Canada's university

FACULTY OF GRADUATE AND POSDOCTORAL STUDIES

Kai Zhou

AUTEUR DE LA THÈSE / AUTHOR OF THESIS

M.A.Sc. (Civil Engineering)

GRADE / DEGREE

Department of Civil Engineering

FACULTÉ, ÉCOLE, DÉPARTEMENT / FACULTY, SCHOOL, DEPARTMENT

Models for Predicting Corrosion-Induced Cracking, Spalling/Delamination of Rehabilitated Bridge Decks

TITRE DE LA THÈSE / TITLE OF THESIS

Beatriz Martin-Perez

DIRECTEUR (DIRECTRICE) DE LA THÈSE / THESIS SUPERVISOR

CO-DIRECTEUR (CO-DIRECTRICE) DE LA THÈSE / THESIS CO-SUPERVISOR

EXAMINATEURS (EXAMINATRICES) DE LA THÈSE / THESIS EXAMINERS

Burkan Isgor

Dan Palermo

Murat Saatcioglu

Gary W. Slater

LE DOYEN DE LA FACULTÉ DES ÉTUDES SUPÉRIEURES ET POSTDOCTORALES /
DEAN OF THE FACULTY OF GRADUATE AND POSTDOCORAL STUDIES

MODELS FOR PREDICTING CORROSION-INDUCED CRACKING, SPALLING/DELAMINATION OF REHABILITATED RC BRIDGE DECKS

By

Kai Zhou

A thesis

Presented to the University of Ottawa in fulfillment of the requirements for

Master of Applied Science in Civil Engineering

Department of Civil Engineering

University of Ottawa

Ottawa, Canada

K1N 6N5

April 2005

Your file Votre référence
ISBN: 0-494-11480-0
Our file Notre référence
ISBN: 0-494-11480-0

To My parents and my sister

Acknowledgement

My special appreciation goes to Dr. Beatriz Martin-Pèrez for her advice and direction throughout this research.

I would like to express my sincere gratitude to Dr. Magdi Mohareb and Dr. Hiroshi Tanaka for their help.

My deepest thanks go to my parents and my sister, for their tireless support and encouragement during my study.

I would like to extend my appreciation to Ms. Shiyan Tang and Mr. Xiaoping Tian for their presence whenever I needed help.

Abstract

The corrosion of reinforcing steel in reinforced concrete (rc) bridge decks due to the application of de-icing salts in winter has been recognized as one of the major causes of highway bridge deterioration in North America. Corrosion-induced damage is usually manifested by longitudinal cracking, spalling, and/or delamination of the concrete cover due to the expansion of corrosion products accumulating around the reinforcement. This damage leads to loss or reduction of serviceability, safety, and service life of rc bridge decks. This research presents an analytical model that describes the mechanism of damage initiation and accumulation to predict corrosion-induced cracking, spalling and delamination of rc bridge decks. This model assumed the concrete deck cover acts as a thick-wall cylinder subjected to a uniform internal pressure due to the expansion of corrosion products. The prediction of the damage caused by corroding reinforcing bars was established by calculating the induced stresses in the surrounding concrete. Corrosion-induced damage of rc bridge decks was also investigated using the finite element method. For this purpose, the commercial finite element package ABAQUS/Standard was used (Hibbit Karlsson & Sorensen Inc. 2004). The finite element analysis was to simulate three main failure modes of corrosion-induced damage of rc bridge decks: longitudinal cracking, delamination and spalling of the concrete. In this study, a finite element model that was independent to parameters defining boundary locations was used. Based on this model, parametric investigations of the influence of various design variables on the concrete deck failure modes were conducted for both unprotected and overlaid rc bridge decks. Finally, propagation models were proposed by comparing the analytical models with the results obtained from the finite element modelling. These propagation models are formulated by correcting the analytical models with factors obtained from the comparison of both sets of results.

Contents

List of Figures

List of Tables

Notation

a	The distance from the center of the rebar to the constrained edge
c	Concrete cover thickness
d	Rebar diameter
E_c	The elastic modulus of concrete
e	The crack penetration length
f'_t	The tensile strength of concrete
G_f	Fracture energy of concrete
j_r	The rate of rust production per unit area
L_1	The length of vertical direction correspond to paths 1
L_2	The length of 45°-direction measured from the horizontal correspond to paths 2
L_3	The length of horizontal direction correspond to paths 3
m_r	The mass of hydrated red rust formed per unit length of rebar
m_s	The mass of steel consumed in the corrosion process
n	The number of integration points in the element
p	The first stresses invariants defined in ABAQUS
q	The second stresses invariants defined in ABAQUS
$\overline{p}$	Effective hydrostatic pressure in ABAQUS
$\overline{q}$	Effective Mises equivalent deviatoric stress in ABAQUS
p_e	The pressure acting at the inner surface of the uncracked ring
p_i	Internal pressure
r	Radius of the concrete ring where stresses are being calculated
s	The rebar spacing
t	The overlay thickness
t_i	The time to onset of corrosion
t_p	The time elapsed since corrosion initiation
t_1	The time at which corrosion would produce crack initiation
t_2	The time at which corrosion would produce longitudinal cracking
t_3	The time at which corrosion would produce spalling of the deck cover

t_4	The time at which corrosion would produce delamination of the deck cover
u	Radial displacement
V	The volume of the structure
V_i	The volume associated with each integration point
α_f	An empirical coefficient that depends on the maximum aggregate size
Δd	The increase in rebar diameter due to corrosion build-up
Δd_1	The increase in rebar diameter due to corrosion build-up at crack initiation
Δd_2	The increase in rebar diameter to cause longitudinal cracking
Δd_3	The increase in rebar diameter to cause spalling of the concrete cover
Δd_4	The increase in rebar diameter to cause delamination of the concrete cover
ΔV	The increase in volume per unit length of rebar due to corrosion
$\delta \mathbf{D}$	The virtual rate of deformation tensor
$\delta \mathbf{D}_i$	The virtual tensor rate of deformation tensor at each integration points
$\tilde{\varepsilon}_t^{pl}$	Hardening variables in ABAQUS
$\tilde{\varepsilon}_c^{pl}$	Hardening variables in ABAQUS
λ_c	Hardening parameters in ABAQUS
λ_t	Hardening parameters in ABAQUS
ν	Poisson's ratio of concrete
ρ_s	The density of steel
ρ_r	The density of hydrated red rust
σ_r	Radial stress in concrete, always compressive
σ_t	Tangential stress in concrete, always tensile
$\boldsymbol{\sigma}$	The stress tensor
$\boldsymbol{\sigma}_i$	The stress tensor rate of deformation tensor at each integration points

Chapter 1

Introduction

1.1 Background

In recent years, corrosion of reinforcing bars in reinforced concrete (rc) bridge decks due to the application of de-icing salts in winter has been recognized as one of the major causes of highway bridge deterioration in North America. In reaction to this trend, there has been an enormous research effort to investigate and model the damage of rc bridge decks induced by the corrosion build-up around the reinforced bars.

Corrosion build-up is produced as a result of steel corrosion products occupying a volume 4 to 5 times that of the original steel. This expansion can cause tensile forces in the surrounding concrete. Since concrete is relatively weak in tension, cracks soon develop around the surfaces of the reinforcing bars. Cracking exposes the steel to even more chlorides, oxygen, carbon dioxide, and moisture and the corrosion process accelerates. As corrosion continues, spalling or delamination of the concrete cover can occur (See Figure 1.1). Delamination is the separation of the concrete cover which usually occurs along a plane parallel to the concrete surface. Delaminations are usually located at, or near the level of the corroding mat. As the process worsens concrete chunks eventually break away or spall off.

Over the past few decades, various methods for protection, repair and rehabilitation for corrosion damaged rc bridge decks have been developed. Among theses methods, overlay is one of the most commonly used ones, and this paper is focused on this method. Depending on the amount and type of damaged and contaminated concrete removed, an overlay can be classified as either a repair method or a rehabilitation method. Repair methods are used to restore a bridge deck to an acceptable level of service. They do not address the causes of deterioration but only their symptoms (spalls, cracks), and thus do not stop or reduce the rate of damage accumulation. On the other hand, rehabilitation methods are used to restore a bridge deck to an acceptable level of service and mitigate or stop the deterioration process to extend the service life of the deck. They address both the symptoms and the causes of the deterioration.

The most used overlay systems are latex modified concrete (LMC), low-slump dense concrete (LSDC), microsilica concrete (MSC), and hot-mix asphaltic concrete with a preformed membrane (HMAM). The LMC overlay is a concrete that has been modified by addition of latex, which makes the concrete relatively impermeable to chlorides. The LSDC consists of a dense and dry concrete mixed with a maximum water-cement ratio of 0.35 and a cement content of 490 kg/m^3. MSC is a low permeability concrete and contains 7% to 12% of microsilica by weight of concrete.

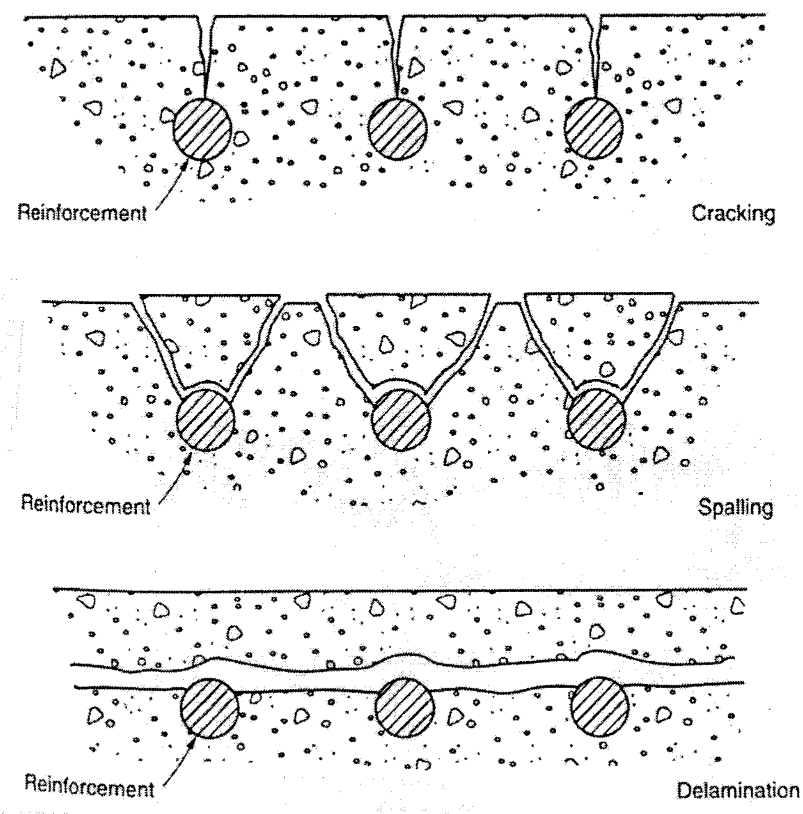

Figure 1.1: Corrosion-induced damage of the rc bridge deck (reproduced from Neville, 1995)

1.2 Objectives and scope of the study

Although there have been a lot of researches on the initiation and mechanism of corrosion, there has not been much on the effect of corrosion on structural damage, especially modeling the mechanics of the problem. The objective of this study was to present, discuss and evaluate the different failure mechanisms of reinforced concrete bridge decks due to corrosion of the reinforcing bars. An analytical model to describe the mechanics of the problem was proposed, and results were compared to finite element simulation of the problem using the commercially available finite element package ABAQUS. It was aimed in this thesis to establish the relation between the different failure mechanisms (cracking initiation, longitudinal cracking, and delamination and spalling) and the different geometries and configurations of the reinforcing bars in the concrete cover of the bridge deck. Design variables used in the analysis were the diameter of the reinforcing bar d, the cover of the reinforcing bar c, and the spacing between reinforcing bar s. Numerical simulations of a repaired reinforced concrete bridge deck repaired with an overlay were also carried out.

A parametric study was then conducted to investigate the influence of the modulus of elasticity of concrete cover E_c, the uniaxial compressive strength of concrete f_c', the ratio of the clear concrete cover to the rebar diameter c/d, and the spacing of the rebars s on the levels of the corrosion build-up necessary to cause cracking initiation, longitudinal cracking, delamination and spalling of the reinforced concrete bridge deck.

Finally, propagation models were proposed by comparing the analytical models with the results obtained from the finite element modelling. These propagation models are formulated by correcting the analytical models with factors obtained from the comparison of both sets of results. All of these analysis were assumed as time-independent.

1.3 Organization of the report

Chapter 2 presents a brief summary of concrete cracking models, with a more detailed description more on the smeared cracking model. Then a review of numerical models to simulate corrosion-induced damage of rc bridge decks is presented.

Chapter 3 presents the analytical model to simulate corrosion-induced damage of the reinforced concrete bridge deck. This chapter describes the basic assumptions of the analytical model and the analytical solution for predicting the values of corrosion build-up corresponding to cracking initiation, longitudinal cracking, delamination, and spalling. A limiting criterion between spalling and delamination is provided.

Chapter 4 presents the finite model used to model the corrosion-induced damage of the reinforced concrete bridge deck. This chapter describes two constitutive models for plain concrete available in ABAQUS/STANDARD, and introduces the choice of a finite element mesh that is independent to the constrain parameters. The finite element model is used to establish the different failure mechanisms of unprotected rc bridge decks with different geometries and configurations.

A parametric study conducted to investigate the influence of several design variables is presented in Chapter 5. This section presents the results from a parametric study conducted using the finite element model for an unprotected rc bridge deck subjected to reinforcement corrosion. The parametric study was carried out to establish the different corrosion-induced failure patterns as a function of design variables c, d, and s.

In Chapter 6, the effect of rehabilitating an rc bridge deck with an overlay on the corrosion-induced damage of the concrete cover is studied through the use of the finite element model presented in Chapter 4.

In Chapter 7, a comparison of the values of corrosion build-up causing cracking initiation, longitudinal cracking, spalling and delamination of rc bridge decks obtained by the analytical models presented in Chapter 3 and the finite element analyses presented in Chapter 5 and 6 is made. This comparison is presented in the form of simple models for prediction of corrosion-induced crack initiation, longitudinal cracking, spalling, and delamination of the concrete bridge deck cover. These models have been formulated by modifying the analytical models developed in Chapter 3 with correction factors. These factors were obtained by comparing the results from the analytical models for each of the corrosion-induced failure modes with those from the finite element analyses.

Finally, conclusions and recommendations for future work are discussed in Chapter 8.

Chapter 2

Literature review

2.1 Introduction

Corrosion-induced damage in reinforced concrete (rc) structures is usually manifested by rust-staining of the surface and cracking, delamination and/or spalling of the concrete cover. The transformation of metallic iron into corrosion products is accompanied by an increase in volume due to the lower density of iron oxides compared to that of the iron metal itself. Depending on the oxidation state, iron can expand as much as six times its original volume (Rosenberg et al., 1989). This increase in volume exerts tensile stresses in the concrete surrounding the rebars, and when these stresses exceed the concrete tensile strength, cracking and spalling of the concrete cover occur. The main corrosion-induced damage mechanisms in rc as illustrated in Figure 2.1 are:

- Decrease in the rebar cross-sectional area;
- Possible loss of steel ductility;
- Cracking, delamination, and spalling of the concrete cover;
- Loss of bond along the steel/concrete interface;
- Reduction in stiffness and strength; and,
- Possible change of failure mechanism.

This chapter reviews existing models used to predict corrosion-induced cracking, spalling and delamination of the concrete cover of rc bridge decks. Since modelling corrosion-induced damage requires modelling the initiation and propagation of cracks through the concrete cover of the bridge deck, Section 2.2 presents a summary of widely accepted approaches to model cracking in concrete, with a more detailed description on the smeared cracking approach. Sections 2.3 and 2.4

present respectively analytical and numerical models that simulate concrete damage due to corrosion build-up around the reinforcement. Most of the models found in the literature have focused on unrepaired rc structures reinforced with conventional mild steel. However, there are few models that have been developed for rehabilitated concrete structures, and these are presented in Section 2.5.

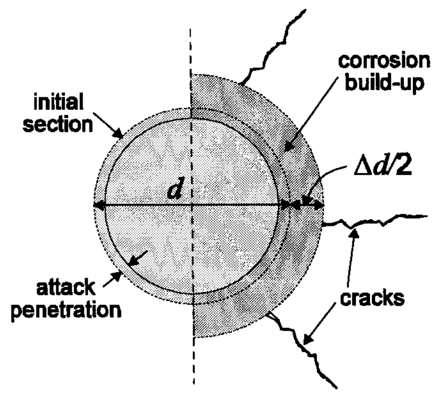

Figure 2.1: Consequences of rebar corrosion

2.2 Cracking models for concrete

2.2.1 Introduction

There are 3 main approaches for modeling cracking in concrete:

1. Discrete crack models (Ngo and Scordelis, 1967)
2. Smeared crack models (Rashid, 1968)
3. Lattice models (van Mier, 1991; Schlangen, 1993)

The third method was originally devised by physicists (Herrmann et al., 1989), where the continuum is replaced *a priori* by lattices of truss or beam elements. Subsequently, the microstructure of the material can be mapped onto these beam elements by assigning them different properties, depending on whether the truss or beam element represents a grain or mortar. This is a new developing method.

In the first type of models, cracking is assumed to occur as soon as the nodal force that is normal to the element boundaries exceeds the maximum tensile force that can be sustained. New degrees-of-freedom at the node location are created and a geometrical discontinuity is assumed to occur between the old node and the newly created node. Pre-defined cracks (Nilson, 1968) and discrete cracks established during the analysis (Mufti et al., 1970) are used to represent cracks in rc. The need to change the topology of the finite element mesh in this method greatly restricts the ease and speed of its use in analysis.

The need for models offering automatic generation of cracks without redefining the topology of the finite element mesh led to the creation of the second method, which images the cracked region to remain a continuum but switches its initial isotropic stress-strain relation to an orthotropic stress-strain relation. As a consequence, the topology of the original finite element mesh is preserved. This is computationally very efficient, and it is for this reason that the second method has come into wide use. This study will focus on the second method to model cracked concrete, extending it also to repaired rc.

2.2.2 Smeared cracking models

The smeared crack approach can be classified into 3 kinds of models:

1. Fixed-crack models
2. Rotating-crack models
3. Multiple crack models

Fixed-crack concrete models

Prior to cracking, concrete can be modeled sufficiently accurately as an isotropic, linear-elastic material. For instance, in a two-dimensional state of plane stress, we have:

$$\begin{Bmatrix} \sigma_{xx} \\ \sigma_{yy} \\ \sigma_{xy} \end{Bmatrix} = \frac{E}{1-\nu^2} \begin{bmatrix} 1 & \nu & 0 \\ \nu & \nu & 0 \\ 0 & 0 & 0.5(1-\nu) \end{bmatrix} \begin{Bmatrix} \varepsilon_{xx} \\ \varepsilon_{yy} \\ \gamma_{xy} \end{Bmatrix} \qquad (2.1)$$

where E is Young's modulus and ν is Poisson's ratio.

When the major principal tensile stress exceeds the tensile strength (i.e. tension cut-off criterion is reached), a fixed crack is initiated perpendicular to the direction of principal stress. The isotropic stress-strain law is replaced by an orthotropic law with the fixed *n,s*-axes of orthotropy, *n* is the direction normal to the crack (Mode-I) and *s* refers to the direction tangential to the crack (Mode-II). In a first attempt the orthotropic relation can be defined as (Rashid 1968):

$$\begin{Bmatrix} \sigma_{nn} \\ \sigma_{ss} \\ \sigma_{ns} \end{Bmatrix} = \begin{bmatrix} 0 & 0 & 0 \\ 0 & E & 0 \\ 0 & 0 & 0 \end{bmatrix} \begin{Bmatrix} \varepsilon_{nn} \\ \varepsilon_{ss} \\ \gamma_{ns} \end{Bmatrix} \tag{2.2}$$

where the orthotropic stress-strain relation has been set up in the coordinate system that aligns with the axes of orthotropy (Figure 2.2). Equation (2.2) shows that both the normal stiffness and the shear stiffness across the crack are set equal to zero upon cracking. As a consequence all effects of lateral contraction/expansion disappear.

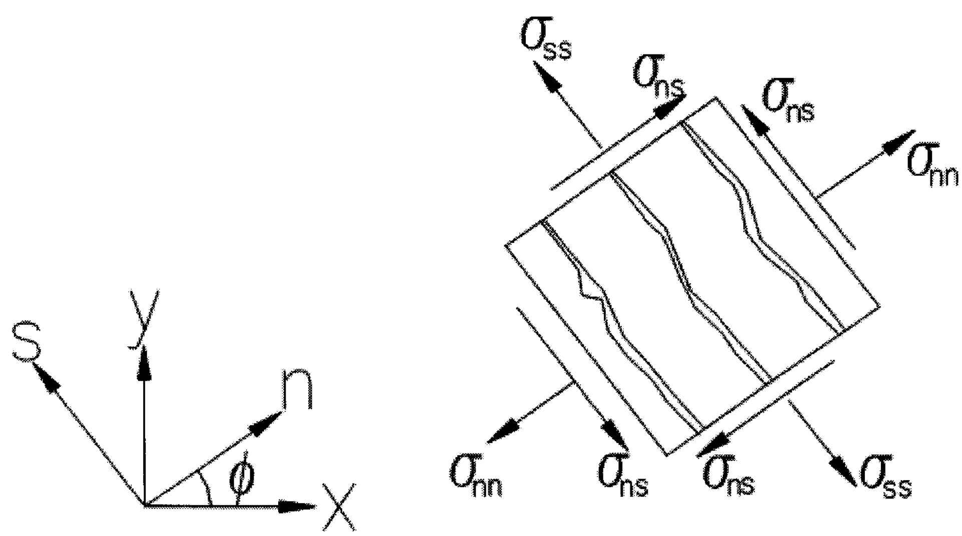

Figure 2.2: Stresses in *x,y*-axes and *n,s*-axes

If, for a plane-stress situation, $\boldsymbol{\sigma}_{ns} = [\sigma_{nn}, \sigma_{ss}, \sigma_{ns}]^t$ and $\boldsymbol{\varepsilon}_{ns} = [\varepsilon_{nn}, \varepsilon_{ss}, \varepsilon_{ns}]^t$,and the secant stiffness matrix $\mathbf{D}^s_{ns}$ is defined as:

$$\mathbf{D}_{ns}^{s} = \begin{bmatrix} 0 & 0 & 0 \\ 0 & E & 0 \\ 0 & 0 & 0 \end{bmatrix} \tag{2.3}$$

The orthotropic elastic stiffness relation in the *n,s*-coordinate system is given as:

$$\boldsymbol{\sigma}_{ns} = \mathbf{D}_{ns}^{s} \boldsymbol{\varepsilon}_{ns} \tag{2.4}$$

If ϕ is the angle from the *x*-axis to the *n*-axis, we can transform the component of $\boldsymbol{\sigma}_{ns}$ and $\boldsymbol{\varepsilon}_{ns}$ to the global *x,y*-coordinate via the transformation matrix **T**:

$$\boldsymbol{\sigma}_{xy}=\mathbf{T}^{t}(\phi)\boldsymbol{\sigma}_{ns} \tag{2.5}$$

$$\boldsymbol{\varepsilon}_{ns}=\mathbf{T}(\phi)\boldsymbol{\varepsilon}_{xy} \tag{2.6}$$

where the transformation matrix **T** is given by:

$$\mathbf{T}=\begin{bmatrix} \cos^2\phi & \sin^2\phi & -\sin\phi\cos\phi \\ \sin^2\phi & \cos^2\phi & \sin\phi\cos\phi \\ 2\sin\phi\cos\phi & -2\sin\phi\cos\phi & \cos^2\phi-\sin^2\phi \end{bmatrix}$$

The local secant stiffness relation given by Eq. (2.4) then transforms into a secant stiffness relation in the global *x,y*-coordinate:

$$\boldsymbol{\sigma}_{xy}=\mathbf{T}^{t}(\phi)\mathbf{D}_{ns}^{s}\mathbf{T}(\phi)\boldsymbol{\varepsilon}_{xy} \tag{2.7}$$

The special case in which ϕ is fixed upon crack initiation, (i.e. when the tension cut-off criterion is first reached) is known as the *fixed smeared-crack model*. When we refer to this angle as ϕ_0, we have instead of Eq. (2.7):

$$\boldsymbol{\sigma}_{xy}=\mathbf{T}^{t}(\phi_0)\mathbf{D}_{ns}^{s}\mathbf{T}(\phi_0)\boldsymbol{\varepsilon}_{xy} \tag{2.7a}$$

The tangential stiffness relation can be obtained by differentiating Eq. (2.7) as follows:

$$\dot{\boldsymbol{\sigma}}_{xy}=\mathbf{T}^{t}(\phi_0)\mathbf{D}_{ns}T(\phi_0)\dot{\boldsymbol{\varepsilon}}_{xy} \tag{2.8}$$

where $\mathbf{D}_{ns}$ is now the material tangent stiffness matrix. For the linear-elastic behavior of concrete, $\mathbf{D}_{ns}^{s} = \mathbf{D}_{ns}$.

Because of ill-conditioning, the use of Eq. (2.3) may result in premature convergence difficulties. Also, a physically unrealistic and distorted crack can be obtained (e.g. Suidan and Schnobrich, 1973). For this reason a reduced shear modulus βG ($0 \leq \beta \leq 1$) was reinserted in the model:

$$\mathbf{D}_{ns}^{s} = \begin{bmatrix} 0 & 0 & 0 \\ 0 & E & 0 \\ 0 & 0 & \beta G \end{bmatrix} \tag{2.9}$$

The use of the so-called shear retention factor β not only reduces the numerical difficulties, but also improves the physical reality of fixed crack models, because it can be thought as a model representation of aggregate interlock (i.e. shear stresses are transferred across the interfaces of cracks). Most researchers simply adopt a constant shear retention factor (β=0.2 is a commonly adopted value), but sometimes a crack-strain dependent factor is employed (Kolmar and Mehlhorn, 1984). The latter option is more realistic since the capability of a crack to transfer shear stresses in Model-II decreases with increasing crack strain.

In Eq. (2.9), the stiffness normal to the crack set to zero demonstrates that a sudden drop in tensile stresses from the initial tensile strength f_t to zero occurs when cracks appear. Similar to the use of a zero shear retention factor, this may cause numerical problems. Furthermore, experiments have shown that when concrete cracks, the tensile stress across the cracks drops but does not disappear immediately. This is known as *tension-softening* in concrete. In a smeared crack model, one can model this by inserting a normal reduction factor μ in Eq. (2.9):

$$\mathbf{D}_{ns}^{s} = \begin{bmatrix} \mu E & 0 & 0 \\ 0 & E & 0 \\ 0 & 0 & \beta G \end{bmatrix} \tag{2.10}$$

Similar to the shear reduction factor β, the normal reduction factor μ can be a function of a strain normal to the crack: $\mu=\mu(\varepsilon_{nn})$. A final refinement is given by the addition of Poisson coupling after cracking. Then, we arrive at the model-I crack band formation of Bažant and Oh (1983) extended with the model-II shear retention:

$$\mathbf{D}_{ns}^{s} = \begin{bmatrix} \dfrac{\mu E}{1-\nu^2\mu} & \dfrac{\nu\mu E}{1-\nu^2\mu} & 0 \\ \dfrac{\nu\mu E}{1-\nu^2\mu} & \dfrac{E}{1-\nu^2\mu} & 0 \\ 0 & 0 & \beta G \end{bmatrix} \qquad (2.11)$$

Rotating-crack concrete models

As observed in the tests by Vecchio and Collins (1982), they suggest that initial crack directions change as loading progresses, and the material behavior of concrete is dominated by the current rather than original crack directions. The rotating-crack models were first proposed by Cope et al. (1980) and developed to reflect this behavior. The distinct differences with the fixed-crack models are that in the rotating-crack models the directions of the major principal stress and the shear normal to the crack are aligned during the entire cracking process. This can be displayed in Eq. (2.7) where ϕ varies. But the directions of principal stress and principal strain for cracked concrete are assumed to coincide. The cracking direction is taken to be perpendicular to the current direction of the major principal strain at any stage of loading. Except the one used by Vecchio (1989) which is based on a total (secant) formulation, the majority of models are based on a tangent stiffness formulation as follows:

$$\dot{\boldsymbol{\sigma}}_{ns} = \mathbf{D}_{ns}\dot{\boldsymbol{\varepsilon}}_{ns} \qquad (2.12)$$

where:

$$
\mathbf{D}_{ns} = \begin{bmatrix} \mu E & 0 & 0 \\ 0 & E & 0 \\ 0 & 0 & \dfrac{\sigma_{nn} - \sigma_{ss}}{2(\varepsilon_{nn} - \varepsilon_{ss})} \end{bmatrix} \tag{2.13}
$$

Multiple crack concrete models

Crack models as discussed in the preceding are based on total strain concepts. This approach works well in many applications, but it has some drawbacks. For example, it is impossible to properly combine cracking and other nonlinear phenomena (e.g., creep, shrinkage, thermal effect) when a total relation is adopted between stress and strain. To overcome this difficulty de Borst et al. (1985) have proposed a model in which the total strain is additively decomposed into a concrete part $\boldsymbol{\varepsilon}^{co}$ and a crack part $\boldsymbol{\varepsilon}^{cr}$:

$$
\boldsymbol{\varepsilon} = \boldsymbol{\varepsilon}^{co} + \boldsymbol{\varepsilon}^{cr} \tag{2.14}
$$

The concrete strain can then be composed of an elastic contribution, a shrinkage contribution, a creep contribution and so on. Similarly, the crack strain can be decomposed further, so that:

$$
\boldsymbol{\varepsilon}^{cr} = \boldsymbol{\varepsilon}_1^{cr} + \boldsymbol{\varepsilon}_2^{cr} + \ldots \tag{2.15}
$$

where $\boldsymbol{\varepsilon}_1^{cr}$ is the strain owing to a primary crack, $\boldsymbol{\varepsilon}_2^{cr}$ is the strain owing to a secondary crack and so on. From Eq. (2.14) and Eq. (2.15), an incremental formulation can be written as follows:

$$
\dot{\boldsymbol{\varepsilon}} = \dot{\boldsymbol{\varepsilon}}^{co} + \dot{\boldsymbol{\varepsilon}}^{cr} \tag{2.16}
$$

and

$$
\dot{\boldsymbol{\varepsilon}}^{cr} = \dot{\boldsymbol{\varepsilon}}_1^{cr} + \dot{\boldsymbol{\varepsilon}}_2^{cr} + \ldots \tag{2.17}
$$

The relation between the crack strain rate of a particular crack (either primary or secondary) is conveniently defined in the coordinate system with the crack. If the crack strain rate of crack n is defined as $\dot{\boldsymbol{\varepsilon}}_n^{cr}$ and $\dot{\mathbf{e}}_n^{cr}$ in the global x,y-coordinate and local n,s-coordinate system, respectively, where $\dot{\mathbf{e}}_n^{cr} = \left[\dot{e}_n^{cr},\ \dot{\gamma}_n^{cr}\right]^t$, the relation between $\dot{\boldsymbol{\varepsilon}}_n^{cr}$ and $\dot{\mathbf{e}}_n^{cr}$ is:

$$\dot{\boldsymbol{\varepsilon}}_n^{cr} = \mathbf{Q}_n \dot{\mathbf{e}}_n^{cr} \tag{2.18}$$

with

$$\mathbf{Q}_n = \begin{bmatrix} \cos^2\theta_n & -\sin\theta_n\cos\theta_n \\ \sin^2\theta_n & \sin\theta_n\cos\theta_n \\ 2\sin\theta_n\cos\theta_n & \cos^2\theta_n - \sin^2\theta_n \end{bmatrix} \tag{2.19}$$

where θ_n is the inclination angle of the normal of crack n with the x-axis.

From Eq. (2.18) and Eq. (2.19)

$$\dot{\boldsymbol{\varepsilon}}^{cr} = \mathbf{Q}_1\dot{\mathbf{e}}_1^{cr} + \mathbf{Q}_2\dot{\mathbf{e}}_2^{cr} + \ldots.. \tag{2.20}$$

By introducing $\dot{\mathbf{e}}^{cr} = \left[\dot{e}_1^{cr}, \dot{\gamma}_1^{cr}, \dot{e}_2^{cr}, \gamma_2^{cr}, \ldots.\right]^t$ and $\mathbf{Q} = \left[\mathbf{Q}_1, \mathbf{Q}_2, \ldots.\right]$, Eq. (2.20) becomes:

$$\dot{\boldsymbol{\varepsilon}}^{cr} = \mathbf{Q}\dot{\mathbf{e}}^{cr} \tag{2.21}$$

In a similar way, a vector $\dot{\mathbf{s}}_n$: $\dot{\mathbf{s}}_n = \left[\dot{s}_n, \dot{t}_n\right]^t$ is defined, where $\dot{s}_n, \dot{t}_n$ are the normal and shear stress rates of crack n at the integration point. The vector $\dot{\mathbf{s}}$, which assembles all the stress rates with respect to their own local n,s-coordinate system, is written as:

$$\dot{\mathbf{s}} = \left[\dot{s}_1, \dot{t}_1, \dot{s}_2, \dot{t}_2, \ldots.\right]^t \tag{2.22}$$

The relation between the stress rate in the global coordinate system $\dot{\boldsymbol{\sigma}}$ and the vector $\dot{\mathbf{s}}$ can subsequently be derived to be:

$$\dot{\mathbf{s}} = \mathbf{Q}^t\dot{\boldsymbol{\sigma}} \tag{2.23}$$

For the concrete between the cracks, the stress-strain relationship is as follows:

$$\dot{\boldsymbol{\sigma}} = \mathbf{E}^{co}\dot{\boldsymbol{\varepsilon}}^{co} \tag{2.24}$$

with the matrix $\mathbf{E}^{co}$ containing the instantaneous modulus of concrete. For most analyses it suffices to use the elasticity matrix for $\mathbf{E}^{co}(\mathbf{E}^{co} = \mathbf{E}^{el})$. However, there is no conceptual limitation to carry out analysis with elastic-plastic or visco-elastic concrete properties to model other nonlinear phenomena (e.g., creep, shrinkage, thermal effects). De Borst (1987) utilizes an iterative approach in which the elastic-fracture matrix is substituted for the elastic matrix in the elastic-plastic relations. Then the computed plastic strain increment is treated as a known strain increment that is subtracted from the total strain increment before the crack mode is activated.

The relation between the crack strain rate $\dot{\mathbf{e}}_n^{cr}$ of crack n and the stress rate $\dot{\mathbf{s}}_n$ in the crack is also defined as:

$$\dot{\mathbf{s}}_n = \mathbf{E}_n^{cr}\dot{\mathbf{e}}_n^{cr} \tag{2.25}$$

where $\mathbf{E}_n^{cr}$ is defined as:

$$\mathbf{E}_n^{cr} = \begin{bmatrix} E^I & 0 \\ 0 & E^{II} \end{bmatrix} \tag{2.26}$$

when a crack is initialized during loading, where $\dfrac{1}{E} + \dfrac{1}{E^I} = \dfrac{1}{\mu E}$, $\dfrac{1}{G} + \dfrac{1}{E^{II}} = \dfrac{1}{\beta E}$

or as:

$$\mathbf{E}_n^{cr} = \begin{bmatrix} S & 0 \\ 0 & E^{II} \end{bmatrix} \tag{2.27}$$

when a crack starts unloading, where $S = \dfrac{\mu E}{(1-\mu)}$

It is again convenient to assemble all the matrices $\mathbf{E}_n^{cr}$ in one matrix $\mathbf{E}^{cr}$ as:

$$\mathbf{E}^{cr} = \begin{bmatrix} \mathbf{E}_1^{cr} & 0 & \dots \\ 0 & \mathbf{E}_2^{cr} & \dots \\ \dots & \dots & \dots \end{bmatrix} \tag{2.28}$$

so that the relation between $\dot{\mathbf{s}}$ and $\dot{\mathbf{e}}^{cr}$ reads:

$$\dot{\mathbf{s}} = \mathbf{E}^{cr}\dot{\mathbf{e}}^{cr} \tag{2.29}$$

Using Eqs. (2.16), (2.21), (2.23), (2.24), and (2.29), the tangential compliance relation for cracked concrete can be written as follows:

$$\dot{\boldsymbol{\varepsilon}} = \left[(\mathbf{E}^{co})^{-1} + \mathbf{Q}(\mathbf{E}^{cr})^{-1}\mathbf{Q}^{t}\right]\dot{\boldsymbol{\sigma}} \tag{2.30}$$

The stiffness relation is therefore written as:

$$\dot{\boldsymbol{\sigma}} = \left\{\mathbf{E}^{co} - \mathbf{E}^{co}\mathbf{Q}\left[\mathbf{E}^{cr} + \mathbf{Q}^{t}\mathbf{E}^{co}\mathbf{Q}\right]^{-1}\mathbf{Q}^{t}\mathbf{E}^{co}\right\}\dot{\boldsymbol{\varepsilon}} \tag{2.31}$$

2.3 Analytical models for corrosion-induced damage of rc structures

2.3.1 Bažant's model

Bažant developed a model for the time of corrosion-induced concrete cracking of concrete structures exposed to seawater. The governing parameters are the corrosion rate, concrete cover depth, bar spacing, and mechanical properties of the concrete (Bažant, 1979). The theoretical equation proposed by Bažant for evaluating the time to cracking of the concrete cover is given by:

$$t_{cr} = \rho_{corr}\frac{d\Delta d}{s\,j_r} \tag{2.32}$$

where t_{cr} is the time to concrete cracking, ρ_{corr} is a function of the densities of steel and rust, d is the reinforcing bar diameter, Δd is the increase in rebar diameter due to corrosion products accumulation, s is the spacing between rebars, and j_r is the rate of rust production, assumed to be constant over time. The increase in rebar diameter Δd was estimated by applying a uniform pressure around the reinforcing bar and assuming concrete to be a homogeneous elastic material.

2.3.2 Cady, Weyers et al.'s models

Based on field observations, Weyers et al. (1993) have indicated that the cracking period has a strong dependence on the corrosion rate, but it is not strongly affected by the cover depth, reinforcing steel spacing and size, and concrete strength. The corrosion rate is largely controlled by the rate of oxygen diffusion to the cathodic areas, resistivity of the pore solution, and concrete temperature. The reason for the discrepancy with Bažant's model may be due to the fact that the corrosion rate of concrete structures that are submerged is limited by the supply of oxygen. Hence, other factors play a greater role in estimating the time to cracking due to corrosion products accumulation around the reinforcing bars.

From a study on the influence of corrosion rates on time to first cracking, Newhouse and Weyers (1996) concluded that the expression given by Eq. (2.32) significantly underestimated the time to concrete cracking when using uniform corrosion rates based on measured metal loss. Reasons given for the difference between calculated and measured values were based on the observations that not all the corrosion products exert an internal pressure around the reinforcing bar perimeter (corrosion products were found as far as 50 mm away from the reinforcement), nor do they result in the same volume increase.

To overcome the limitations of existing models in predicting the time to cracking for concrete bridge decks, Weyers (1998) and Liu and Weyers (1998) developed a cracking model wherein the rate of rust production is not a linear relationship of the product of the corrosion rate and time as stated by Faraday's law. The authors argued that this nonlinearity is due to the fact that iron ions have to diffuse through the rust layer built around the reinforcing bars before any further oxidation can take place. The critical amount of corrosion products needed to induce cracking of the concrete cover was estimated from:

$$W_{crit} = \rho_{rust}\left(\pi\left[\frac{cf_t'}{E_{ef}}\left(\frac{a^2+b^2}{b^2-a^2}+\nu_c\right)+d_o\right]D+\frac{W_{st}}{\rho_{st}}\right) \qquad (2.33)$$

where W_{crit} is the amount of corrosion products needed to induce concrete cracking, ρ_{rust} is the density of corrosion products, c is the concrete cover, f'_t is the concrete tensile strength, E_{ef} is an effective elastic modulus of the concrete (where creep effect are taken into account), ν_c is Poisson's ratio of the concrete, d_o is the thickness of pore band around the steel/concrete interface, D is the rebar diameter, W_{st} is the mass of corroded steel, and ρ_{st} is the density of steel. Equation (2.33) is also built on the assumption that the concrete cover behaves as an elastic thick-wall cylinder under the action of internal pressure arising from corrosion build-up, where a is the inner radius ($a = (D + 2d_o)/2$) and b is the outer radius ($b = a + c$). The time to cover cracking t_{cr} was then calculated from:

$$t_{cr} = \frac{W_{crit}^2}{2k_p} \tag{2.34}$$

where k_p is the rate of rust production, which the authors relate to the rate of metal loss. The resulting model is a nonlinear relation between corrosion build-up and time to cracking, leading to predictions that are more realistic compared to field data (Liu and Weyers, 1998). In this model, cracking is only restricted to the stresses resulting from the expansion of corrosion products; other loading effects in bridge decks such as dynamic loading and freezing and thawing are not considered, although they may accelerate the appearance of cracks.

2.3.3 Noghabai's model

Based on the cracking model proposed by Tepfers (1979), wherein the concrete cover is treated as a thick-wall cylinder subjected to internal pressure, Noghabai (1996) proposed an equation for concrete cracking based on non-linear fracture mechanics. The model adopted the assumptions of Molina et al. (1993) regarding the correlation of circumferential deformations in the concrete due to corrosion product accumulation to the corrosion rate. Noghabai (1996) assumed that prior to the appearance of splitting cracks, both the corrosion build-up and the bursting action of the rebars due to bond may be superimposed.

2.4 Numerical models for corrosion-induced damage of rc structures

2.4.1 Dagher and Kulendran's model

Dagher and Kulendran (1992) developed a two-dimensional finite element model to estimate the damage in concrete resulting from the volume expansion of corrosion products. Their corrosion-damage model was based on the smeared crack approach with a number of options for modelling crack formation and propagation (local-versus-nonlocal continuum approach and strength-versus-fracture mechanics criteria). The model assumed as input parameters the onset and rate of corrosion as well as the geometry of corrosion build-up. Volume expansion due to corrosion products build-up was modelled by imposing predefined displacement fields on the nodes around the perimeter of the reinforcing bars. For each increment of bar expansion, the model evaluated stresses and strains in the surrounding concrete as well as crack locations and directions.

Crack formation and propagation was checked using a fixed-crack smeared approach (Bažant, 1988). Plain-strain isotropic elements were used for the undamaged concrete, whereas orthotropic elements were used for the fully cracked concrete. In the fixed-crack smeared method, a tension-softening curve is needed to model the discontinuous macrocrack behaviour of concrete. The authors used the following tension softening diagrams:

i. A bilinear stress-strain curve with an ascending branch for uncracked concrete and a descending branch for cracked concrete (see Figure 2.3.); and,

ii. A linear stress-strain curve that didn't have a descending branch. In this diagram, the actual tensile strength f_t' was replaced with an equivalent tensile strength f_{teq}', which depended on the element size to avoid mesh-dependency of the results (see Figure 2.4.)

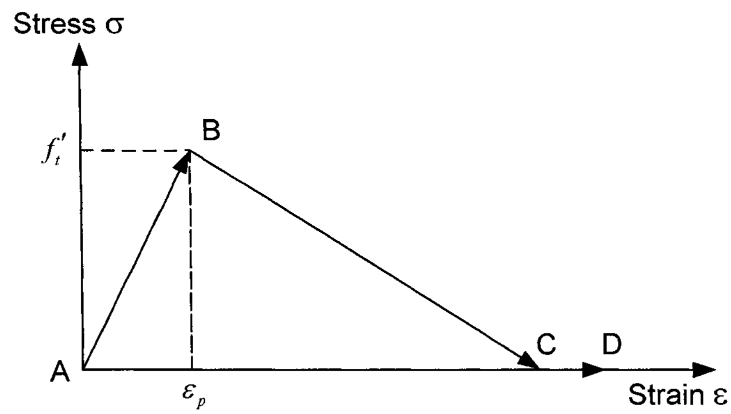

Figure 2.3: Bilinear stress-strain curve

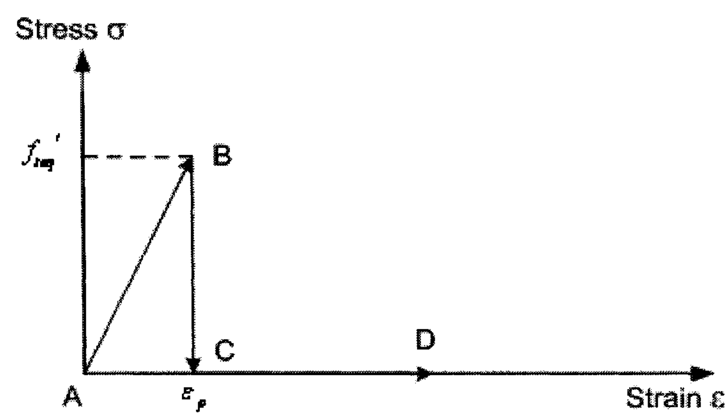

Figure 2.4: Linear stress-strain curve without tension softening

In order to eliminate the spurious dependence of the analysis results on the element size in smeared crack models, the authors used a fracture mechanics criterion for crack propagation. Assuming a sudden vertical drop in the stress-strain curve (line ABCD in Figure 2.4), the fracture energy per unit extension is:

$$G_f = (f_t'^2 / 2E) w_c \tag{2.35}$$

where G_f is the fracture energy for a unit extension of crack, f_t' is the tensile strength of the concrete, E is the tension modulus of intact concrete, and w_c is the width of the crack process zone, which is a material property related to the maximum size of the aggregate in concrete. If the chosen element size h is different from w_c, then the correct fracture energy may be preserved by using an equivalent tensile strength f_{teq}' such that:

$$G_f = (f_{teq}'^2 / 2E)h \tag{2.36}$$

By comparing Eqs. (2.35) and (2.36), the following relationship between f_{teq}' and f_t' is obtained:

$$f_{teq}' = \sqrt{w_c / h}\, f_t' \tag{2.37}$$

In their model, when an equivalent tensile strength f_{teq}' was used for crack propagation, the actual tensile strength f_t' was still used to determine crack initiation.

The authors applied the model to study the damage in concrete bridge decks subjected to uniform corrosion. Since only corrosion-induced damage was modelled and of interest to the authors, only the concrete cover of the bridge deck was discretized in their analyses (see Figure 2.5.) The analyses showed that 0.008 mm of uniform radial bar expansion can cause a plane of delamination in a deck with No. 20 reinforcing bars spaced 152 mm apart. It was also observed that as the bar spacing increased (from 152 mm to 254 mm), the likelihood of delamination decreased and that of the formation of potholes increased. These results were based on corrosion-induced stresses alone, without considering the effect of other types of loading.

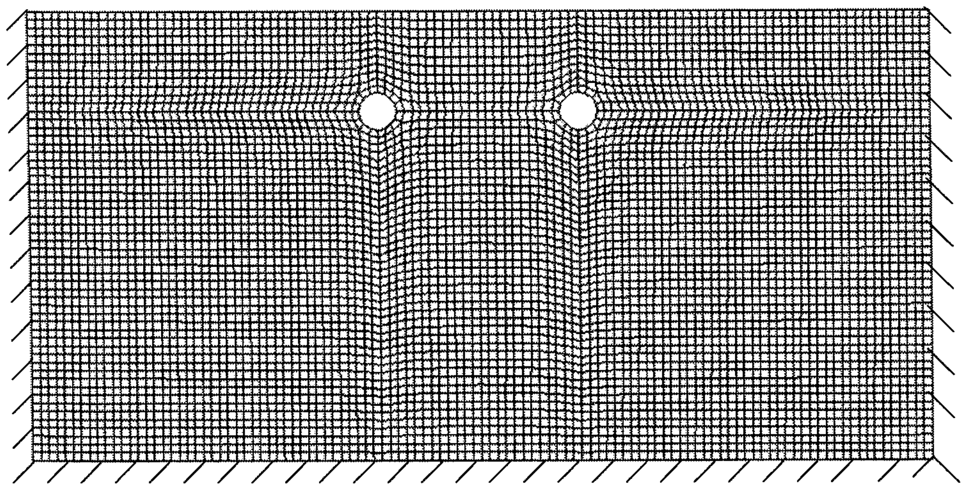

Figure 2.5: Finite element mesh for simulating corrosion damage of rc bridge decks

2.4.2 Molina et al.'s model

Molina et al. (1993) also developed a numerical model based on the finite element method to simulate cracking in concrete due to corrosion of the reinforcement. However, in this model both concrete and steel elements were included in the formulation. Corroding reinforcing steel was modelled by superposition of a decrease in its stiffness, which varied linearly from iron to rust, and an increase in its specific volume, which was achieved by imposing an initial strain on the element being corroded. In fact, this initial strain was imposed as an equivalent thermal load on the structure. The ratio between the specific volumes of rust and iron was taken as 2. Concrete cracking was modelled by a smeared-fixed-crack approach with linear softening. The process of active corrosion was simulated by applying three cumulative load combinations, each representing an advance of 20 μm in the attack penetration, which was assumed to be uniform around the rebar perimeter. The authors concluded that the value given to the specific volume of rust was a determinant factor on crack growth.

2.4.3 Yokozeki et al.'s model

Following a similar approach, Yokozeki et al. (1997) formulated a non-linear elasto-plastic finite element model for predicting first cracking of concrete after the onset of corrosion, and they integrated it in a complete service life prediction model. The authors considered the accelerated damage period following the onset of cracking, as illustrated in Figure 2.6, to be much faster than the time for corrosion initiation and time for first cracking of the concrete cover, and they neglected it in service life estimations. In their corrosion-damage model, the mechanical properties of concrete, steel and corrosion products were defined as input parameters. Concrete was modelled by means of a fracture mechanics approach with a smeared-crack analysis. The stiffness of the steel elements was reduced according to the rust concentration around the rebars. Analyses were performed assuming a state of plane-strain, in which the corrosive expansion force was simulated by assigning strains to the reinforcing bar elements according to:

$$\frac{d\varepsilon}{d\Phi} = \sqrt[3]{\alpha} \tag{2.38}$$

where ε denotes the applied strain, Φ is the rust concentration, and α is the volumetric expansion ratio, which was given a value of 3.20.

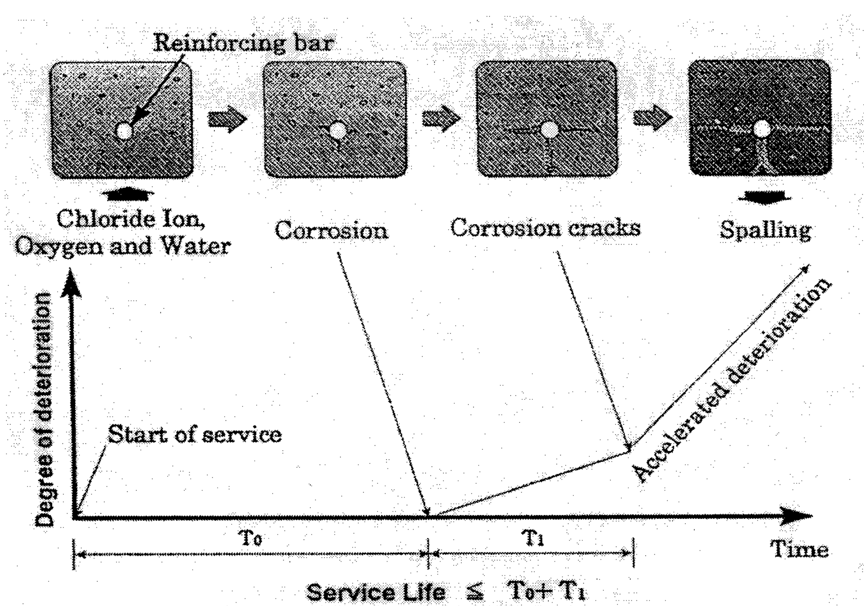

Figure 2.6: Progress of corrosion induced damage (fromYokozeki et al., 1997)

2.4.4 Hansen and Saouma's model

Hansen and Saouma (1999) simulated the process of steel corrosion and concrete cracking through the use of the commercial finite element code ABAQUS (Hibbit, Karlsson and Sorensen, 1995). The authors used the mass transfer capabilities of ABAQUS to simulate electrochemical corrosion in their model. Once the current density due to electrochemical corrosion is determined, the corrosion rate is calculated using Faraday's Law, i.e.,

$$r = \frac{ia}{nF} \tag{2.39}$$

where i is the current density at the electrode/electrolyte interface, a is atomic weight of Fe, n is the number of ions exchanged, and F is Faraday's constant. This corrosion rate is the amount of rust produced at the anodic region of the reinforcing bar, which produces a volume expansion between the reinforcing bar and the surrounding concrete.

The authors then performed a non-linear finite element fracture analyses using a mixed model discrete crack propagation model based on Hillerborg's model to investigate concrete cracking due to corrosion product build-up. The non-linear fracture analysis was performed using the finite element program MERLIN (Reich, Cervenka, and Saouma, 1997). The main finite elements used in these fracture analyses were three-node plain strain elements with linear elastic material properties. Cracks were modeled with four-node interface elements. Two finite element meshes were considered: (1) the first mesh contained 2314 nodes and had a single vertical crack path from the reinforcing bar to the cover surface; and, (2) the second mesh contained 4631 nodes and had five crack paths along the vertical, horizontal, and two diagonal directions.

Their results indicated that cracks propagate from the reinforcing bar in the horizontal, vertical, and diagonal directions, and their extent depend on parameters such as the concrete cover and the rebar spacing. The numerical results highlighted that cracks propagating in the horizontal and vertical directions resulted from crack opening (tensile effect), whereas cracks propagating in the diagonal direction resulted from crack sliding (shear effect).

2.5 Modelling repaired rc bridge decks

2.5.1 Modelling overlays and patches

Chidiac et al. (1997) presented a two-dimensional plane-strain stress analysis model to predict the performance of overlays and patches. A layered approach was implemented in the formulation to accommodate changes in material properties and variations in the strain field distribution (as shown in Figure 2.7). A perfect bond between the old and new concrete was assumed.

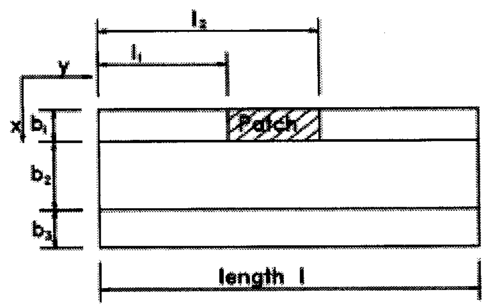

Figure 2.7: Idealized model for a repaired concrete slab

The displacement field for a finite layered system was approximated using a Fourier series along the longitudinal direction and a linear distribution across the thickness, as follows:

$$u = \sum_{m=1}^{r} (c_0 + c_1 x) \sin \frac{m\pi y}{l} \tag{2.40}$$

$$v = \sum_{m=1}^{r} (d_0 + d_1 x) \cos \frac{m\pi y}{l} \tag{2.41}$$

where u is the vertical displacement along the x-axis, v is the horizontal displacement along the y-axis, and r represents the number of terms for the Fourier series. Constants c_0, c_1, d_0, d_1 were introduced to ensure the compatibility of the displacement fields along the contact line of the layers. The analytical solution which forms the basis of this model was derived from the principle of minimum potential energy, as follows:

$$\delta(\Pi) = \delta(U - W) = 0 \tag{2.42}$$

where U and W are the strain energy and potential energy, respectively, and Π is the total potential energy of the system. This model was successfully applied to evaluate the stresses and deformations for a repaired concrete slab subjected to mechanical and thermal loads, wherein the repair system used was both a patch and an overlay. The results of the analyses indicated that compatibility problems arose if thermal and mechanical properties of the repair material and the concrete substrate were dissimilar. The difference in stiffness in the two materials yielded different failure modes depending on the repair system used. For the patch system, it was observed that cracks initiated at the base and corners of the patch. For an overlaid slab, the dominant failure mode observed from the results was edge curling.

2.5.2 Modelling FRP laminates

Tedesco et al. (1999) built a three-dimensional finite element model to simulate the behaviour of an rc bridge repaired with FRP laminates. The deck and girders were modeled independently of each other in order to simulate the effect of the existing cracks in the girders. An isometric view of the finite element model used is shown in Figure 2.8. In the actual bridge, the concrete girders exhibited extensive flexural and shear cracking. These cracks extended through the entire stem of each girder, virtually along their entire length. Therefore the elastic modulus of the girders was reduced to simulate their extensive damage state. The modulus of elasticity of the deck was calculated using the American Concrete Institute standard $E_c = 4730\sqrt{f_c'}$, where f_c' is the concrete compressive strength in MPa.

The finite element analyses were conducted using the ADINA finite element computer programs. The finite element model consisted of 1440 eight-node solid elements for the concrete deck slab, 1280 eight-node solid elements (having a reduced modulus of elasticity to simulate the effect of cracks) for the concrete girders, and 160 truss elements to model the steel reinforcing bars. The bonded FRP laminates were represented with 160 truss elements to model the CFRP plates located at the mid-bottom nodes of the girders. In addition, another 720 truss elements were employed on the sides of the girders to represent the GFRP plates. Perfect bond behaviour was assumed. A typical cross section of the finite element model of the bridge is presented in Figure 2.9.

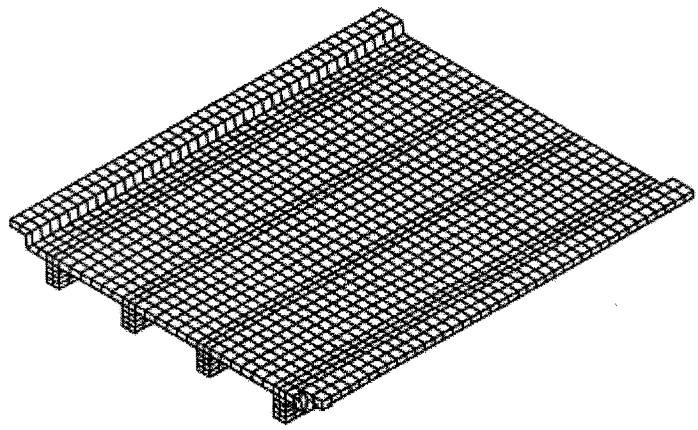

Figure 2.8: An isometric view of the finite element model of the bridge

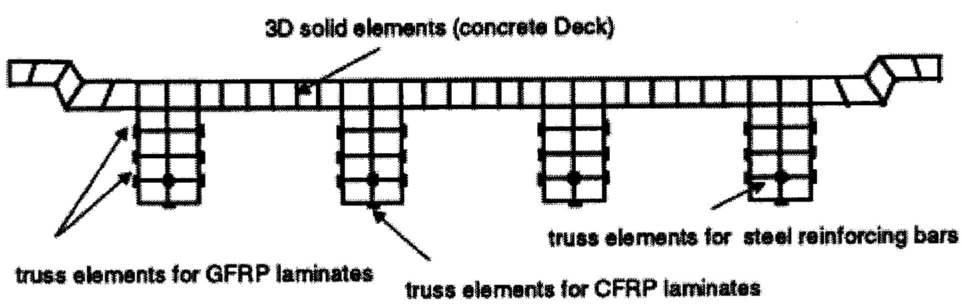

Figure 2.9: Typical cross section of the FEM model for a repaired bridge structure

A comprehensive series of analyses were conducted on the bridge structure. Both static and dynamic analyses were performed to verify the accuracy of the finite element model by replicating field load tests. The dynamic analysis studies included frequency analyses to establish the dynamic characteristics of the bridge, and transient analyses to simulate the dynamic field load tests. A parametric study was also conducted to quantify the effects of varying several cross section characteristics and mechanical properties of the FRP laminates upon the bridge girder structural responses.

The results of the finite element analysis correlated very well with the field test data, and indicated that the external bonding of FRP laminates to the bridge girders reduced the average maximum mid-span girder deflections and reinforcing steel stresses by 9% and 11%, respectively. The results of the parametric study suggest that increasing the FRP plate cross-sectional area can reduce the maximum girder deflections and reinforcing steel stresses by approximately 20% and 22%, respectively. Moreover, increasing the FRP plate modulus of elasticity can reduce both the maximum girder deflections and reinforcing steel stresses by 16%. The loads in this study were in-service loads far below the ultimate capacity of the bridge, so it was sufficiently accurate to use a reduced modulus of elasticity to simulate the effect of cracks in the overall structural response.

Chapter 3

Analytical models

3.1 Introduction

Assuming that concrete is an homogeneous elastic material, the analysis of the state of stress in concrete due to the expansion of corrosion products is done by assuming the concrete deck cover acting as a thick-wall cylinder subjected to a uniform internal pressure (Bažant 1979; Tepfers 1979). It is further assumed that the concrete cylinder is of sufficiently great length compared to its radius, so that the strain in the axial direction is zero (i.e., $\varepsilon_z = 0$). This assumption simulates a state of plane-strain and corresponds to stress conditions associated with a splitting mode of failure.

Under the assumption of plane strain, the stresses in a concrete thick-wall cylinder of inner radius $d/2$ and outer radius $c+d/2$ subjected to a uniform internal pressure p_i are given by (Timoshenko 1956):

$$\sigma_r = \frac{(d/2)^2 p_i}{(c+d/2)^2 - (d/2)^2}\left(1 - \frac{(c+d/2)^2}{r^2}\right) \tag{3.1}$$

$$\sigma_t = \frac{(d/2)^2 p_i}{(c+d/2)^2 - (d/2)^2}\left(1 + \frac{(c+d/2)^2}{r^2}\right) \tag{3.2}$$

where σ_r is the radial stress in concrete, always compressive, σ_t is the tangential stress in concrete, always tensile, d is the rebar diameter, c is the concrete cover, and r is the radius of the concrete ring where stresses are being calculated (see Figure 3.1). The radial displacement u due to the internal pressure p_i is obtained from:

$$u(r) = \frac{(1+\nu)(d/2)^2 p_i}{E_c\left[(c+d/2)^2 - (d/2)^2\right]}\left[(1-2\nu)r + \frac{(c+d/2)^2}{r}\right] \tag{3.3}$$

where ν is Poisson's ratio of concrete, which ranges from 0.15 to 0.20 (Neville 1981), and E_c is the elastic modulus of concrete.

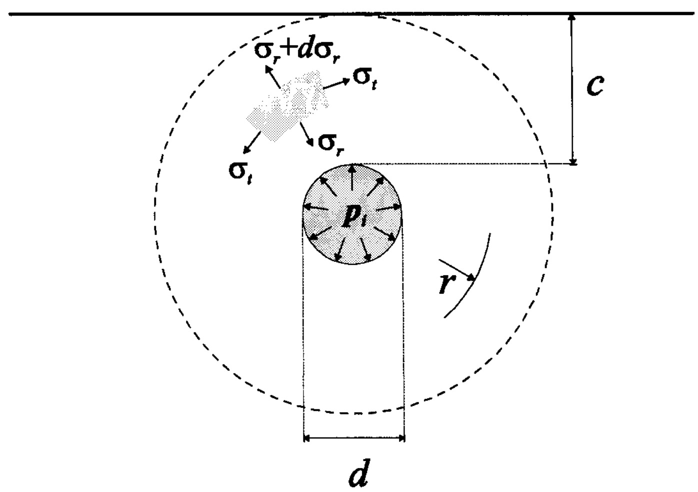

Figure 3.1: Concrete deck cover treated as thick-wall cylinder

The increase in diameter Δd due to accumulation of rust around the rebar is solved for by calculating the radial displacement at the inner surface of the cylinder, i.e., by substituting $r = d/2$ into Eq. 3.3:

$$\frac{\Delta d}{2} = \frac{(1+\nu)(d/2)^2 p_i}{E_c\left[(c+d/2)^2 - (d/2)^2\right]}\left[(1-2\nu)\frac{d}{2} + \frac{(c+d/2)^2}{d/2}\right] \tag{3.4}$$

Equation 3.4 can be further simplified to:

$$\Delta d = \frac{1}{2}\frac{(1+\nu)}{E_c}\frac{p_i}{(c/d)^2 + (c/d)}\left[d(1-\nu) + 2c(c/d+1)\right] \tag{3.5}$$

3.2 Rust accumulation

The transformation of metallic iron into corrosion products is accompanied by an increase in volume due to the lower density of iron oxides compared to that of iron metal itself. Depending on the oxidation state, iron can expand as much as six times its original volume (Rosenberg et al. 1989). Here, it is assumed that the final corrosion product formed is hydrated red rust $Fe(OH)_3$ (Bažant 1979), whose volume is four times larger than that of steel.

In order to calculate this increase in volume, the amount of hydrated red rust produced at the anode first needs to be determined. The mass of hydrated red rust formed per unit length of rebar, m_r, is calculated from (Bažant 1979):

$$m_r = s \cdot j_r \cdot t_p \tag{3.6}$$

where s is the rebar spacing, j_r is the rate of rust production per unit area, and t_p is the time elapsed since corrosion initiation. Equation 3.6 assumes that the rate of production of hydrated red rust j_r is constant after corrosion initiation. The mass of steel consumed to produce m_r is calculated from the ratio of molecular weights of metal iron and hydrated red rust (Bažant 1979), i.e.,

$$m_s = 0.523 m_r \tag{3.7}$$

where m_s is the mass of steel consumed in the corrosion process, also given per unit length of rebar.

The increase in volume ΔV around the reinforcing bar due to accumulation of corrosion products (see Figure 3.2) is calculated from:

$$\Delta V = \frac{\pi}{4}\left[(d + \Delta d)^2 - d^2\right] = \frac{m_r}{\rho_r} - \frac{m_s}{\rho_s} \tag{3.8}$$

where ΔV is the increase in volume per unit length of rebar due to formation of hydrated red rust, d is the rebar diameter, Δd is the increase in rebar diameter due to corrosion build-up, ρ_s is the density of steel (7.85×10^3 kg/m^3), and ρ_r is the density of hydrated red rust, which is one-fourth of ρ_s (1.96×10^3 kg/m^3).

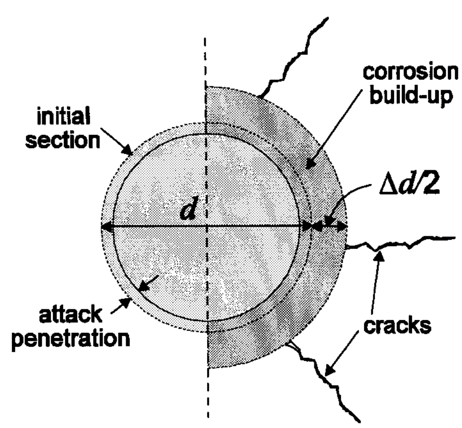

Figure 3.2: Increase in volume due to accumulation of corrosion products

By substituting Eqs. 3.6 and 3.7 into Eq. 3.8, the following relation results:

$$(d + \Delta d)^2 - d^2 = s \cdot j_r \cdot t_p \cdot \frac{4}{\pi}\left[\frac{1}{\rho_r} - \frac{0.523}{\rho_s}\right] \tag{3.9}$$

Noting that $\Delta d << d$, the time elapsed since corrosion initiation, t_p, is calculated from:

$$t_p = \frac{\pi}{2}\left[\frac{1}{\rho_r} - \frac{0.523}{\rho_s}\right]^{-1} \cdot \frac{d\Delta d}{s j_r} \tag{3.10}$$

In deriving Eq. 3.10, it is assumed that all rust products formed create a pressure around the reinforcing bar and therefore contribute to the volume increase given by Eq. 3.8. Although the geometry of corrosion build-up is usually irregular and it is very difficult to determine, it is assumed here that precipitated hydrated red rust is equally distributed along the rebar perimeter, as illustrated in Figure 3.2.

3.3 Crack initiation

The internal pressure p_i acting at the steel/concrete interface is balanced by rings of tensile stresses in the concrete cover, as illustrated in Figure 3.1. The tensile strength of the concrete cover will be first reached at the inner surface of the concrete thick-wall cylinder, and at that point a crack is initiated (see Figure 3.3). The tangential stress in concrete σ_t is maximum at the inner surface of the cylinder, i.e., where $r = d/2$. Thus,

$$\sigma_t^{\max} = p_i \frac{(c+d/2)^2 + (d/2)^2}{(c+d/2)^2 - (d/2)^2} \tag{3.11}$$

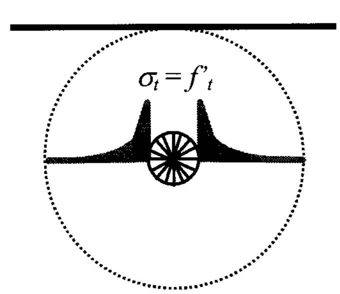

Figure 3.3: Tangential stresses developed in the concrete at crack initiation

When the stress given by Eq. 3.11 exceeds the tensile strength of concrete f'_t, an internal crack starts to form at the steel/concrete interface. The internal pressure required for concrete to initiate a crack at the inner surface of the thick-wall cylinder is therefore obtained by equating $\sigma_t^{\max}$ to f'_t in Eq. 3.11 and solving for p_i, i.e.,

$$p_i = f'_t \frac{(c/d)^2 + (c/d)}{(c/d)^2 + (c/d) + 0.5} \tag{3.12}$$

The increase in rebar diameter Δd_1 due to corrosion build-up at crack initiation is given by substituting Eq. 3.12 into Eq. 3.5, i.e.,

$$\Delta d_1 = \frac{1}{2}\frac{(1+\nu)}{E_c}\frac{f_t'}{(c/d)^2+(c/d)+0.5}\left[d(1-\nu)+2c(c/d+1)\right] \tag{3.13}$$

The time t_1 at which corrosion would produce crack initiation at the steel/concrete interface is given by:

$$t_1 = t_i + t_{p1}$$

where t_i is the time to onset of corrosion and t_{p1} is calculated by substituting Δd_1 from Eq. 3.13 into Eq. 3.10, i.e.,

$$t_{p1} = \frac{\pi}{4}\left[\frac{1}{\rho_r}-\frac{0.523}{\rho_s}\right]^{-1}\cdot\frac{d}{sj_r}\cdot\frac{(1+\nu)}{E_c}\frac{f_t'}{(c/d)^2+(c/d)+0.5}\left[d(1-\nu)+2c(c/d+1)\right] \tag{3.14}$$

3.4 Longitudinal cracking

Although an internal crack starts at the inner surface of the concrete cylinder when the peak tensile stress exceeds the tensile strength of the concrete cover, the ultimate tensile load capacity of the concrete cylinder is not reached yet. As the internal pressure is increased because of further accumulation of hydrated red rust around the reinforcing bar, the outer tensile concrete rings will be stressed further up to the concrete tensile strength. The ultimate tensile load of the cylinder will be reached when the crack propagates through the entire concrete cover.

After a crack has initiated at the steel/concrete interface, it starts to propagate through the concrete cover as the tangential stresses reach f'_t, as illustrated in Figure 3.4. However, concrete still behaves elastically in the outer part where the tangential stresses are still below f'_t. The internal pressure p_i acting at the steel/concrete interface is now transferred through the concrete teeth between cracks to the uncracked part of the cylinder. Since the inner area of this uncracked ring is larger than that of the cylinder without any crack, the pressure at this surface must therefore be reduced accordingly (Tepfers 1979), i.e.,

$$p_e = p_i\frac{d}{2e} \tag{3.15}$$

where p_e is the pressure acting at the inner surface of the uncracked ring, and e is the crack penetration length (see Figure 3.4). The uncracked ring of concrete can now be treated as a thick-wall cylinder in itself, with an inner radius equal to e and subjected to an internal pressure p_e. The tangential stresses in this outer part of the concrete ring can be evaluated similar to Eq. 3.2, i.e.,

$$\sigma_t = p_i \frac{d}{2e} \frac{e^2}{(c+d/2)^2 - e^2}\left(1 + \frac{(c+d/2)^2}{r^2}\right) \tag{3.16}$$

The maximum tangential stress at the inner surface of this uncracked cylinder ($r = e$) is calculated from:

$$\sigma_t^{\max} = p_i \frac{d}{2e} \frac{(c+d/2)^2 + e^2}{(c+d/2)^2 - e^2}, \qquad \text{where } \frac{d}{2} \le e \le c + \frac{d}{2} \tag{3.17}$$

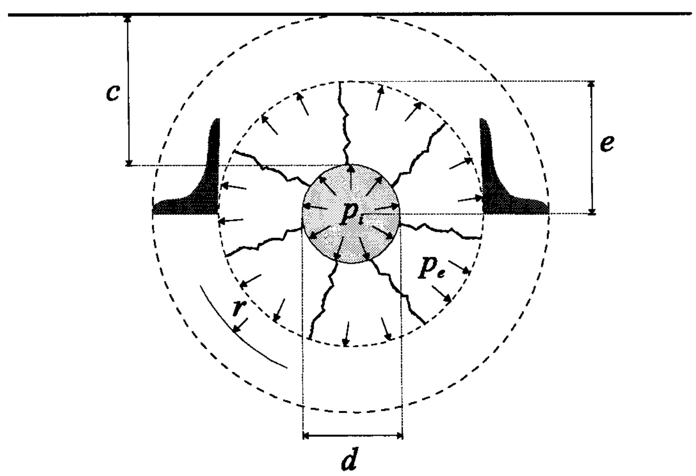

Figure 3.4: Concrete thick-wall cylinder with internal cracks

The maximum stress given in Eq. 3.17 corresponds to the attainment of the concrete tensile strength, i.e., $\sigma_t^{\max} = f_t'$. Equation 3.17 is only valid when the internal pressure p_i resulting from hydrated red rust accumulation around the rebar exhibits a maximum for a value of e within the bounds $d/2$ and $c+d/2$. By differentiating p_i/f_t' in Eq. 3.17 with respect to e and equating the derivative to zero, the value of e for which the tensile load capacity of the concrete thick-wall cylinder is a maximum is obtained as (Tepfers 1979):

$$e = 0.486\left(c + \frac{d}{2}\right) \tag{3.18}$$

As a consequence, internal longitudinal cracks can develop and penetrate the concrete cover to an optimum depth equal to:

$$\text{Crack depth} = e - \frac{d}{2} = 0.486c - 0.257d \tag{3.19}$$

When this depth is exceeded, the crack penetrates right through the concrete cover because the tensile load capacity of the concrete ring is then reached. The tensile stresses developed in the concrete thick-wall cylinder when internal cracks have developed are evaluated from Eq. 3.16 for $e = 0.486(c + d/2)$. The internal pressure p_i required to crack the cover is calculated from Eq. 3.17 with e given by Eq. 3.18 and $\sigma_t^{\max} = f_t'$. The resulting expression is given by (Tepfers 1979):

$$p_i = f_t' \frac{(c/d) + 0.5}{1.665} \tag{3.20}$$

The increase in rebar diameter Δd_2 to cause cracks to appear at the deck surface is given by substituting Eq. 3.20 into Eq. 3.5, i.e.,

$$\Delta d_2 = \frac{1}{3.33} \frac{(1+\nu)}{E_c} f_t' \frac{(c/d) + 0.5}{(c/d)^2 + (c/d)} \left[d(1-\nu) + 2c(c/d + 1) \right] \tag{3.21}$$

The time t_2 at which corrosion would produce surface cracking is given by:

$$t_2 = t_i + t_{p2}$$

where t_i is the time to onset of corrosion and t_{p2} is calculated by substituting Δd_2 from Eq. 3.21 into Eq. 3.10, i.e.,

$$t_{p2} = \frac{\pi}{6.66} \left[\frac{1}{\rho_r} - \frac{0.523}{\rho_s} \right]^{-1} \cdot \frac{d}{s j_r} \cdot \frac{(1+\nu)}{E_c} f_t' \frac{(c/d) + 0.5}{(c/d)^2 + (c/d)} \left[d(1-\nu) + 2c(c/d + 1) \right] \tag{3.22}$$

3.5 Spalling

After the propagation of an internal crack through the entire concrete cover, the pressure p_i generated by corrosion products build-up around the reinforcing bar will be sustained until part of the cover spalls off. By assuming a 45°-plane of failure with respect to the concrete deck surface, as illustrated in Figure 3.5, the concrete cover will not spall off until the tensile strength of section AB has been exceeded (Bažant 1979; Martín-Pérez 1999; Tepfers 1982). By establishing equilibrium in the vertical direction, the internal pressure p_i corresponding to the attainment of tensile strength at AB is given by (Martín-Pérez 1999):

$$p_i = 2f_t'\left(c/d + 0.5\right) \tag{3.23}$$

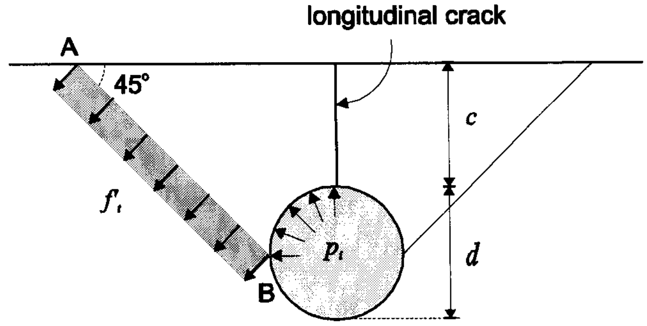

Figure 3.5: Spalling of the concrete cover

The increase in rebar diameter Δd_3 to cause spalling of the concrete cover is given by substituting Eq. 3.23 into Eq. 3.5, i.e.,

$$\Delta d_3 = \frac{(1+\nu)}{E_c} f_t' \frac{(c/d + 0.5)}{(c/d)^2 + (c/d)}\left[d(1-\nu) + 2c(c/d+1)\right] \tag{3.24}$$

The time t_3 at which corrosion would produce spalling of the deck cover is given by:

$$t_3 = t_i + t_{p3}$$

where t_i is the time to onset of corrosion and t_{p3} is calculated by substituting Δd_3 from Eq. 3.24 into Eq. 3.10, i.e.,

$$t_{p3} = \frac{\pi}{2}\left[\frac{1}{\rho_r} - \frac{0.523}{\rho_s}\right]^{-1} \cdot \frac{d}{sj_r} \cdot \frac{(1+\nu)}{E_c} f_t' \frac{(c/d+0.5)}{(c/d)^2 + (c/d)}\left[d(1-\nu) + 2c(c/d+1)\right] \tag{3.25}$$

3.6 Delamination

Delamination of the concrete deck cover occurs when a crack runs parallel to the surface from one rebar to another instead of reaching it (see Figure 3.6). By establishing equilibrium along the vertical direction, the internal pressure p_i corresponding to the attainment of tensile strength at the crack plane is given by (Bažant 1979):

$$p_i = f_t'\left(s/d - 1\right) \tag{3.26}$$

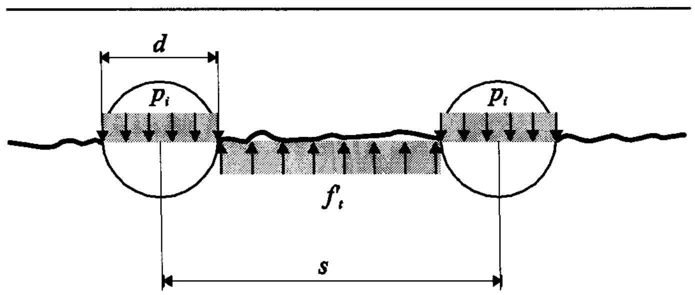

Figure 3.6: Delamination of the concrete cover

The increase in rebar diameter Δd_4 to cause delamination of the concrete cover is given by substituting Eq. 3.26 into Eq. 3.5, i.e.,

$$\Delta d_4 = \frac{1}{2}\frac{(1+\nu)}{E_c} f_t' \frac{(s/d)-1}{(c/d)^2+(c/d)}\left[d(1-\nu)+2c(c/d+1)\right] \tag{3.27}$$

The time t_4 at which corrosion would produce delamination of the deck cover is given by:

$$t_4 = t_i + t_{p4}$$

where t_i is the time to onset of corrosion and t_{p4} is calculated by substituting Δd_4 from Eq. 3.27 into Eq. 3.10, i.e.,

$$t_{p4} = \frac{\pi}{4}\left[\frac{1}{\rho_r} - \frac{0.523}{\rho_s}\right]^{-1} \cdot \frac{d}{s j_r} \cdot \frac{(1+\nu)}{E_c} f_t' \frac{(s/d)-1}{(c/d)^2+(c/d)}\left[d(1-\nu)+2c(c/d+1)\right] \tag{3.28}$$

Depending on the geometry configuration of the reinforcing bars in the concrete deck, different patterns will govern failure as illustrated in Figure 3.7. Spalling of the concrete cover governs over delamination if the pressure given by Eq. 3.23 is lower than that given by Eq. 3.26. To establish the limiting criterion between these two failure patterns, Eqs. 3.23 and 3.26 are equated to relate the governing parameters c and s, i.e.,

$$2 f_t'(c/d+0.5) \le f_t'(s/d-1) \quad \Rightarrow \quad c \le \frac{s}{2} - d \tag{3.29}$$

For concrete deck covers c lower or equal to $(s/2)-d$, the governing failure mechanism as given by Eq. 3.23 will be spalling. For those bridge decks where $c > (s/2)-d$, the governing failure mechanism will be delamination, with Eq. 3.26 giving the required pressure to delaminate the deck cover.

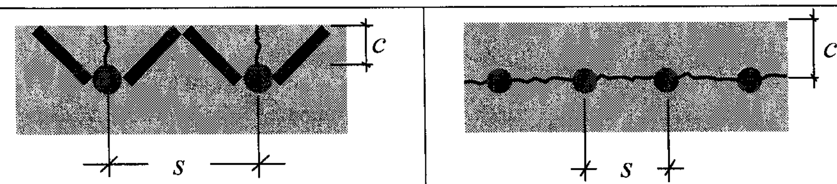

$c \le (s/2) - d$	$c > (s/2) - d$
(a) Spalling	(b) Delamination

Figure 3.7: Corrosion-induced failure patterns of concrete bridge decks

Figure 3.8 shows the plot of internal pressure p_i normalized to f'_t against the ratio of concrete cover c to rebar diameter d for the relations given by Eqs. 3.12, 3.20, 3.23, and 3.26, which respectively correspond to the expressions for the internal pressure required for cracking initiation, longitudinal cracking, spalling, and delamination of the concrete cover. For any value of c/d, as the internal pressure due to the accumulation of rust around the rebar reaches the concrete tensile strength, internal cracks start to originate at the interface between the steel and the concrete (denoted by the blue line labelled "Crack initiation " in Figure 3.8). Depending on the geometric configuration of the concrete cover and top reinforcing mat of the deck, the internal pressure p_i resulting from further accumulation of corrosion products will cause the concrete cover to fail by longitudinal cracking followed by spalling, longitudinal cracking followed by delamination, or delamination alone. For the example illustrated in Figure 3.8, where the ratio of rebar spacing s to rebar diameter d is set to 4, the corrosion-induced damage will manifest itself as longitudinal cracking followed by spalling for $c/d \le 3$, as longitudinal cracking followed by delamination for $3 < c/d \le 4.5$, or just as delamination for $c/d > 4.5$.

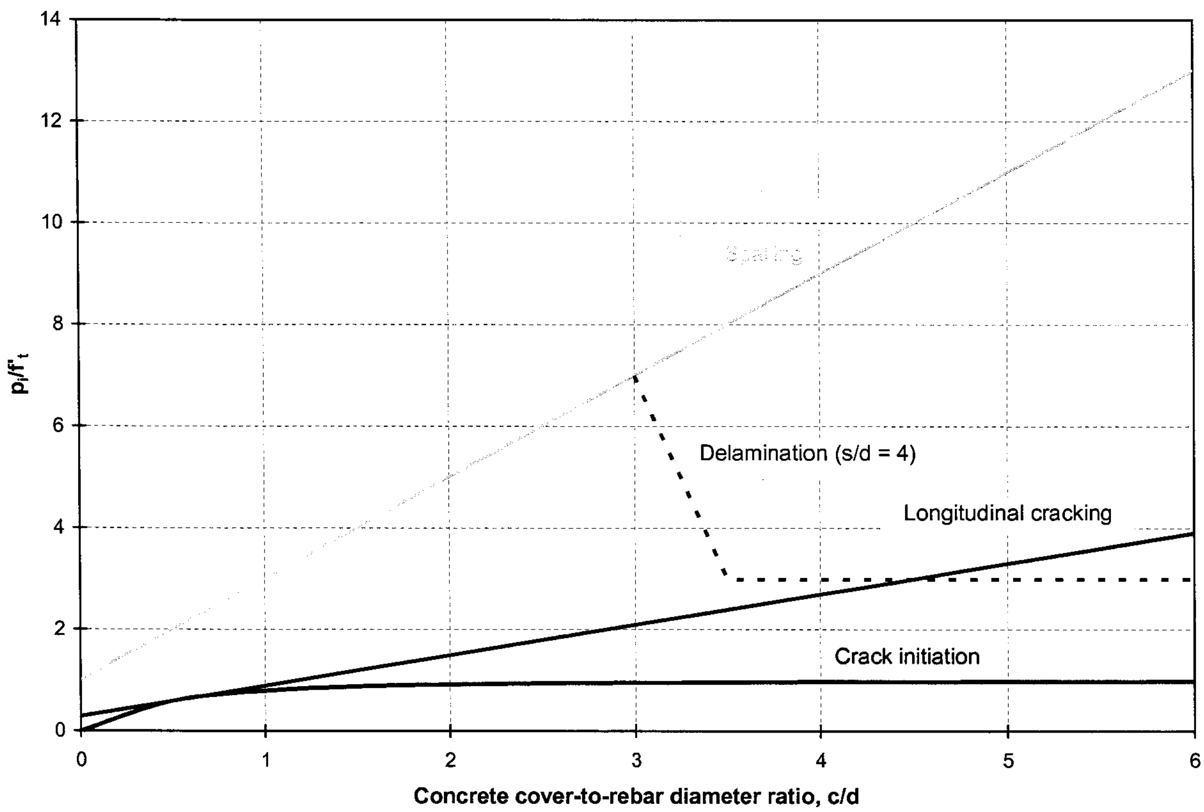

Figure 3.8: Pressure required for crack initiation, longitudinal cracking, spalling and delamination of the concrete deck cover

Chapter 4

Finite element model of corrosion-induced damage of rc bridge decks

4.1 Introduction

Corrosion-induced damage of rc bridge decks was investigated using the finite element method. For this purpose, the commercial finite element package ABAQUS/Standard was used (Hibbit Karlsson & Sorensen Inc. 2004). The analysis focused on corrosion-induced cracking of the concrete, because it is the serviceability limit state triggering repair in damaged reinforced concrete bridge decks. Two constitutive models for plain concrete available in ABAQUS/STANDARD were used in this study to simulate the initiation and propagation of cracks in the reinforced concrete decks under different corrosion build-up levels. The analysis was setup to simulate three main failure modes of corrosion-induced damage of rc bridge decks: longitudinal cracking, delamination and spalling of the concrete. The objective of the finite element analysis was to conduct a parametric investigation of the influence of various design variables on the concrete deck failure modes.

4.2 Assumptions and approach

The damage caused by corroding reinforcing bars was predicted by analyzing the state of stress induced in the surrounding concrete. The following assumptions were made:

1. Even though the real problem is three-dimensional, the concrete deck was modeled in a state of plane strain ($\varepsilon_z = 0$). This assumption corresponds to stress conditions associated with a splitting mode of failure.
2. The geometry of corrosion products was assumed to be a uniform build-up around the surface of the rebar.
3. The quality and strength of the concrete were assumed to be time-independent.

Based on these assumptions, the accumulation of corrosion products on the reinforcing bars was simulated by imposing a uniform radical displacement along the surface of the reinforcing bar ($\Delta d / 2$ in Figure 4.2). This displacement was divided between 100 to 400 equal increments, i.e., time steps in ABAQUS. Then, by inspecting the crack patterns in the finite element models, the values of the corrosion build-up to cause the different failure modes, (i.e. cracking initiation, delamination, longitudinal cracking and spalling) were obtained.

4.3 Modeling concrete behavior

Two constitutive models for plain concrete were used in this study to simulate the nonlinear behavior of the damaged concrete deck. These models are the smeared crack model and damaged plasticity model available in the ABAQUS/STANDARD material library. The theories of these two models are presented in the following:

In smeared crack model, a Mohr-Coulomb type compression yield surface with a crack detection failure surface is used. When the principal stress components of concrete are predominately compressive, the response of the concrete is modeled by an elastic-plastic theory, using a simple form of yield surface in terms of the first and second stresses invariants, p and q that are defined below. Associated flow and an isotropic hardening rule are used.

On the contrary, when these components are dominantly in tension, cracking is assumed to occur by these stresses reaching the crack detection surface. This failure surface is taken to be a simple Coulomb line in terms of the first and second stresses invariants, p and q that are defined below. The orientation of the crack is stored. Damage elasticity is then used to model the existing crack. This model is a smeared crack model, in the sense that it does not intend to track individual macro cracks, rather it assumed the microcracks smeared over elements. So constitutive calculations are preformed independently at each integration point of the finite element model, and the presence of cracks enters into these calculations by the way the cracks affect the stress and material stiffness associated with the integration point. The principle concern is that this modeling approach can introduce mesh sensitive in the solution, e.g. the finite element results do not converge to a unique result with the mesh refinement. To solve this problem, Hilleborg's (1976) approach based on brittle fracture concepts is introduced for practical purposes. This aspect of the model is discussed below in the section on cracking.

In damaged plasticity model, concepts of isotropic damaged elasticity in combination with isotropic tensile and compressive plasticity are used to represent the nonlinear behavior of concrete. It assumes that the main two failure mechanisms are tensile cracking and compressive crushing of the concrete material. The evolution of the yield (or failure) surface is controlled by two hardening variables, $\tilde{\varepsilon}_t^{pl}$ and $\tilde{\varepsilon}_c^{pl}$, linked to failure mechanisms under tension and compression loading, respectively. $\tilde{\varepsilon}_t^{pl}$ and $\tilde{\varepsilon}_c^{pl}$ are defined as tensile and compressive equivalent plastic strains respectively.

In order to use above constitutive models, the material properties of concrete should be input to meet the requirements of ABAQUS/STANDARD. The concrete deck was assumed to be normal strength concrete with a uniaxial compressive strength f_c' of 30MPa.

Under uniaxial compression, the concrete strain ε_0 corresponding to the peak stress f_c' is usually around the range of 0.002–0.003. A representative value suggested by ACI Committee 318 [ACI 318-99 (1999)] and used in the study was $\varepsilon_0 = 0.003$

The Poisson's ratio v_c of concrete under uniaxial compressive stress ranges from about 0.15–0.22, with a representative value of 0.19 or 0.20 (ASCE 1982). In this study, the Poisson's ratio of concrete was assumed to be 0.2.

The uniaxial tensile strength of concrete f_t' is difficult to measure. For this study, this value was taken as (ASCE 1982):

$$f_t' = 0.33\sqrt{f_c'} \text{ (MPa)} \tag{4.1}$$

The modulus of elasticity of concrete E_c was highly correlated to its compressive strength and can be calculated with reasonable accuracy from the empirical equation [ACI 318-99 (1999)]:

$$E_c = 4700\sqrt{f_c'} \text{ (MPa)} \tag{4.2}$$

Under multiaxial loading, the smeared crack model uses uniaxial stress–strain relations in tension and compression to define the failure surface and its hardening behavior of concrete. The basic idea of this approach is to take this failure surface and its hardening to be a simple Coulomb line in terms of the hydrostatic pressure and the Mises equivalent deviatoric stress, p and q , and hardening parameters λ_c, λ_t. These parameters are then related to the uniaxial stress–strain relations in tension and compression by setting the stress condition to a uniaxial tension and compression. The damaged plasticity model uses a similar approach to capture the yield surface and the hardening behavior of concrete. The only difference is that the damaged plasticity model uses yield function and hardening law proposed by Lubliner et al. (1989) and incorporates the modifications proposed by Lee and Fenves (1998) in terms of the effective hydrostatic pressure and the effective Mises equivalent deviatoric stress, $\bar{p}$ and $\bar{q}$,and hardening parameters $\tilde{\varepsilon}_t^{pl}$ and $\tilde{\varepsilon}_c^{pl}$, and uses a nonassociated flow. The details of these models were presented in Section 4.4.

In this study, the unaxial stress–strain relationship of concrete in compression proposed by Saenz (1964), was used, i.e.,

$$\sigma_c = \frac{E_c \varepsilon_c}{1 + (R + R_E - 2)(\frac{\varepsilon_c}{\varepsilon_0}) - (2R - 1)(\frac{\varepsilon_c}{\varepsilon_0})^2 + R(\frac{\varepsilon_c}{\varepsilon_0})^3} \tag{4.3}$$

where

$$R = \frac{R_E(R_\sigma - 1)}{(R_\varepsilon - 1)^2} - \frac{1}{R_\varepsilon}, \quad R_E = \frac{E_c}{E_0}, \quad E_0 = \frac{f_c'}{\varepsilon_0} \quad \text{and} \quad R_\sigma = 4, R_\varepsilon = 4$$

In this study, Equation (4.3) was approximated here by several piecewise linear segments as shown in Figure 4.1.

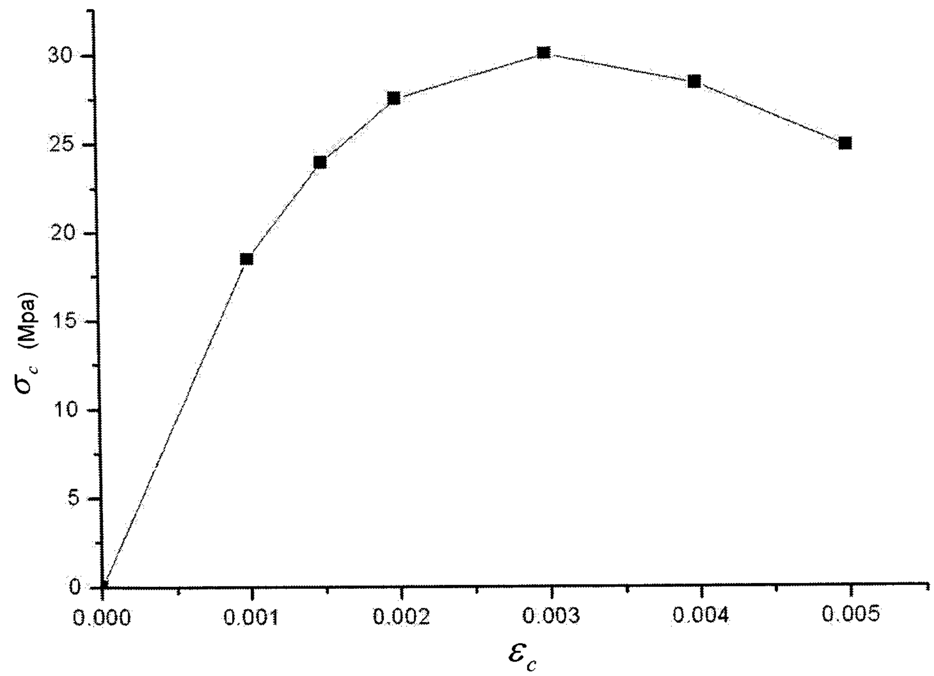

Figure 4.1: Uniaxial stress-strain relation for concrete in compression

In order to overcome mesh-sensitive results when cracking of the concrete takes place, Hilleborg's (1976) fracture energy G_f concept was used in the analysis. The detail of this method was discussed in Section 4.4.

The empirical formula of G_f proposed by CEB-FIP Code (1993) was used in this analysis:

$$G_f = \alpha_f (f_c')^{0.7} \tag{4.4}$$

where α_f is an empirical coefficient that depends on the maximum aggregate size. A value of $\alpha_f = 6$ was used in this analysis for maximum aggregate size around 16mm.

4.4 Finite element model independent to constrains

4.4.1 Introduction

In Chapter 3, the analytical models for corrosion-induced damage of the rc bridge decks were dependent on the diameter of the rebar d , the clear cover of the reinforced concrete bridge deck c, and the spacing between rebars s. To compare the results obtained in Chapter 3, finite element models were constructed to include these three design parameters. Since the area of interest was that of the concrete surrounding a corroding rebar (concrete cover) or between two corroding rebars, only this area was discretized (See Figure 4.2). However, other parameters, such as constrain types, the distance from the center of the rebar to the constrained edge, a, were also needed to complete the numerical analysis. In this study, a finite element model that was independent to parameters defining boundary locations was used.

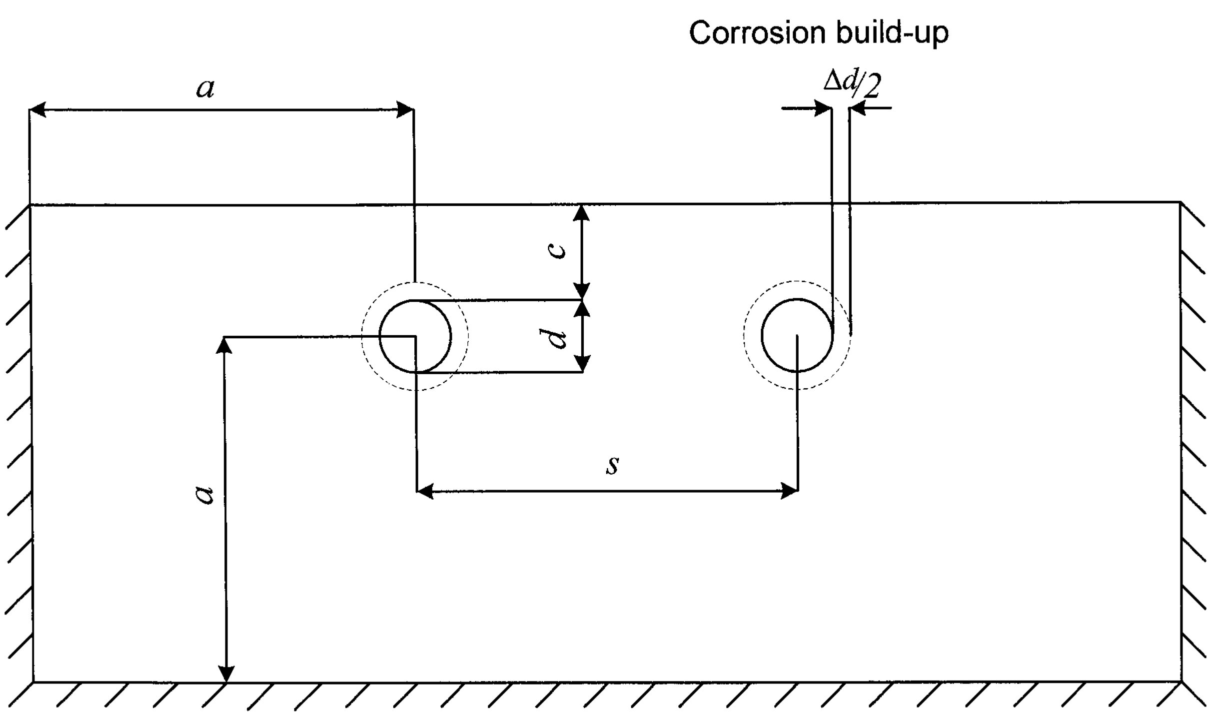

Figure 4.2: Geometry of bridge deck model

According to St. Venant's Principle, the difference between the stresses caused by statically equivalent load systems is insignificant at distances greater than the largest dimension of the area over which the loads are acting. In this study, load was input as the corrosion build-up along the surface of the rebar, so the effect of the corrosion build-up can be seen as a localized effect around the rebar. Therefore, if the boundaries set on the model are sufficiently away from the rebar, they should have little effect on the damage modes caused by the corrosion build-up $\Delta d/2$. In the model presented in this study, the distance from the center of the rebar to the constrained edge, a, was selected as $a \geq 3c$. The analyses showed that first-order elements with reduced-integration were preferred for this type of analysis due to the large strain gradients induced by the large values of the corrosion build-up. Comparisons between the two constitutive models for concrete in the ABAQUS/STANDARD material library mentioned above were also made. The results showed that the damaged plasticity model is more robust from a computational standpoint, since it can carry more displacement increments before it encounters numerical difficulties due to extensive cracking of concrete cover. Finally, the selection of a was verified to make sure that the finite element model built was independent to the location of the boundaries. Section 4.4.2 through Section 4.4.4 present the sensitivity analysis carried out to establish the most appropriate solid element using concrete constitutive model from ABAQUS/STANDARD library, as well as the value for a. The size of the mesh is almost $c/10$.

4.4.2 Selection of the type of the finite element

In ABAQUS/STANDARD, all elements use numerical integration to allow complete generality in material behavior. Hence, the virtual work integral is replaced by a summation as:

$$\int_V \boldsymbol{\sigma} : \delta \mathbf{D} \, dV \approx \sum_{i=1}^{n} \boldsymbol{\sigma}_i : \delta \mathbf{D}_i V_i \tag{4.5}$$

where $\boldsymbol{\sigma}$ is the stress tensor, $\delta\mathbf{D}$ is the virtual rate of deformation tensor, V is the volume of the structure, n is the number of integration points in the element, V_i is the volume associated with each integration point, and $\boldsymbol{\sigma}_i$ and $\delta\mathbf{D}_i$ are the stress tensor and virtual rate of deformation tensor at each integration points respectively. For full integration, the number of integration points used is sufficient to integrate the virtual work expression exactly, at least for linear material behavior. For reduced integration, the number of integration points is sufficient to integrate exactly the contributions of the strain field that are one order less than the order of interpolation, and the higher-order contributions to the strain field present in these elements are not integrated. Practical experience suggests that little accuracy is gained by using higher-order elements than quadratic ones, so ABAQUS does not offer any higher-order ones.

In order to decide which type of element is more appropriate for the application at hand, the two aspects of the element mentioned above were considered, i.e., full or reduced integration and first-order or second-order element. The suggestions provided by ABAQUS (2002) are as following:

1. The advantage of the reduced integration elements is that it has the so-called Barlow point property (Barlow, 1976): the strains are calculated from the interpolation functions with higher accuracy at these points than anywhere else in the element. The second advantage is that the reduced number of integration points decreases CPU time and storage requirements. The disadvantage is that the reduced integration procedure can admit deformation modes that cause no straining at the integration points. These zero-energy modes make the element rank-deficient and introduce a phenomenon called "hourglassing," where the zero energy mode starts propagating through the mesh, leading to inaccurate solutions. To prevent these excessive deformations, an additional artificial stiffness is added to the element. In this so-called hourglass control procedure, a small artificial stiffness is associated with the zero-energy deformation modes. The elements with reduced-integration used in this study had the hourglass control function.
2. The use of second-order elements is preferred in elliptic applications, i.e., the deformation field is a smooth elliptic curve. But many problems of practical interest are not elliptic: localizations arise in one form or another. This allows discontinuities to occur in the solution. So if the finite element solution is to exhibit accuracy, these discontinuities in the gradient field of the solution should be reasonably well modeled. In such case, the first-order elements have proved to be more successful. For first-order elements the uniform strain method yields the exact average strain over the element volume. Not only is this important with respect to the values available for output, it is also significant when the constitutive model is nonlinear, since the strains passed into the constitutive routines are a better representation of the actual strains.

To verify the above suggestions, four types of the plane strain element provided in the ABAQUS/STANDARD elements library were tested in the analyses:

- 4 nodes first-order with full integration (CPE4) (linear)
- 4 nodes first-order with reduced integration (CPE4R) (linear)
- 8 nodes second-order with full integration (CPE8) (quadratic)
- 8 nodes second-order with reduced integration (CPE8R) (quadratic)

The parameters showed in Figure 4.2 were select as:

$$d = 16\text{mm} \; ; \quad c = 35\text{mm} \; ; \quad a = 150\text{mm} \; ; \quad s = 173\text{mm}$$

For total radial corrosion build-up $\Delta d / 2 = 0.2\text{mm}$ and the number of time increment steps was 400, at each step the radial corrosion build-up was $(\Delta d / 2) / 400 = 0.0005\text{mm}$.

The mesh of the model in Figure 4.2 is illustrated in Figure 4.3 and Figure 4.4 for linear and quadratic elements. The size of the mesh is around 3mm, almost *c*/10.

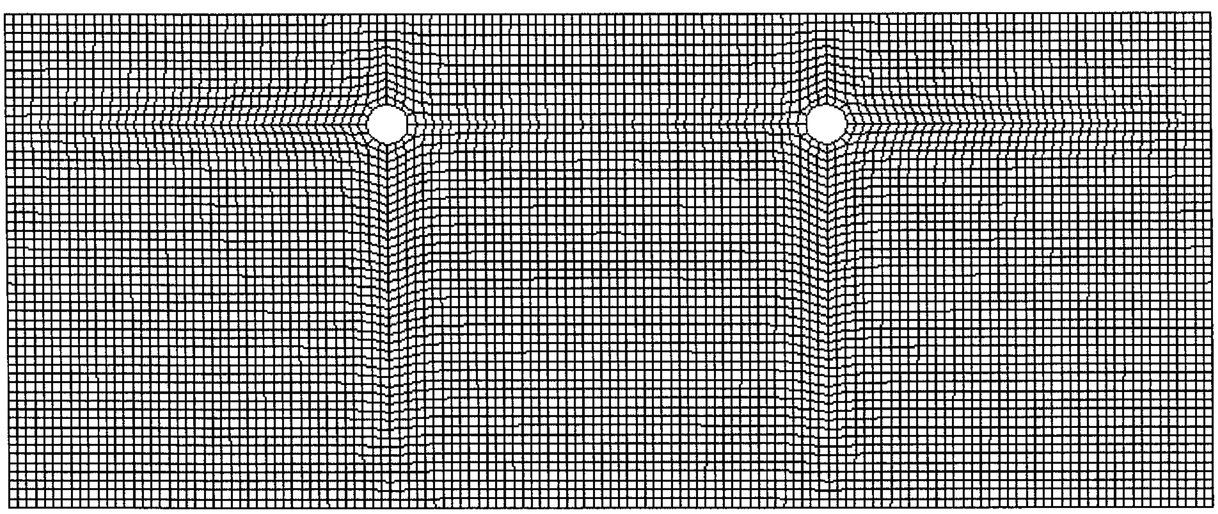

Figure 4.3: Finite element mesh for CPE4 and CPE4R

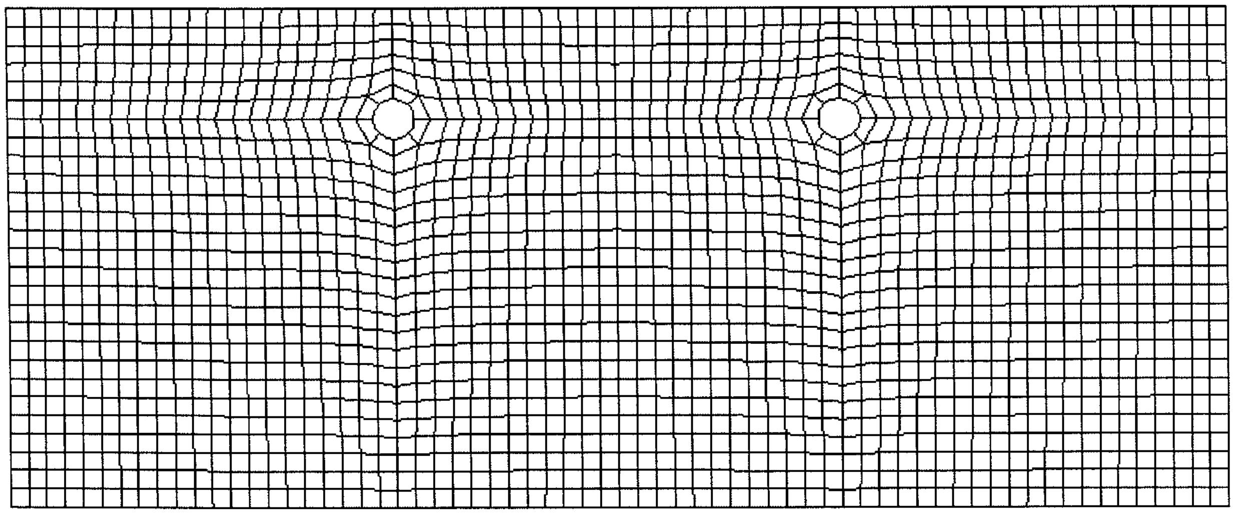

Figure 4.4: Finite element mesh for CPE8 and CPE8R

Since the uniform displacement increments used to simulate corrosion build-up on the rebar surface should be applied on every node of the finite elements along the rebar surface, and the second-order element (CPE8 and CPE8R) has a middle node between every two corner nodes. In order to maintain the same displacement conditions, the number of elements along the rebar surface for the first-order element (CPE4 and CPE4R) mesh (Figure 4.3a) should be doubled compared to that in the second-order element (CPE8 and CPE8R) mesh (Figure 4.3b). Therefore, the number of elements in Figure 4.3a is almost two times that in Figure 4.3b. Even though the elements number was doubled in CPE4 and CPE4R mesh, the CPU time and computer memory used did not increase compared to those in the CPE8 and CPE8R mesh. This is due to the fact that the number of integration points in the first-order element is almost half of that in the second-order element, and that the element stiffness matrix is calculated by using numerical integration at the integration points.

The performance of both meshes (Figure 4.3a and Figure 4.3b) was established by using the damaged plasticity model for concrete. Comparison with the smeared crack model for concrete is established in Section 4.4.3.

As explained in Section 3.4, the concrete damaged plasticity model uses the tensile equivalent plastic strain $\tilde{\varepsilon}_t^{pl} > 0$ to define concrete cracking. From Eq. (3.51), the tensile equivalent plastic strain rate equates to a nonzero weight factor times the maximum plastic strain rate. If the maximum plastic strain is positive, concrete cracking is initiated. The direction of the vector normal to the crack plane is assumed to be parallel to the direction of the maximum principal plastic strain. This direction can be visualized in figures Figure 4.5 to Figure 4.12 by using the Visualization module of ABAQUS/CAE.

Using the Visualization module of ABAQUS/CAE, the initiation and development of cracks could be observed by increasing the radial corrosion build-up of the rebar as node displacements along the rebar surface step by step. Different failure mechanisms can be observed as corrosion build-up is increased: (1) cracking initiation at the concrete/steel interface; (2) longitudinal cracking on the surface along the reinforcement; (3) spalling of the concrete cover; and, (4) delamination of the concrete cover. The corresponding radial corrosion build-up was obtained by multiplying the time step at such cracking pattern to the radial corrosion build-up increment. The cracking patterns and the corresponding levels of radial corrosion build-up of rebar are illustrated in Figures 4.5, Figure 4.6, Figure 4.7, and Figure 4.8 for different types of elements.

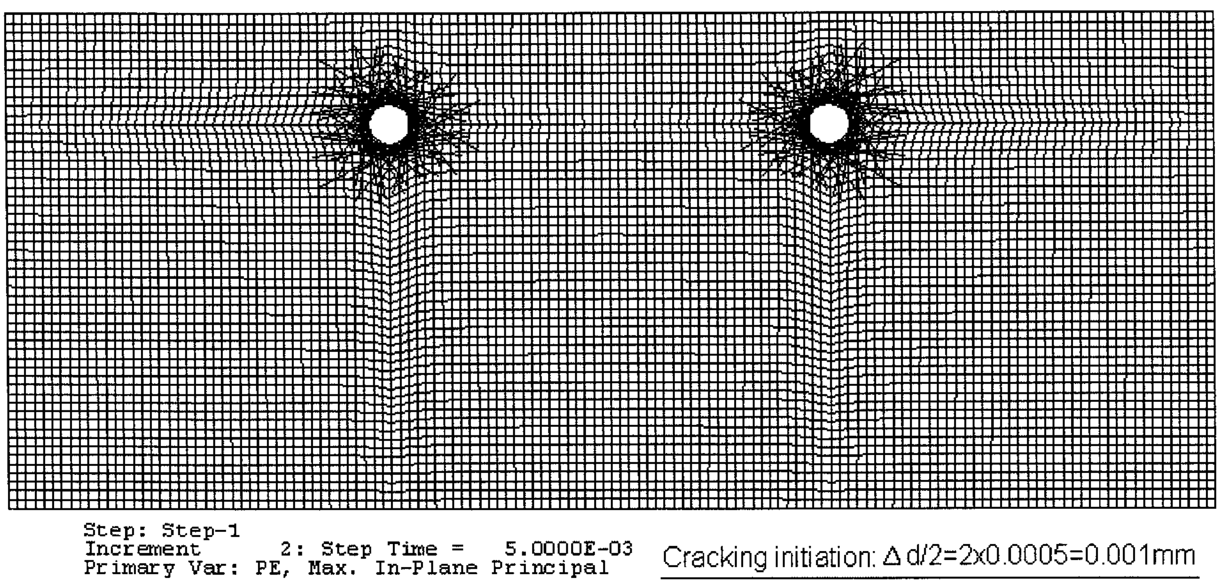

Figure 4.5: Cracking initiation using the CPE4 and CPE4R mesh

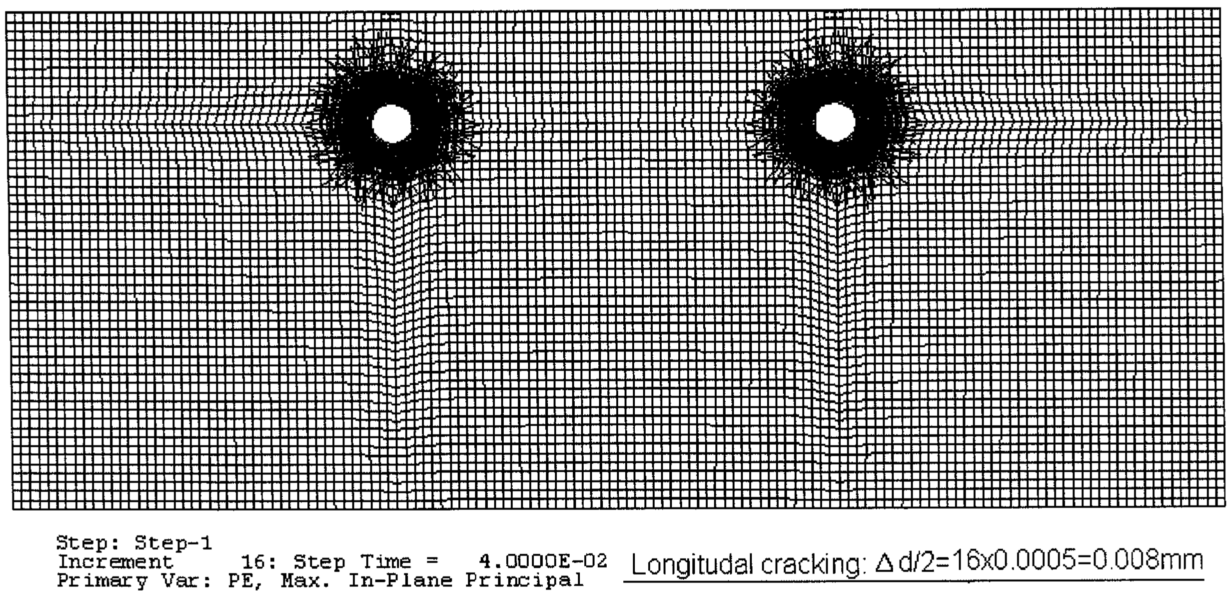

Figure 4.6: Longitudinal cracking using CPE4 and CPE4R mesh

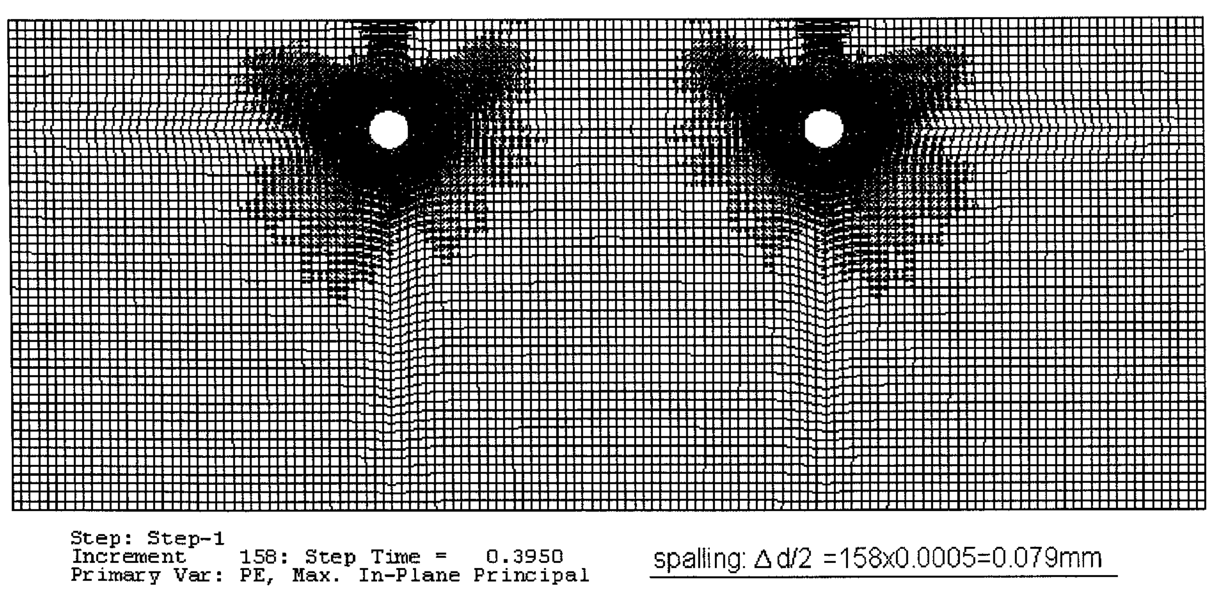

Figure 4.7: Spalling of the concrete cover using the CPE4 and CPE4R mesh

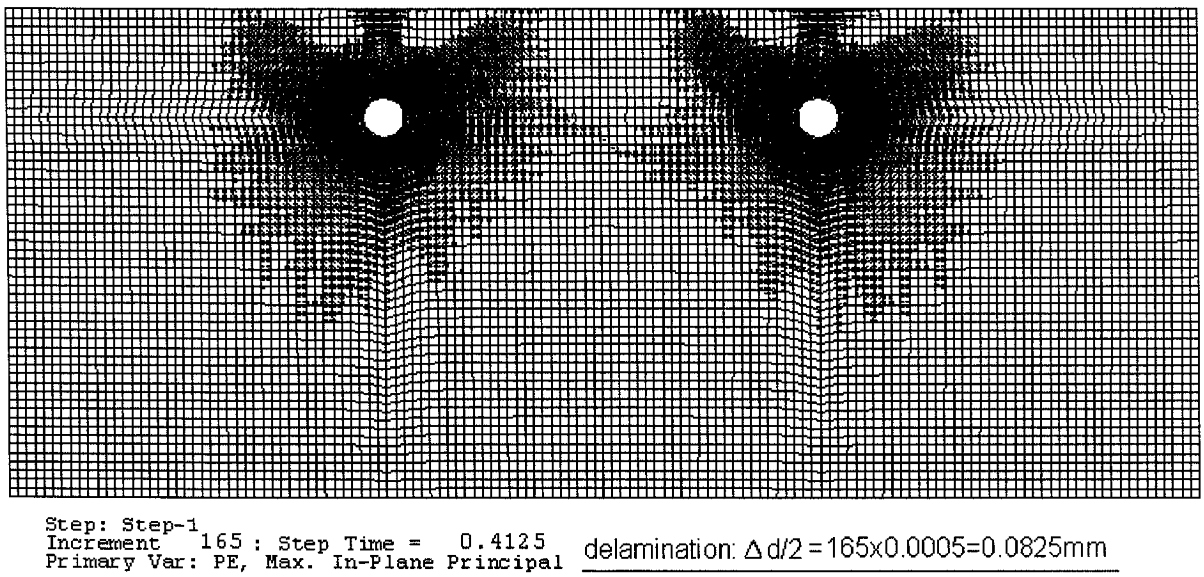

Figure 4.8: Delamination of the concrete cover using the CPE4 and CPE4R mesh

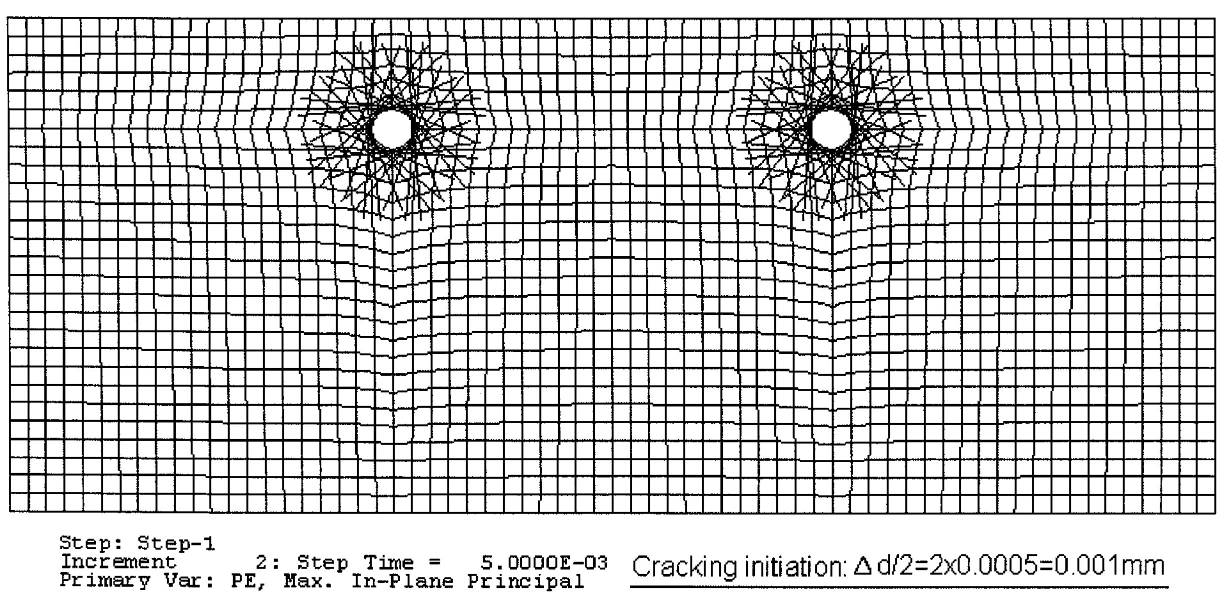

Figure 4.9: Cracking initiation by using the CPE8 and CPE8R mesh

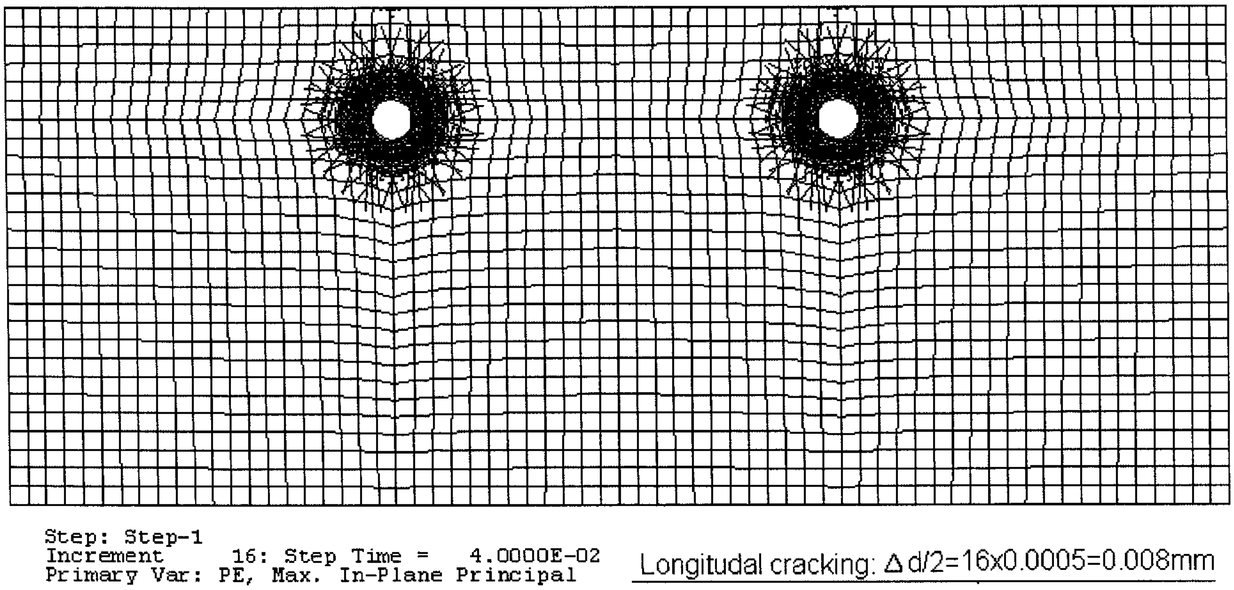

Figure 4.10: Longitudinal cracking by using the CPE8 and CPE8R mesh

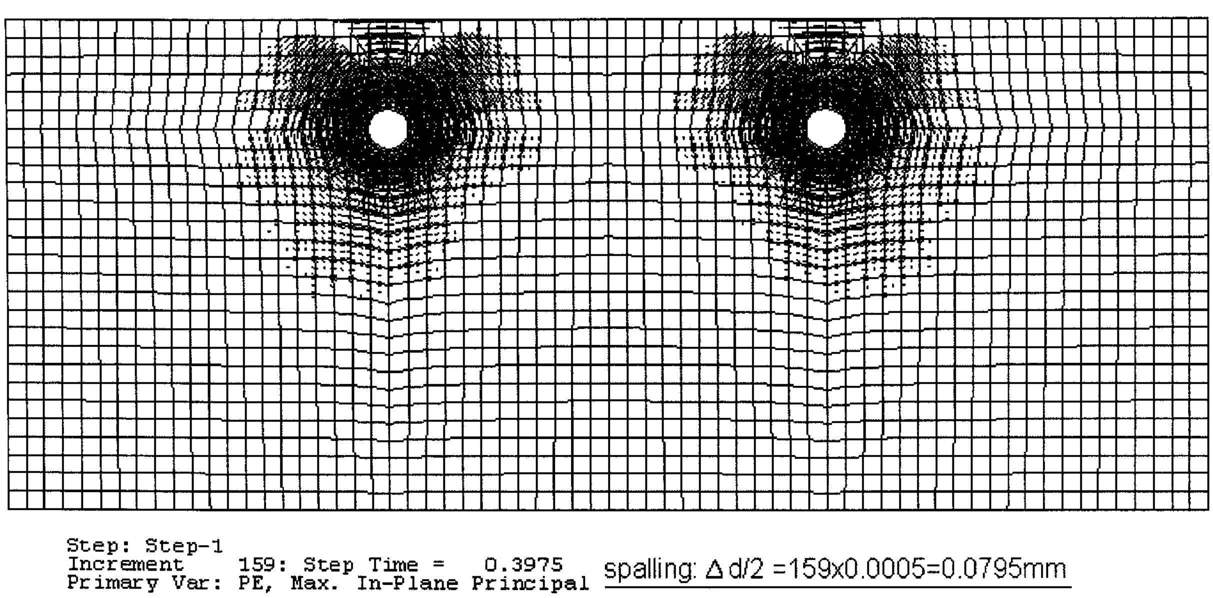

Figure 4.11: Spalling of the concrete cover by using the CPE8 and CPE8R mesh

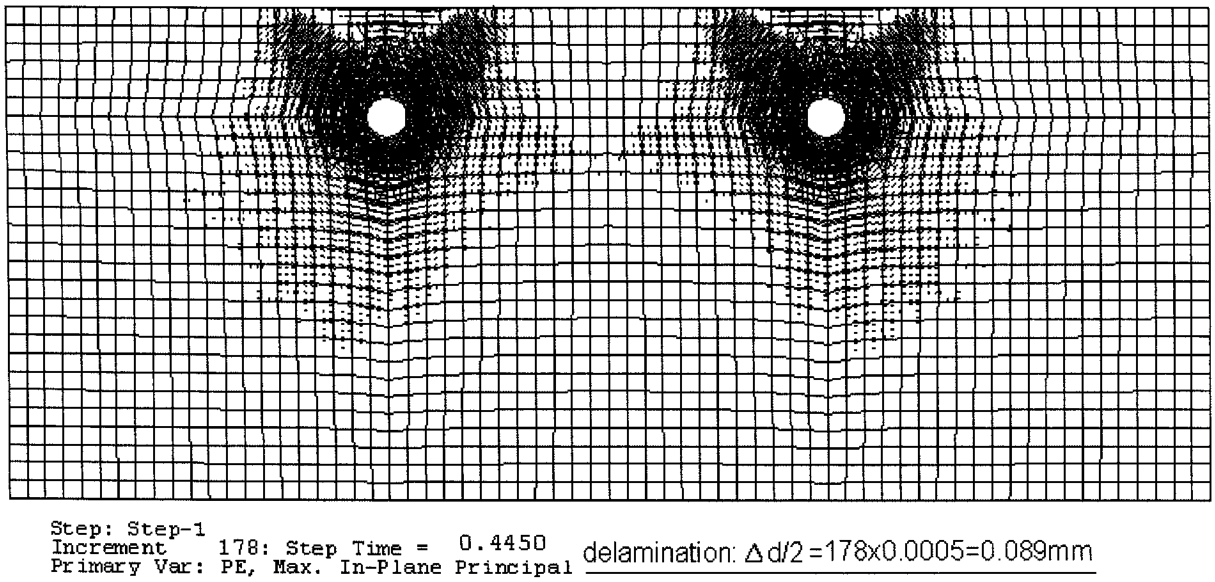

Figure 4.12: delamination of the concrete cover by using the CPE8 and CPE8R mesh

From the previous analyses, it was found that the level of corrosion build-up that caused cracking initiation, longitudinal cracking and spalling of the concrete bridge deck had almost the same values for the different meshes. Only when delamination happened, the values of the corrosion build-up with different finite elements differed by 7.3%. Because the plastic strains showed in Figure 4.5 to Figure 4.12 were all calculated at the integration points of the elements and in first-order and second-order elements, the Barlow points are found from these integration points, the similar results for the plastic strain at the integration points of these elements are expected.

However, the stress distribution varied significantly with the different types of elements. Different paths as illustrated in Figure 4.13 were selected to plot the stress distribution at different levels of corrosion build-up. Note that σ_{11} and σ_{22} in Figure 4.13 denote maximum and minimum principle stresses. The stress distributions along these paths using the different types of element are shown in Figure 4.15-Figure 4.25

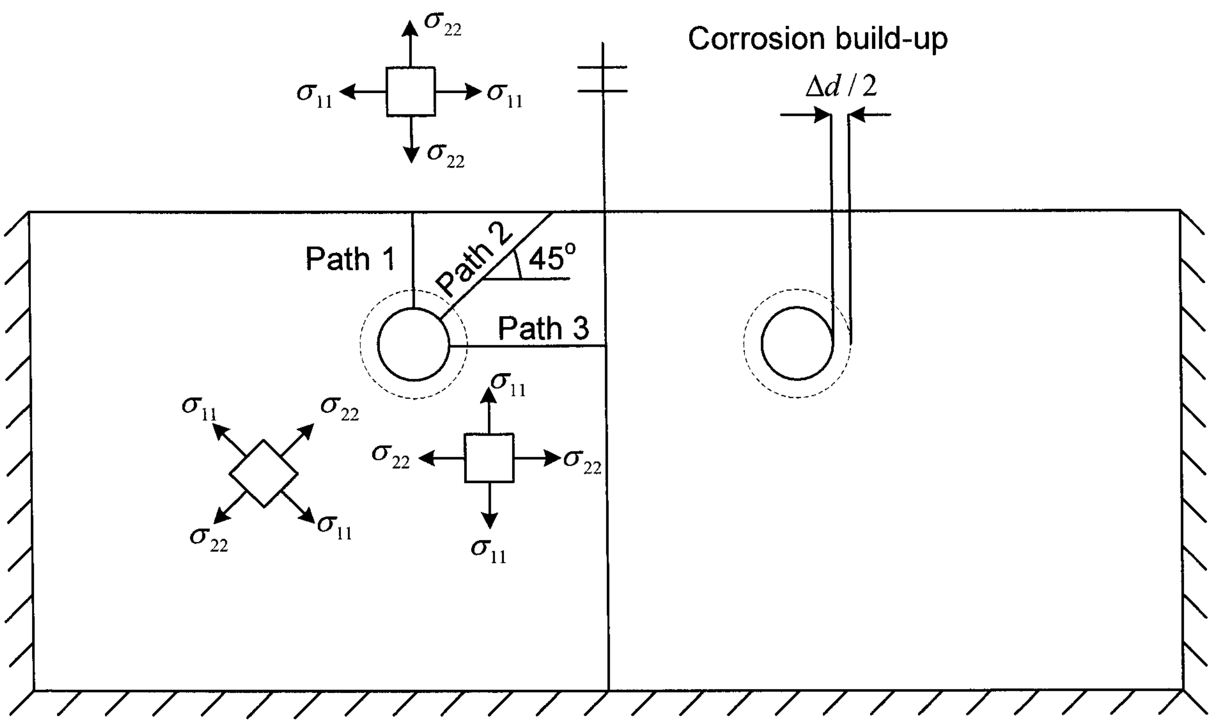

Figure 4.13: Stress distribution paths

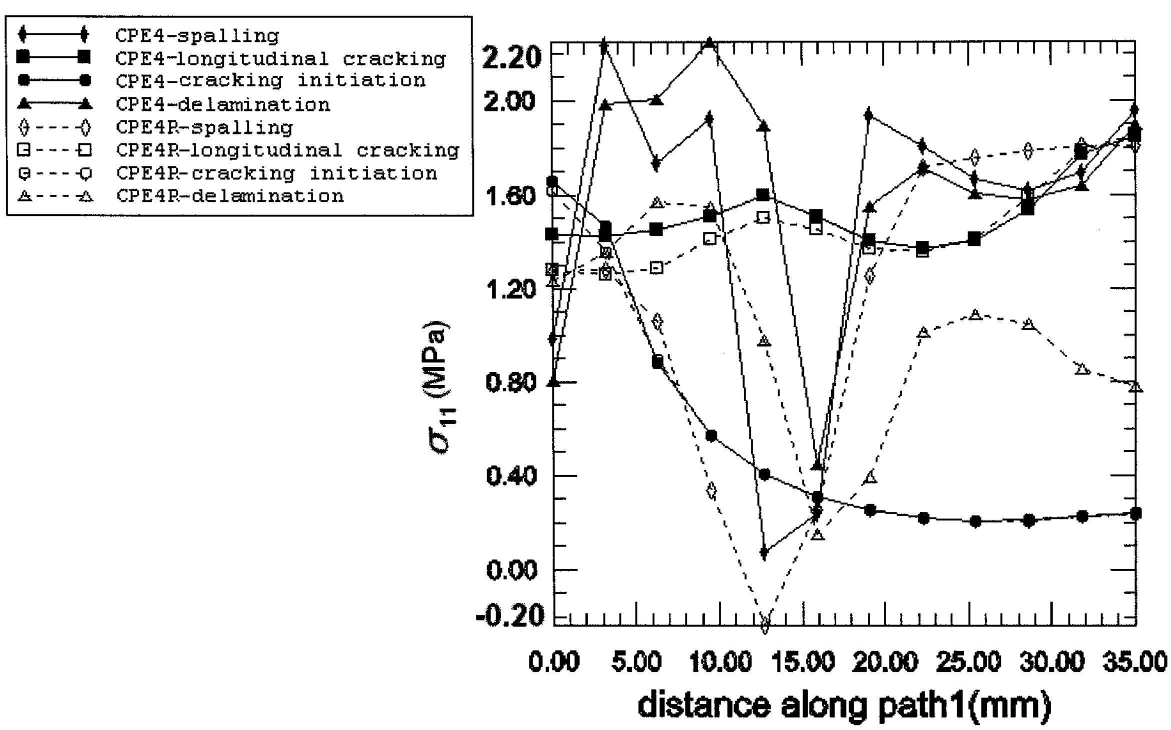

Figure 4.14: Tensile stress σ_{11} along path 1 using the CPE4, CPE4R mesh

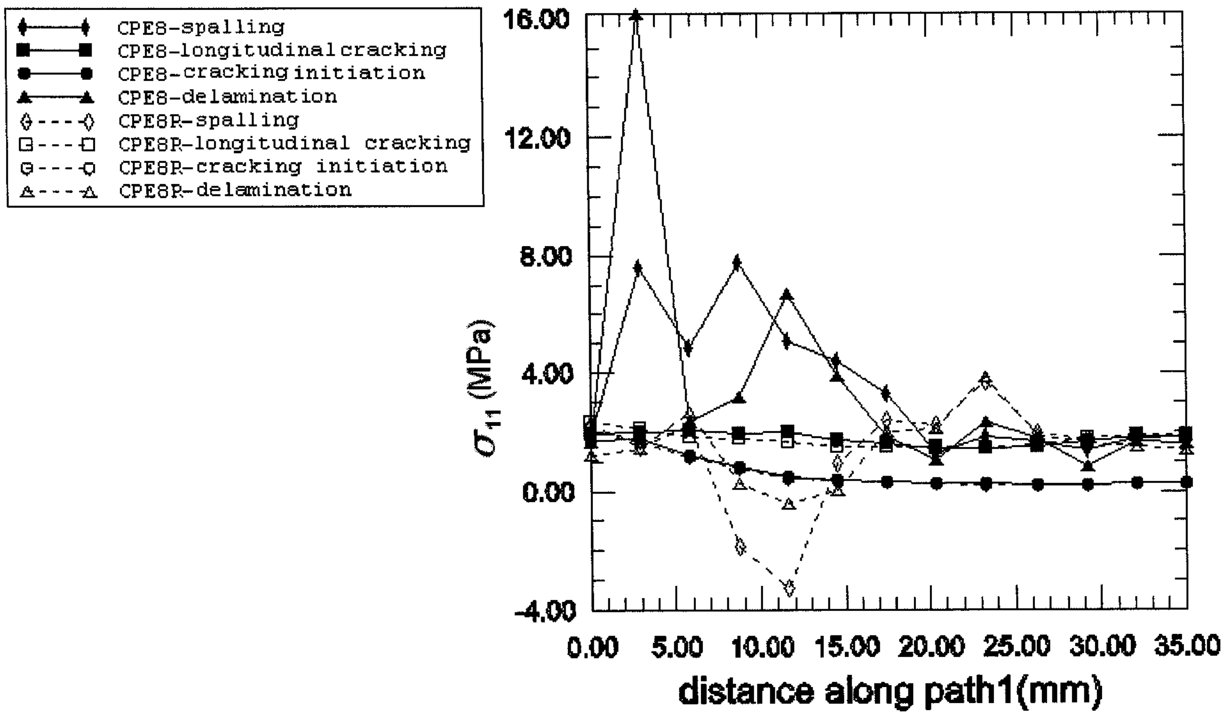

Figure 4.15: Tensile stress σ_{11} along path 1 with CPE8, CPE8R mesh

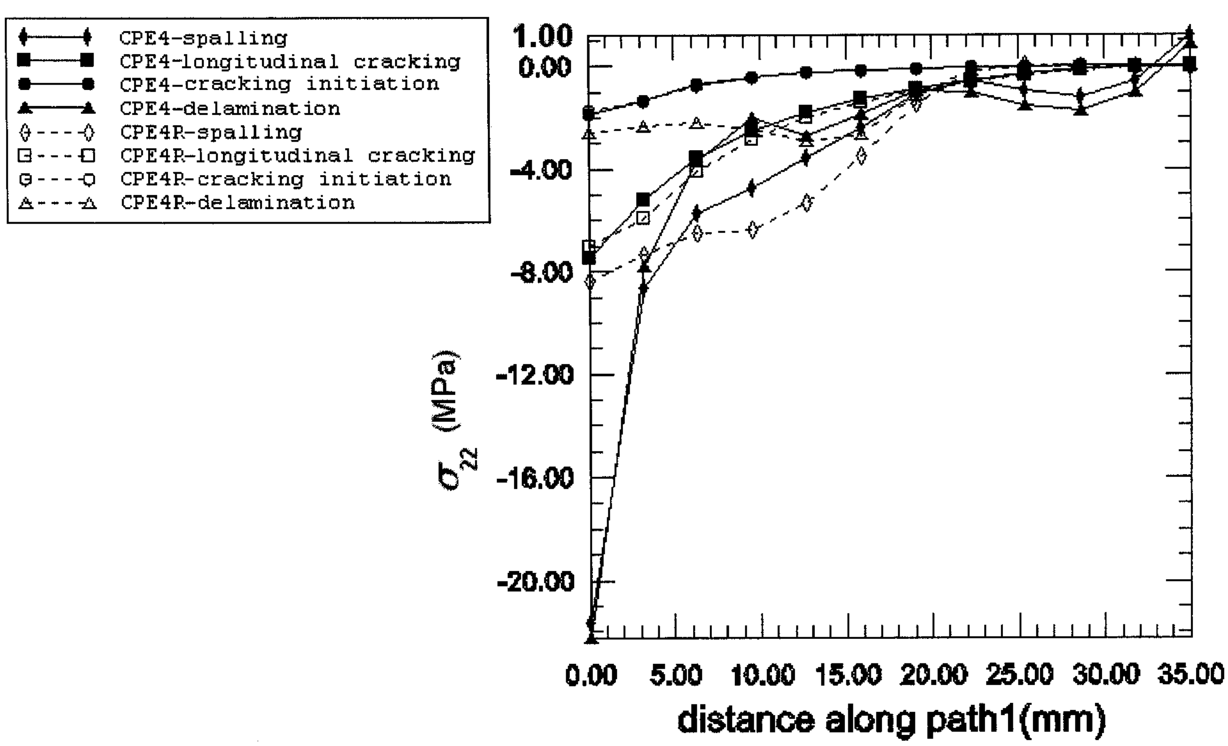

Figure 4.16: Compressive stress σ_{22} along path 1 using the CPE4, CPE4R mesh

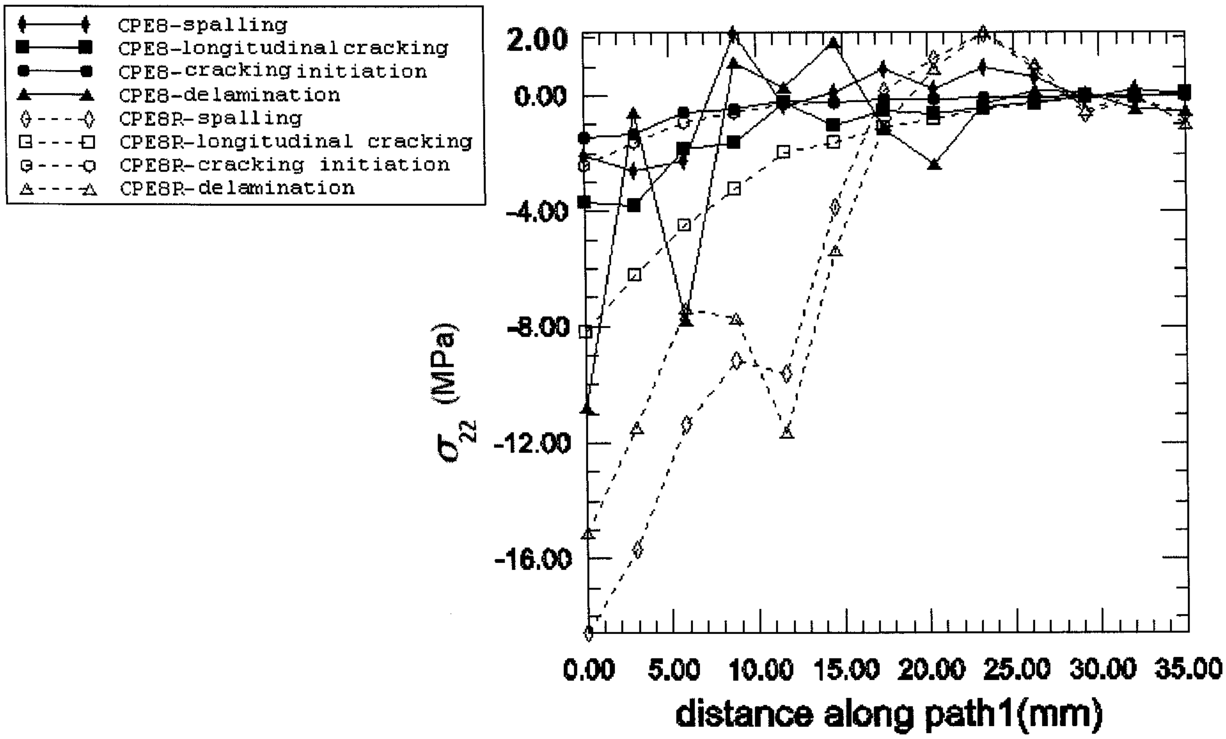

Figure 4.17: Compressive stress σ_{22} along path 1 with CPE8, CPE8R mesh

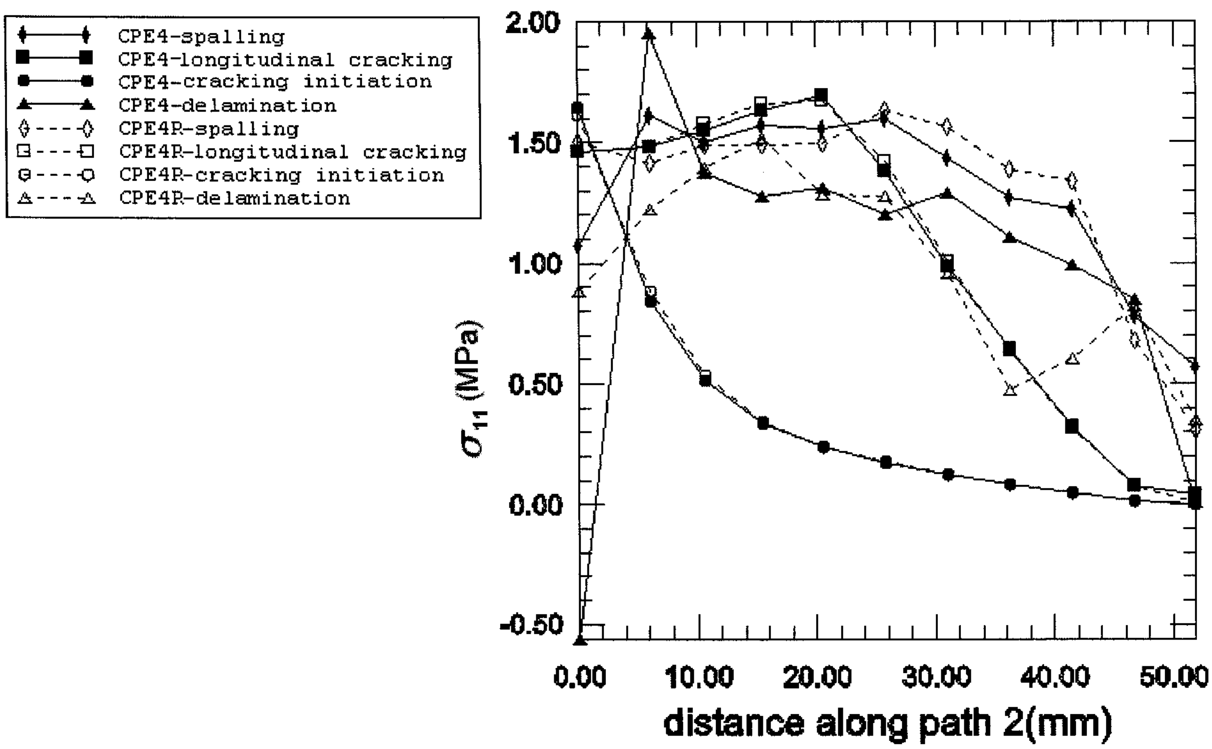

Figure 4.18: Tensile stress σ_{11} along path 2 with CPE4, CPE4R mesh

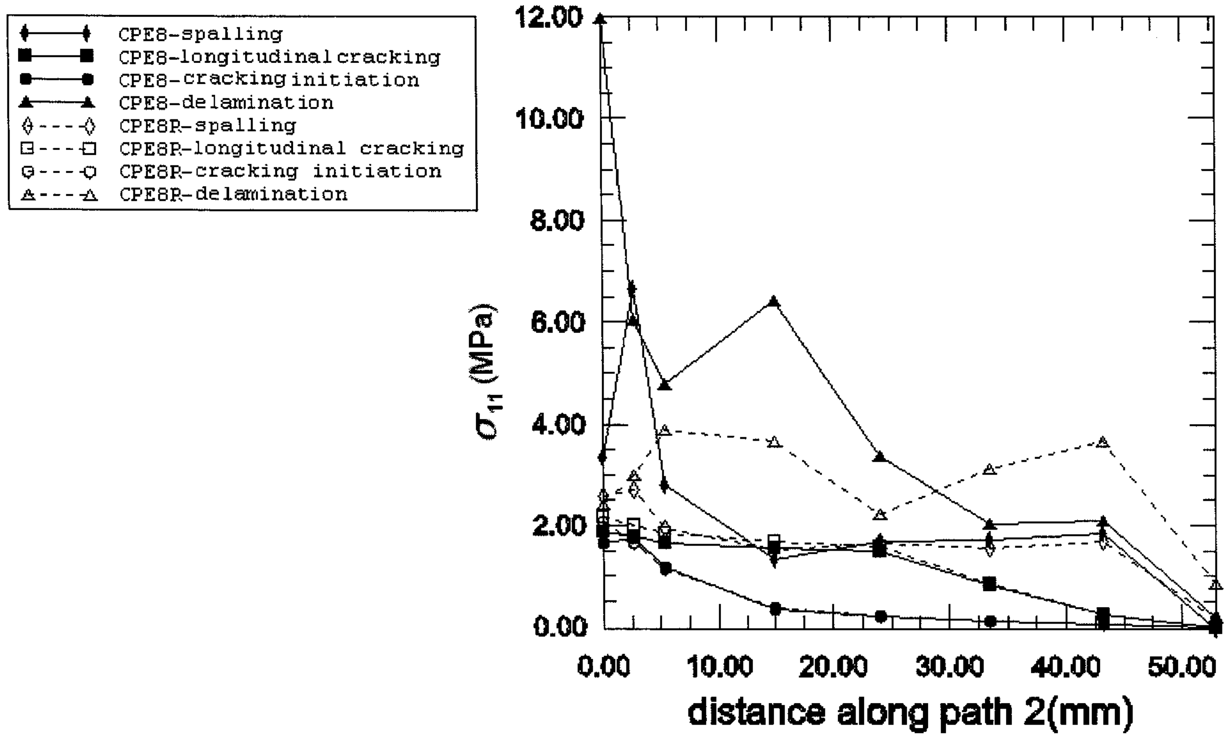

Figure 4.19: Tensile stress σ_{11} along path 2 with CPE8, CPE8R mesh

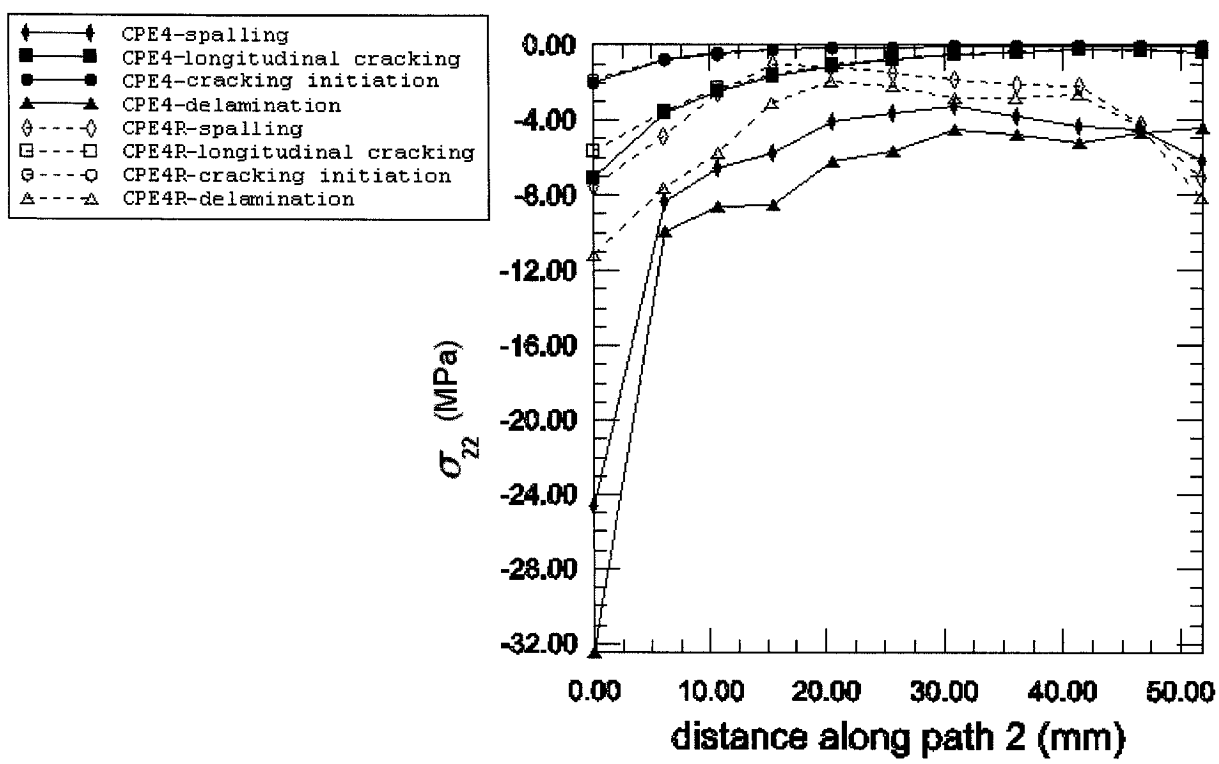

Figure 4.20: Compressive stress σ_{22} along path 2 with CPE4, CPE4R mesh

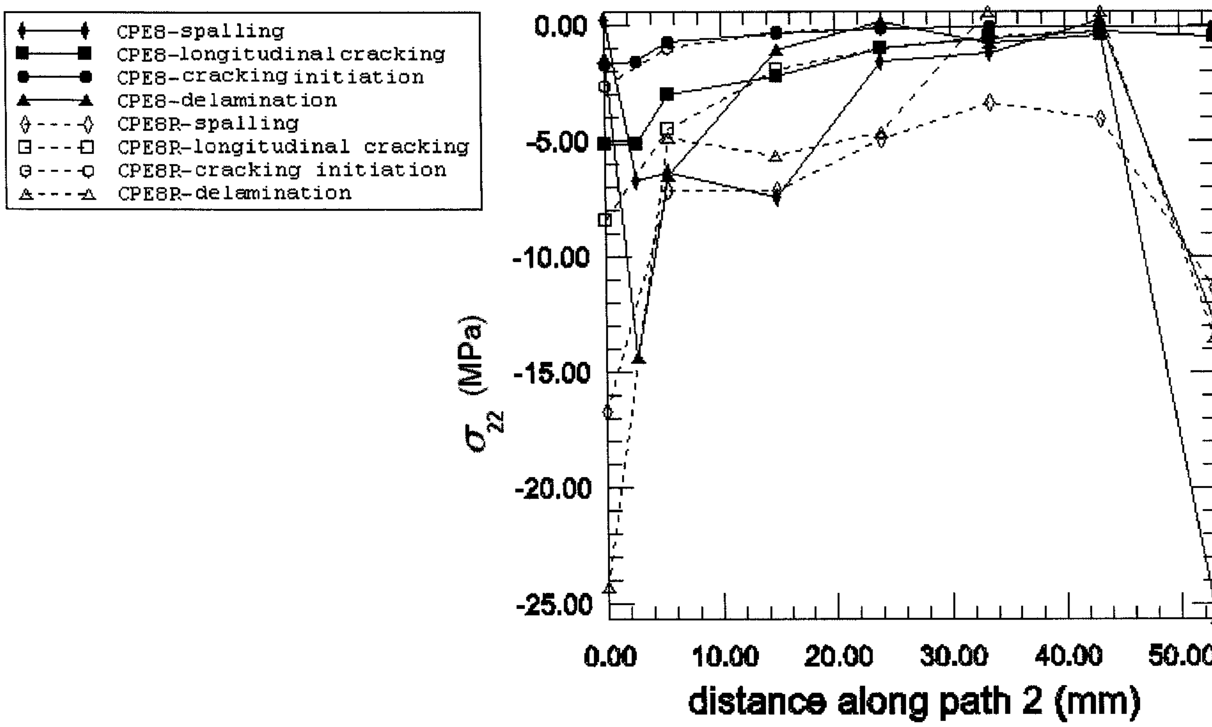

Figure 4.21: Compressive stress σ_{22} along path 2 with CPE8, CPE8R mesh

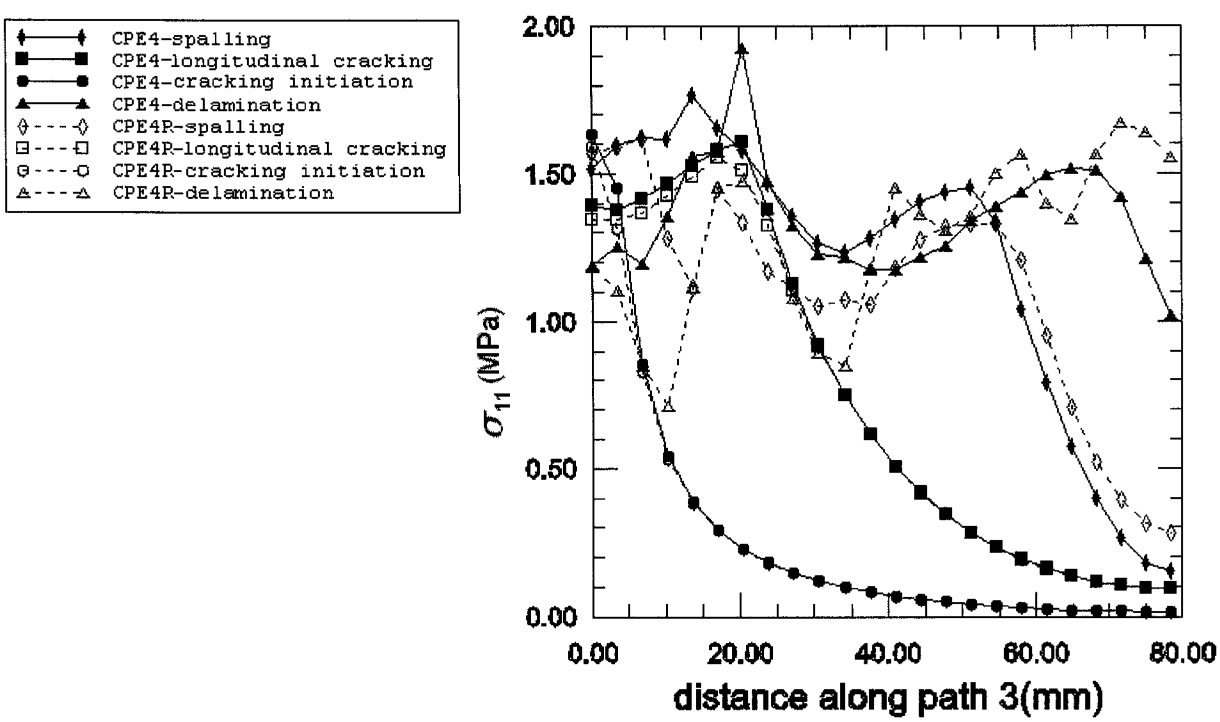

Figure 4.22: Tensile stress σ_{11} along path 3 with CPE4, CPE4R mesh

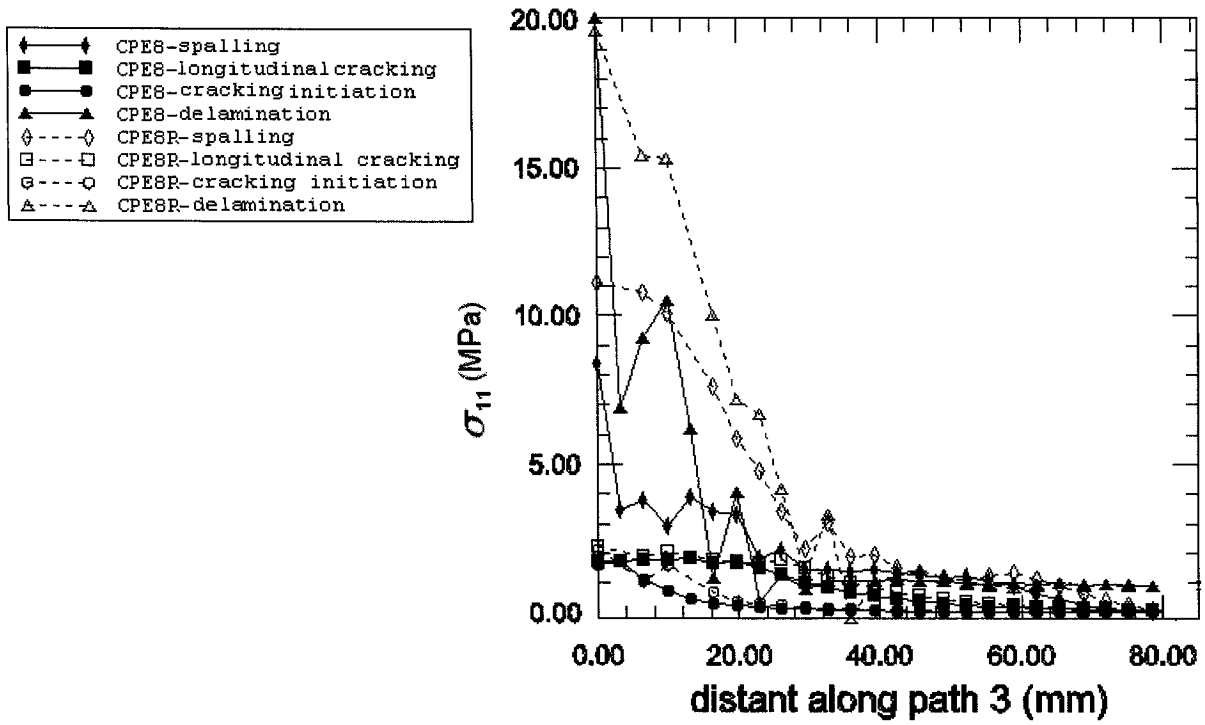

Figure 4.23: Tensile stress σ_{11} along path 3 with CPE8, CPE8R mesh

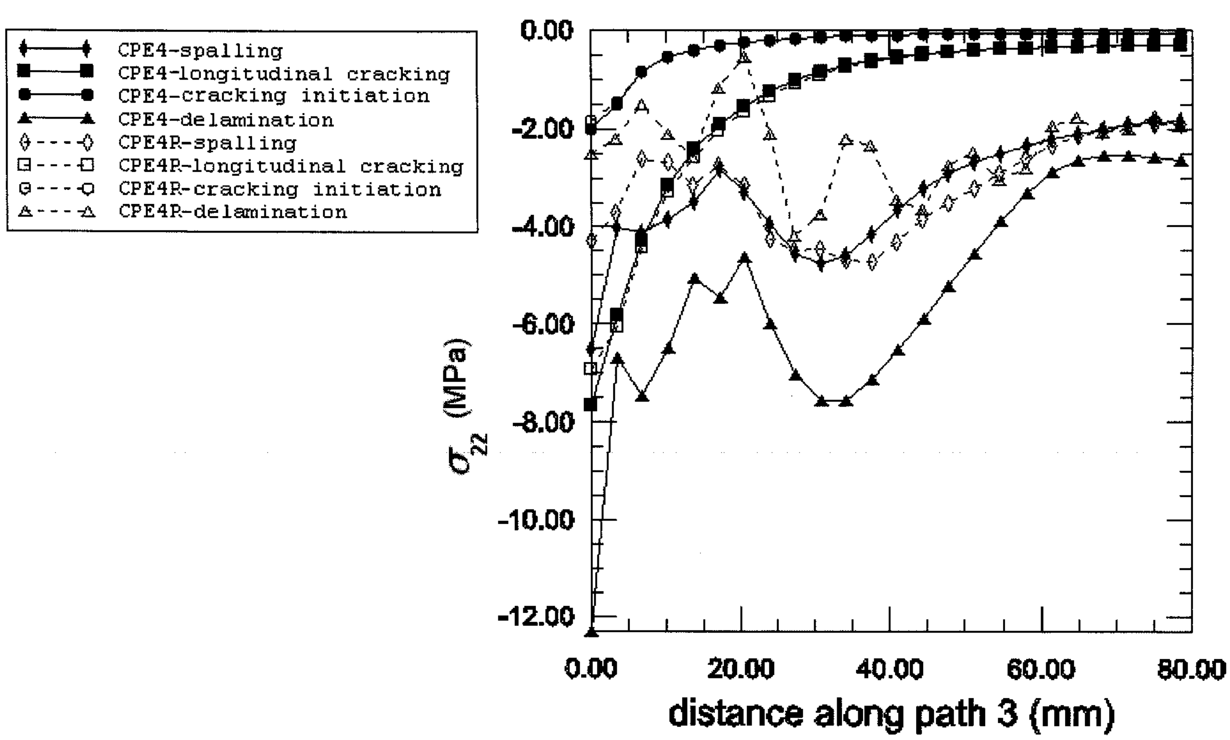

Figure 4.24: Compressive stress σ_{22} along path 3 with CPE4, CPE4R mesh

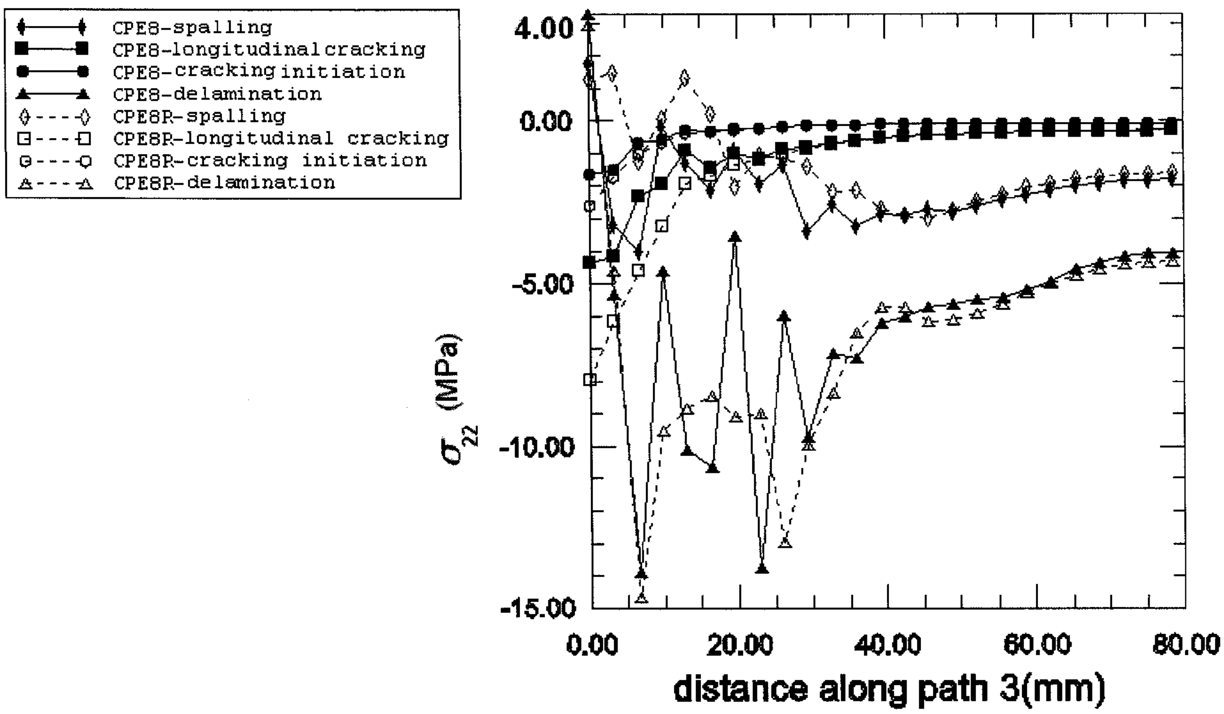

Figure 4.25: Compressive stress σ_{22} along path 3 with CPE8, CPE8R mesh

In the damaged plasticity model for concrete, the uniaxial tensile strength of concrete was defined as σ_{t0}. In multiaxial stress conditions, a yield function proposed by Lubliner et al. (1989) which incorporates the modifications proposed by Lee and Fenves (1998) was introduced to account for the different evolution of strength of concrete under tension and compression. In this yield function the maximum principal tensile stress under multiaxial stress conditions σ_{11} should not exceed σ_{t0}. In this analysis, σ_{t0} was selected as $\sigma_{t0} = 0.33\sqrt{f_c^{'}} = 1.807\text{MPa}$. It was found that using the 4-nodes first-order element with reduced integration (CPE4R) produced a more realistic principal tensile stress σ_{11} distribution along the three paths shown in figure 4.13. Using other types of elements resulted in tensile stresses much higher than σ_{t0}. This could be explained by the suggestions 2 mentioned above.

In Figure 4.16 and Figure 4.17, Figure 4.20 and Figure 4.21, Figure 4.24 and Figure 4.25, σ_{22} was the minimum principle stress that is orthogonal to σ_{11}, and σ_{22} should be compressive stress. With the developing of the cracks from the area that was close to the rebar to the longitudinal of the deck and connecting of the cracks together at last, i.e., the deck was undergoing initial cracking, longitudinal cracking, spalling and delamination,(See Figure 4.5 to Figure 4.12) the value of σ_{22} that was near the rebar should increase first then decrease afterwards, and the value of σ_{22} that was near the surface of the deck should increase from zero. This trend of the distribution of σ_{22} could only reflected by CPE4 and CPE4R.

Based on the above results, it was decided that the most suitable element for this analyses should be the 4-nodes first-order element with reduced integration (CPE4R).

4.4.3 Selection of the constitutive models for concrete

In section 4.4.2, the damaged plasticity constitutive model for concrete was used in the analysis. To decide which model best suited the problem at hand, the smeared crack constitutive model for concrete was used in this section. The parameters of the finite element mesh were the same as those used in section 4.4.2 except the material constitutive data. The uniaxial stress–strain curve was the same as that of the damaged plasticity constitutive model, but the theories of these two constitutive models are different. (See Chapter 3).

Numerical difficulties were encountered by using the smeared crack model: there was no convergence in the results at levels of radial corrosion build-up of the reinforcing bar approximately 10% to 20% of the total value compared to the results obtained using the damaged plasticity constitutive model. It predicted similar corrosion build-up levels for cracking initiation and longitudinal cracking to the damaged plasticity constitutive model, but it could not proceed when the corrosion build-up level was far beyond these values. It is for this reason that the damaged plasticity constitutive model was preferred to simulate concrete behavior.

4.4.4 Selection of the parameter a

In order to verify the selection of a=150mm that made the finite element model independent to the location of the boundary, other values were selected as: a=135mm and a=110mm to construct the finite element mesh. Except for the values of a, other parameters are identical to the mesh used in section 4.4.2.

As discussed previously, 4-nodes first-order element with reduced integration (CPE4R) and the damaged plasticity model for concrete are used in the finite element analyses.

The analysis showed that these two meshes gave the same values of the radial corrosion build-up that causes cracking initiation, longitudinal cracking, spalling and delamination of the concrete deck cover as shown in Figure 4.5 to Figure 4.8.

The cracking patterns and the corresponding level of radial corrosion build-up of rebar with different values of a are presented in Figure 4.26, Figure 4.27, Figure 4.28, Figure 4.29, Figure 4.30, Figure 4.31, Figure 4.32, and Figure 4.33. The distribution of stresses σ_{11} and σ_{22} along path 1 are plotted in Figure 4.34 and Figure 4.34.

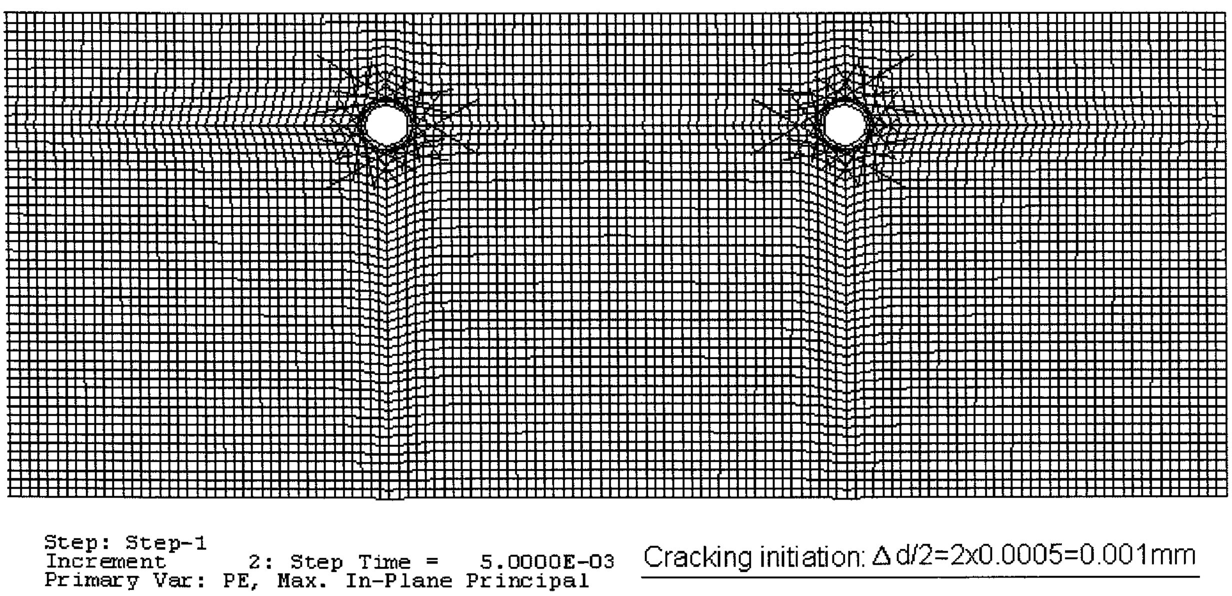

Figure 4.26: Cracking initiation by using the CPE4R mesh and $a = 135\text{mm}$

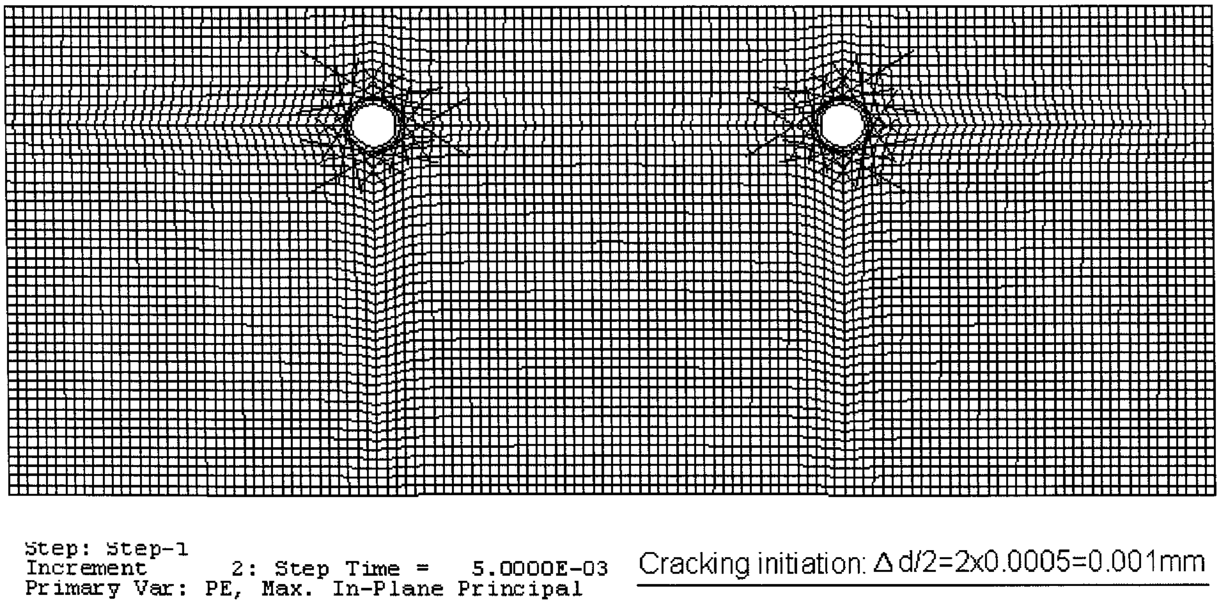

Figure 4.27: initial cracking by using the CPE4R mesh and $a = 110\text{mm}$

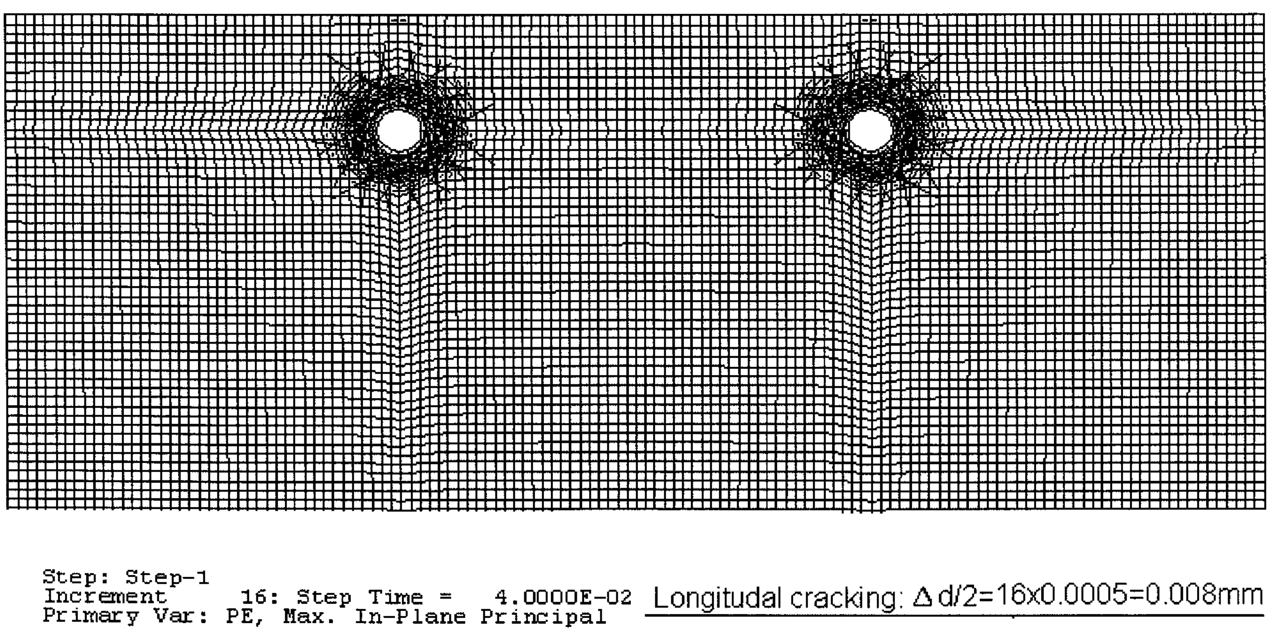

Figure 4.28: longitudinal cracking by using the CPE4R mesh and $a = 135\text{mm}$

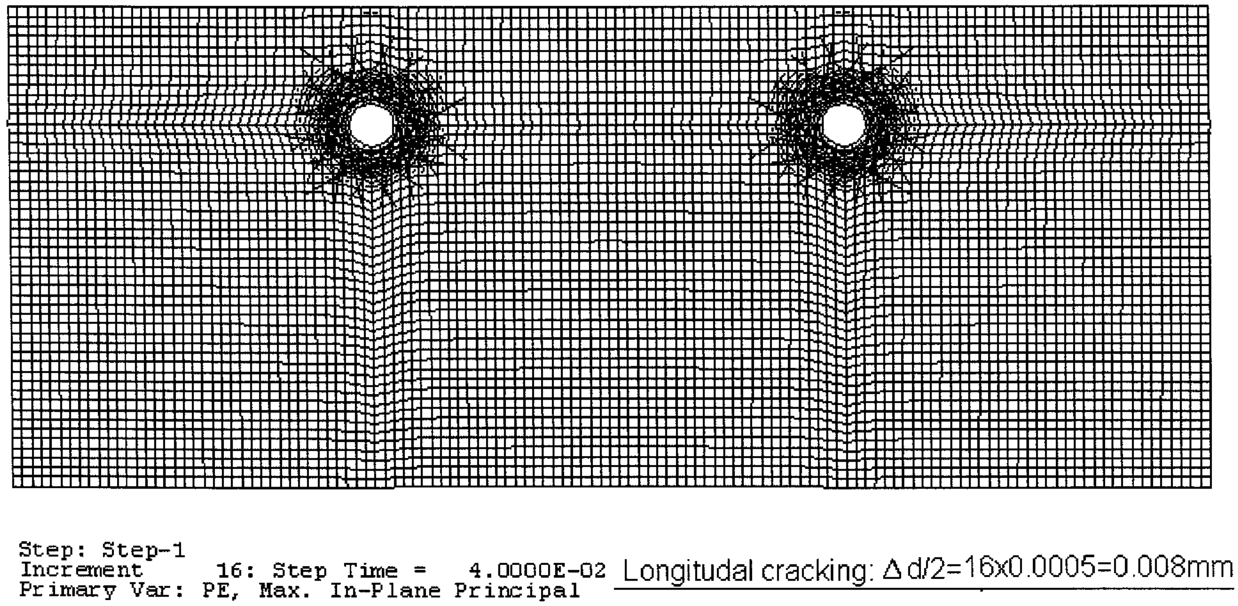

Figure 4.29: longitudinal cracking by using CPE4R mesh and $a = 110\text{mm}$

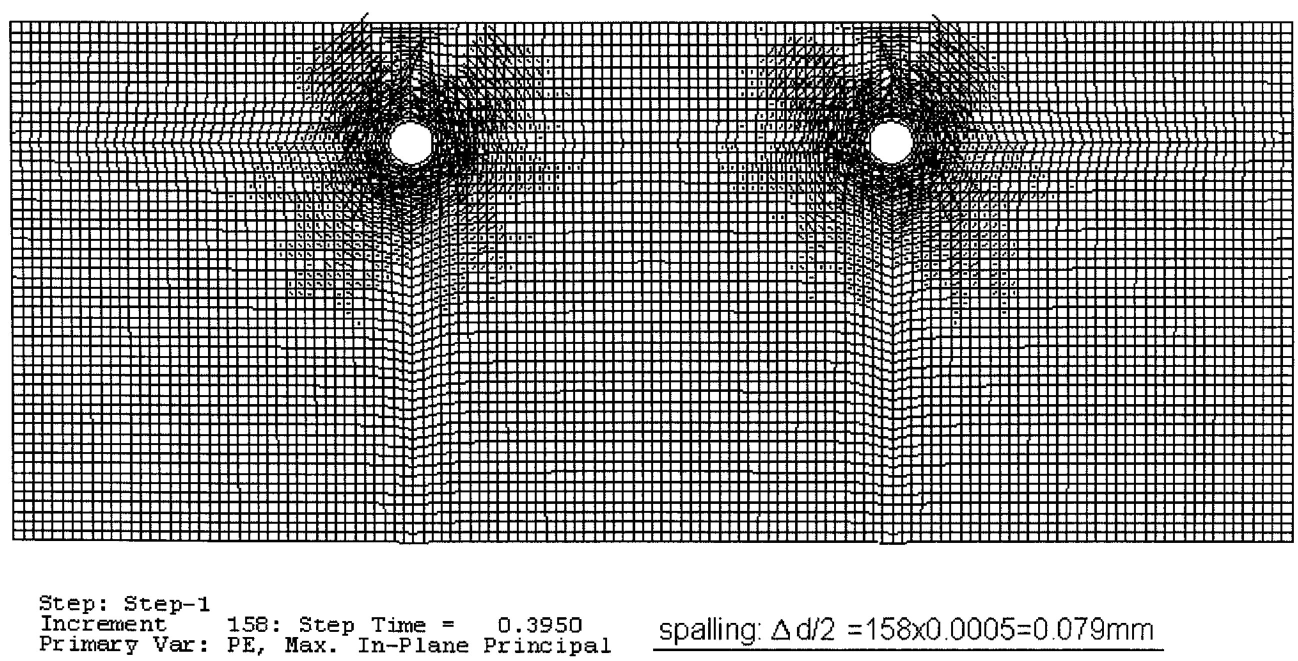

Figure 4.30: spalling by using CPE4R mesh and $a = 135\text{mm}$

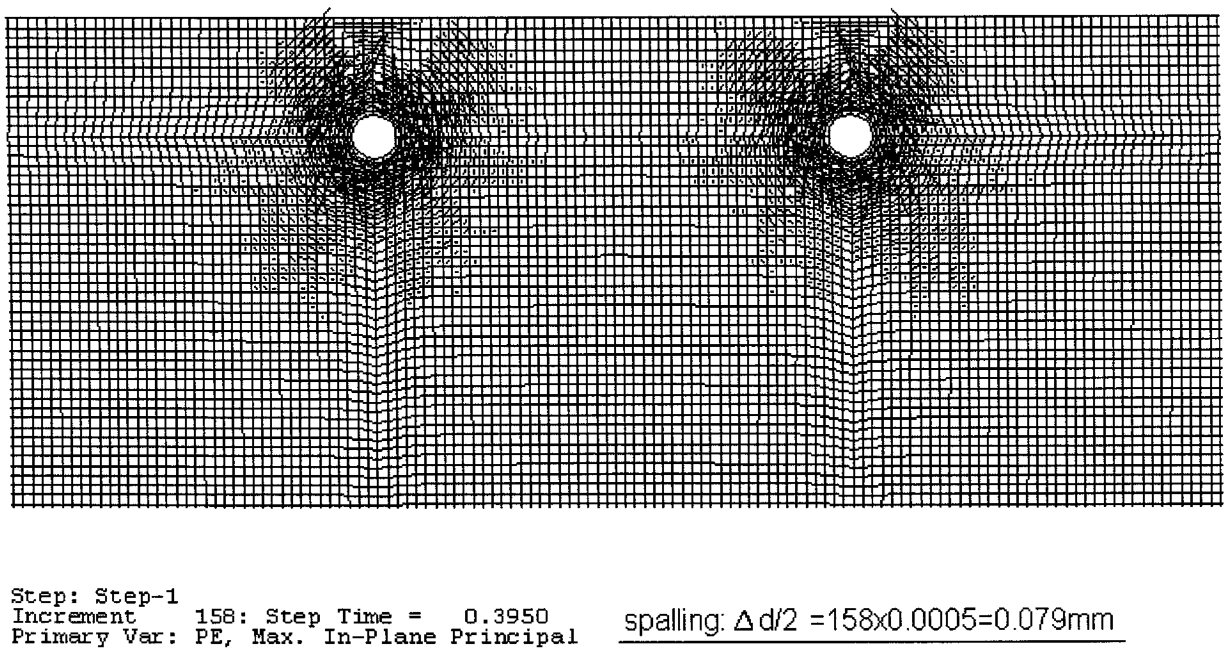

Figure 4.31: spalling by using CPE4R mesh and $a = 110\text{mm}$

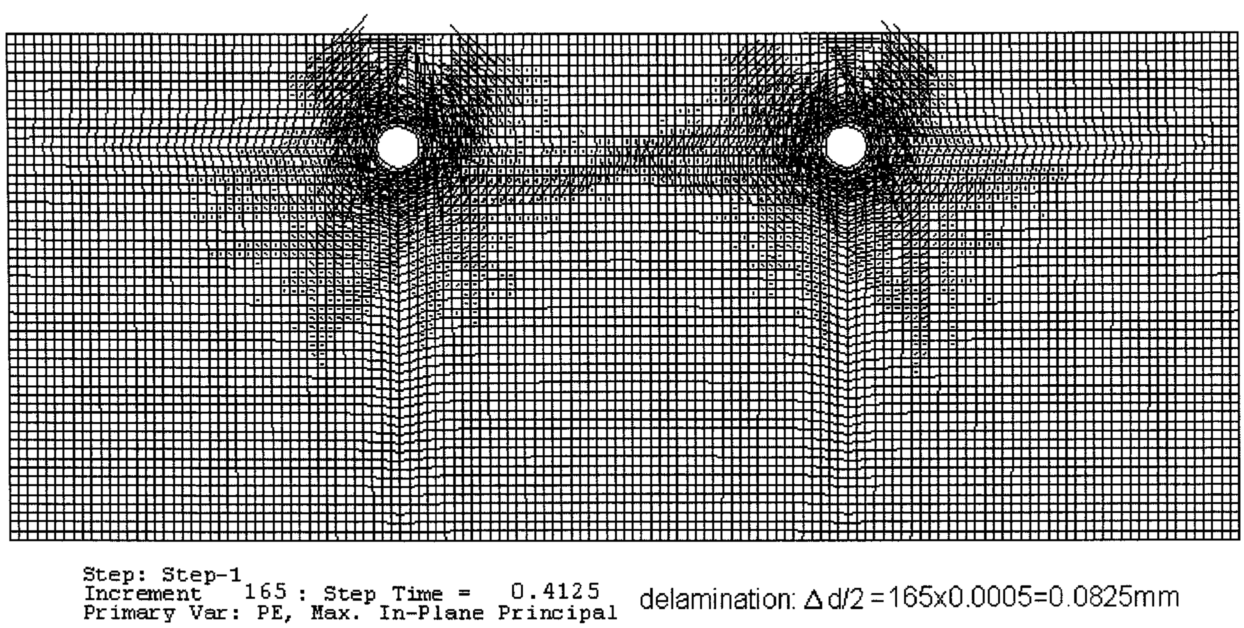

Figure 4.32: delamination by using CPE4R mesh and $a = 135\text{mm}$

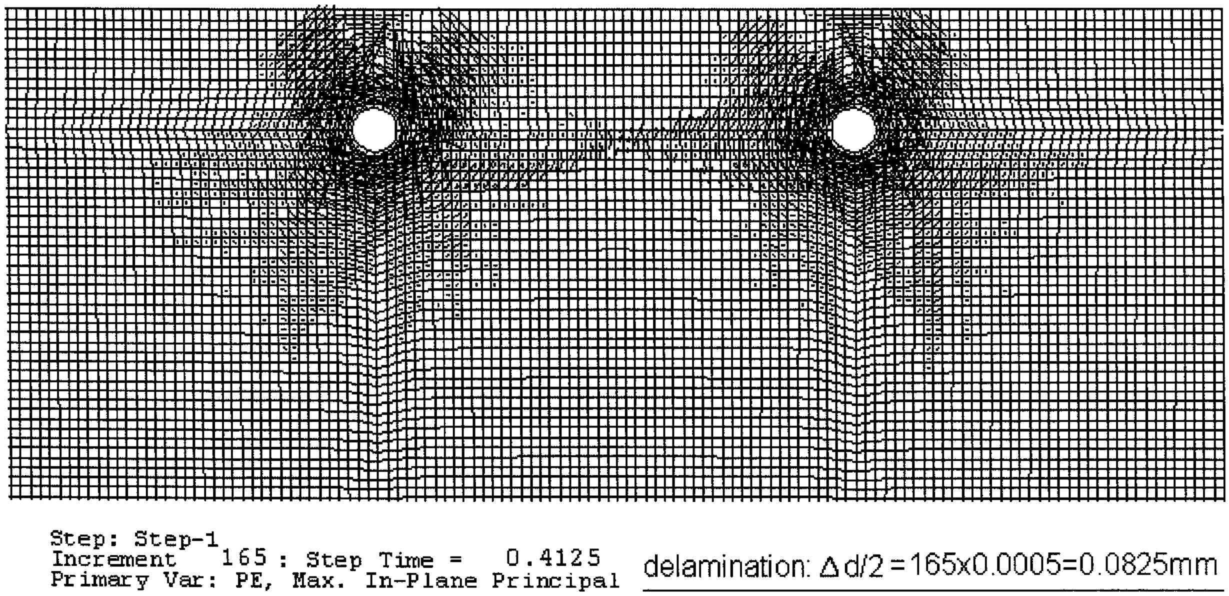

Figure 4.33: delamination by using CPE4R mesh and $a = 110\text{mm}$

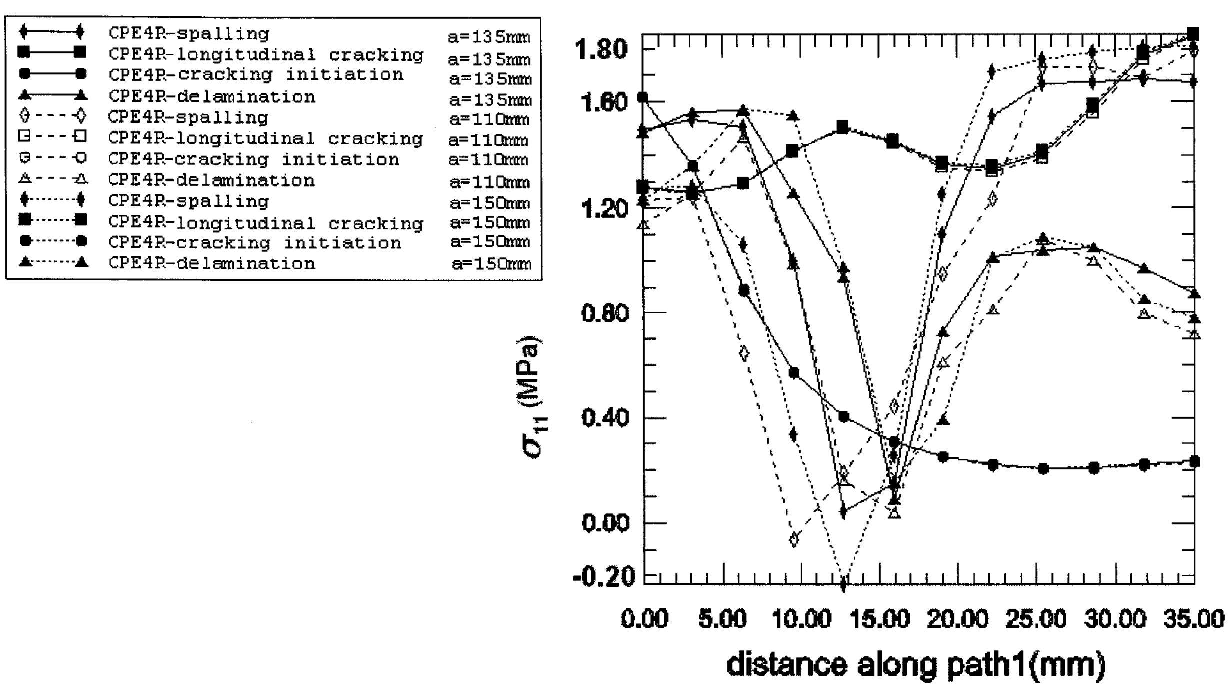

Figure 4.34: σ_{11} **along path 1 with CPE4R** $a = 110\text{mm}$ $a = 135\text{mm}$ $a = 150\text{mm}$

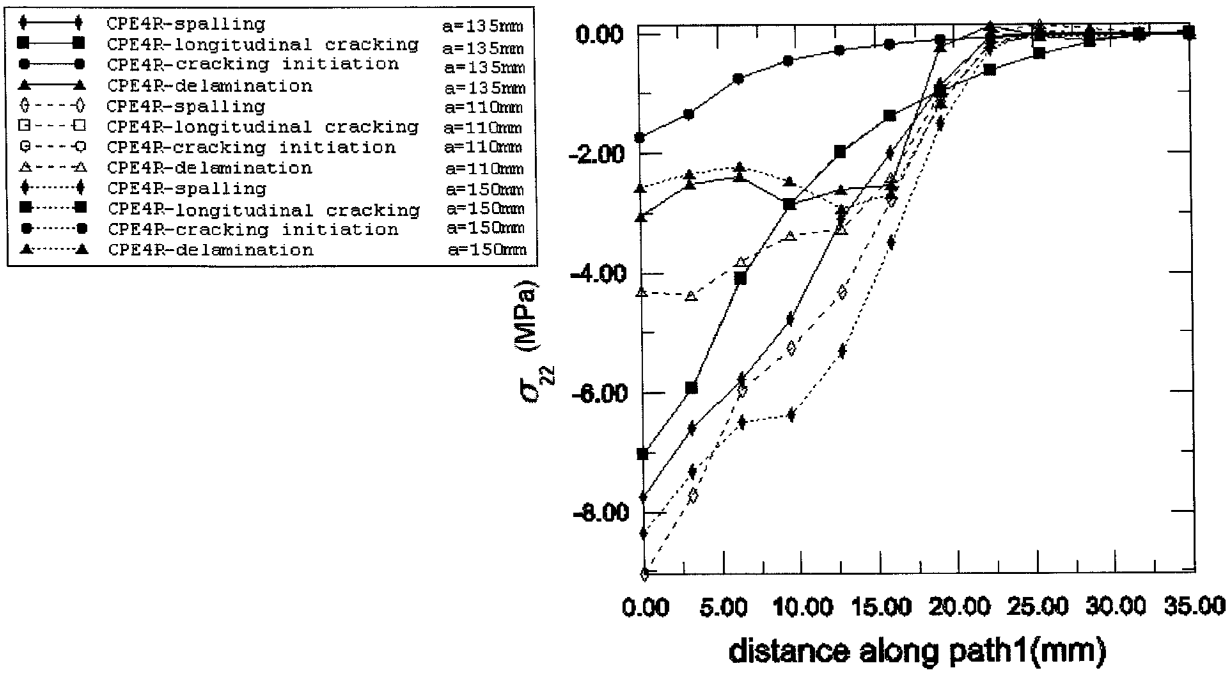

Figure 4.35: σ_{22} along path 1 with CPE4R $a = 110\text{mm}$ $a = 135\text{mm}$ $a = 150\text{mm}$

Chapter 5

Modeling unprotected rc bridge decks

5.1 Introduction

This chapter presents the results from a parametric study conducted using the finite element model for an unprotected rc bridge deck subjected to reinforcement corrosion. The parametric study was carried out to establish the different corrosion-induced failure patterns as a function of design variables *c*, *d*, and *s*. The bridge deck was assumed to be undamaged, and its material properties were taken as those presented in Chapter 4.

5.2 Numerical results

Based on the finite element model described in Chapter 4, the different failure mechanisms of the concrete bridge deck caused by the corrosion build-up of the reinforcing bars (i.e., cracking initiation, longitudinal cracking, spalling and delamination) corresponding to different geometries and rebar configurations were analyzed. The numerical results of the analyses are shown in Table 5.1 and Table 5.2, where $\Delta d_1/2$ is the level of corrosion build-up to cause cracking initiation, $\Delta d_2/2$ is the level of corrosion build-up to cause longitudinal cracking, $\Delta d_3/2$ is the level of corrosion build-up to cause spalling of the concrete cover, and $\Delta d_4/2$ is the level of corrosion build-up to cause delamination.

Table 5.1: Values of corrosion build-up causing different failure modes for rebar diameters of 11 and 16 mm

c (mm)	d (mm)	s (mm)	$\Delta d_1/2$ (mm)	$\Delta d_2/2$ (mm)	$\Delta d_3/2$ (mm)	$\Delta d_4/2$ (mm)
35	11	50	0.000800	0.011300	---	0.003900
35	11	81	0.000800	0.010600	---	0.010600
35	11	86	0.000800	0.010600	---	0.011800
35	11	92	0.000800	0.011500	---	0.014900
35	11	100	0.001000	0.011300	---	0.022700
35	11	110	0.001000	0.012000	0.071500	0.057000
35	11	120	0.001000	0.012000	0.086000	0.070000
35	11	160	0.001000	0.011500	0.099000	0.102000
50	11	80	0.000800	0.019800	---	0.009800
50	11	111	0.000800	0.017700	---	0.018300
50	11	120	0.000800	0.017500	---	0.023500
50	11	152	0.001000	0.017500	0.120000	0.091000
50	11	160	0.001000	0.017000	0.132500	0.096000
50	11	218	0.001000	0.017000	0.142000	0.145500
65	11	80	0.000800	0.026000	---	0.009900
65	11	141	0.000800	0.025800	---	0.026200
65	11	160	0.001000	0.025500	---	0.108000
65	11	195	0.001000	0.025000	0.162500	0.147000
65	11	205	0.001000	0.025000	0.176500	0.160000
65	11	275	0.001000	0.025500	0.180000	0.183500
35	16	80	0.000800	0.009000	---	0.006700
35	16	86	0.000800	0.008900	---	0.009300
35	16	105	0.000800	0.008200	---	0.014500
35	16	115	0.001000	0.008500	0.058500	0.039000
35	16	130	0.001000	0.008500	0.068000	0.046000
35	16	173	0.001000	0.008000	0.079000	0.082500
50	16	80	0.000800	0.014500	---	0.006600
50	16	116	0.000800	0.014300	---	0.014300
50	16	140	0.000800	0.013900	---	0.027500
50	16	157	0.001000	0.013000	0.130000	0.056500
50	16	170	0.001000	0.013500	0.130500	0.095000
50	16	230	0.001000	0.014500	0.161500	0.165500
65	16	80	0.000800	0.019600	---	0.006600
65	16	146	0.000800	0.020100	---	0.021000
65	16	170	0.000800	0.019700	---	0.039200
65	16	200	0.001000	0.019000	0.165500	0.121500
65	16	210	0.001000	0.019500	0.165000	0.170000

Table 5.2: Values of corrosion build-up causing different failure modes for rebar diameters of 20 and 25 mm

c (mm)	d (mm)	s (mm)	$\Delta d_1/2$ (mm)	$\Delta d_2/2$ (mm)	$\Delta d_3/2$ (mm)	$\Delta d_4/2$ (mm)
35	20	80	0.001000	0.007700	---	0.005300
35	20	90	0.001000	0.007500	---	0.007900
35	20	110	0.001000	0.007500	---	0.012300
35	20	120	0.001000	0.007500	0.087500	0.017500
35	20	130	0.001000	0.007500	0.084000	0.024000
35	20	182	0.001000	0.007000	0.118000	0.120000
50	20	80	0.001000	0.013200	---	0.005300
50	20	120	0.001000	0.013600	---	0.014400
50	20	140	0.001000	0.013500	---	0.019500
50	20	160	0.001000	0.013000	0.091500	0.036000
50	20	180	0.001000	0.013000	0.109500	0.080500
50	20	240	0.001000	0.011500	0.149000	0.153000
65	20	120	0.001000	0.021300	---	0.011700
65	20	150	0.001000	0.018200	---	0.018800
65	20	180	0.001000	0.017500	---	0.024000
65	20	204	0.001000	0.017500	0.163500	0.087000
65	20	220	0.001000	0.017500	0.166000	0.131500
65	20	297	0.001000	0.017500	0.179000	0.175000
35	25	80	0.001400	0.009300	---	0.004300
35	25	95	0.001300	0.008600	---	0.009000
35	25	130	0.001300	0.008700	---	0.017800
35	25	160	0.001500	0.008000	0.101000	0.042500
35	25	200	0.001500	0.008500	0.166000	0.171000
50	25	80	0.001200	0.012900	---	0.004100
50	25	125	0.001000	0.012900	---	0.013500
50	25	160	0.001500	0.013500	0.101500	0.087500
50	25	252	0.001500	0.010500	0.179000	0.181000
65	25	130	0.001200	0.019800	---	0.011100
65	25	155	0.001200	0.017600	---	0.018300
65	25	190	0.001500	0.018500	0.151500	0.112500
65	25	310	0.001500	0.018500	0.189000	0.195000

It was found from the analysis that cracks propagated upwardly along the radial direction after initiation of cracking at the steel/concrete interface. However, when cracks reached almost half depth of the deck cover, cracks could continue to propagate along three main directions: the vertical direction, the horizontal direction, and the 45°-direction measured from the horizontal, which respectively correspond to paths 1, 3 and 2 in Figure 4.13. Longitudinal cracking occured when cracks developed along path 1 and reached the surface of the concrete cover (see Figure 4.6). Delamination of the concrete cover occurred when two cracks initiated from the neighboring reinforcing bars' surface and propagated along path 3 towards each other (see Figure 4.8). Spalling of the concrete cover occurred when cracks developed along path 2 and reached the surface of the bridge deck (see Figure 4.7).

Corrosion-induced damage of the rc bridge deck was a combination of two failure patterns. As the rebar spacing s was increased, the following failure mechanisms were observed:

1. Delamination followed by longitudinal cracking
2. Longitudinal cracking followed by delamination
3. Longitudinal cracking followed by spalling

The actual values of s that led to the different failure modes depended on the actual concrete cover-to-rebar diameter ratio c/d and the rebar spacing-to-rebar diameter ratio s/d. A similar pattern of failure was predicted with the analytical models formulated in Chapter 3 (refer to Figure 3.8). Whether failure mode 1 governed over failure mode 2 depended on the lengths of paths 1 and 3, L_1 and L_3, respectively, as illustrated in Figure 5.1.

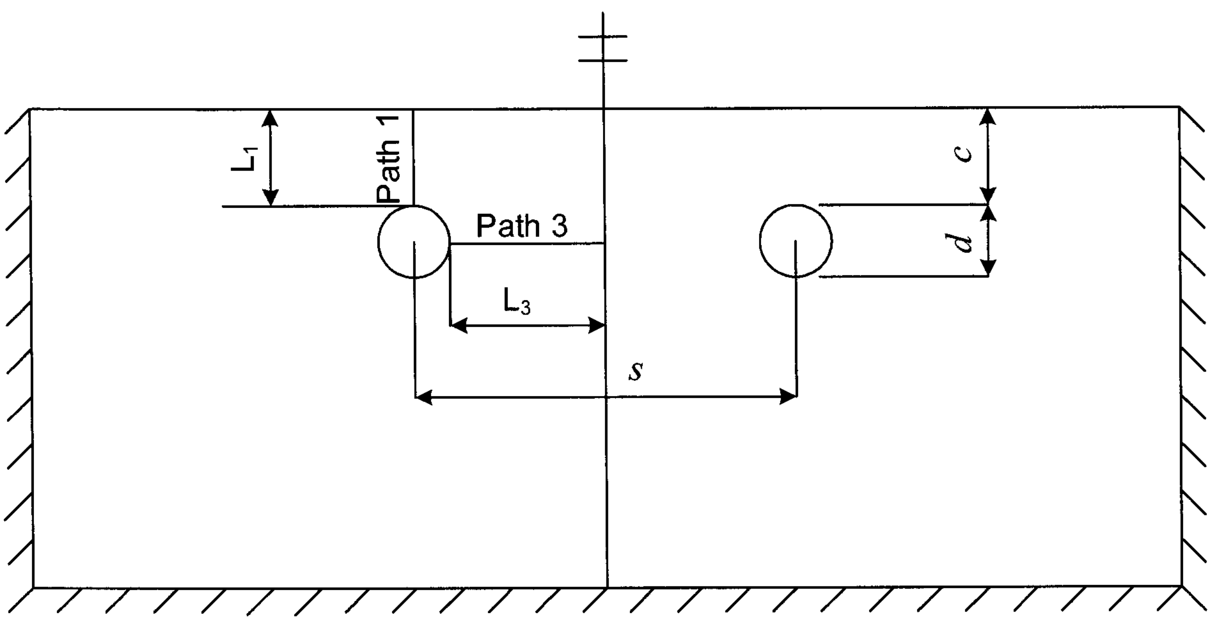

Figure 5.1: Lengths of path 1, L_1, and path 3, L_3

The lengths of paths 1 and 3, L_1 and L_3, can be expressed as a function of c, d, and s as follows:

$$L_1 = c \tag{5.1}$$

$$L_3 = (s - d)/2 \tag{5.2}$$

To set the limiting criterion of s between these two failure modes (i.e., longitudinal cracking or delamination), Eqs. 5.1 and 5.2 are equated to relate c, d, and s, i.e.,

$$L_1 \leq L_3 \quad \Rightarrow \quad c \leq (s-d)/2 \quad \text{or} \quad s \geq 2c+d \tag{5.3}$$

For rebar spacing s greater than or equal to $2c+d$, longitudinal cracking occurred before delamination. On the other hand, for rebar spacing s lower than $2c+d$, delamination occurred before longitudinal cracking. A similar limiting criterion can be obtained from the analytical models by equating the expressions of the pressure required to cause longitudinal cracking and delamination, respectively, i.e., by setting Eq. 3.20 equal to Eq. 3.26:

$$\frac{c/d+0.5}{1.665} \leq \frac{s}{d}-1 \quad \Rightarrow \quad s \geq 0.6c+1.3d \tag{5.4}$$

Figure 5.2 illustrates both limiting criteria (i.e., Eq. 5.3 and Eq. 5.4) as a function of c/d and s/d. Although both models identify the same trend, the analytical model clearly provides a more conservative approach. Note that the models derived from the analytical formulation were based on the assumption that concrete behaves linearly elastic and failed to account for the residual tensile strength that concrete exhibits once a crack has initiated.

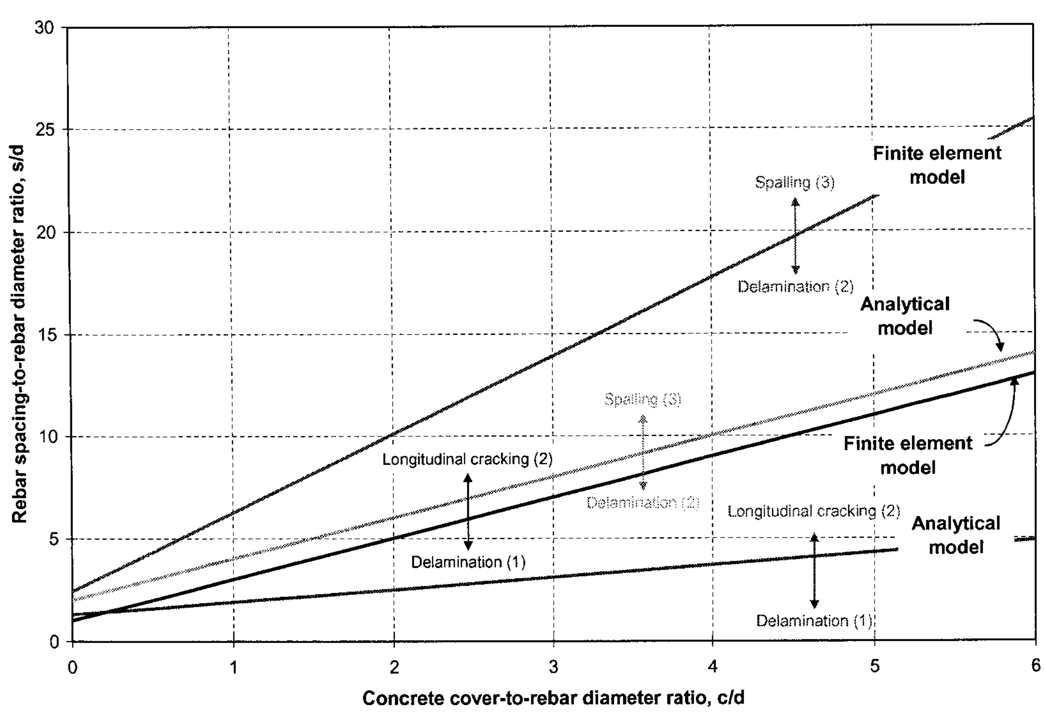

Figure 5.2: Limiting criteria between governing corrosion-induced failure modes of the bridge deck concrete cover as given by the analytical and finite element models

In general, spalling of the concrete cover occurred after delamination had taken place. However, if the spacing between reinforcing bars reached a large value, spalling would occur before delamination. The limiting criterion for s that differentiates between spalling or delamination as the governing failure mode is also determined by the lengths of paths 2 and 3, L_2 and L'_3, in Figure 5.3.

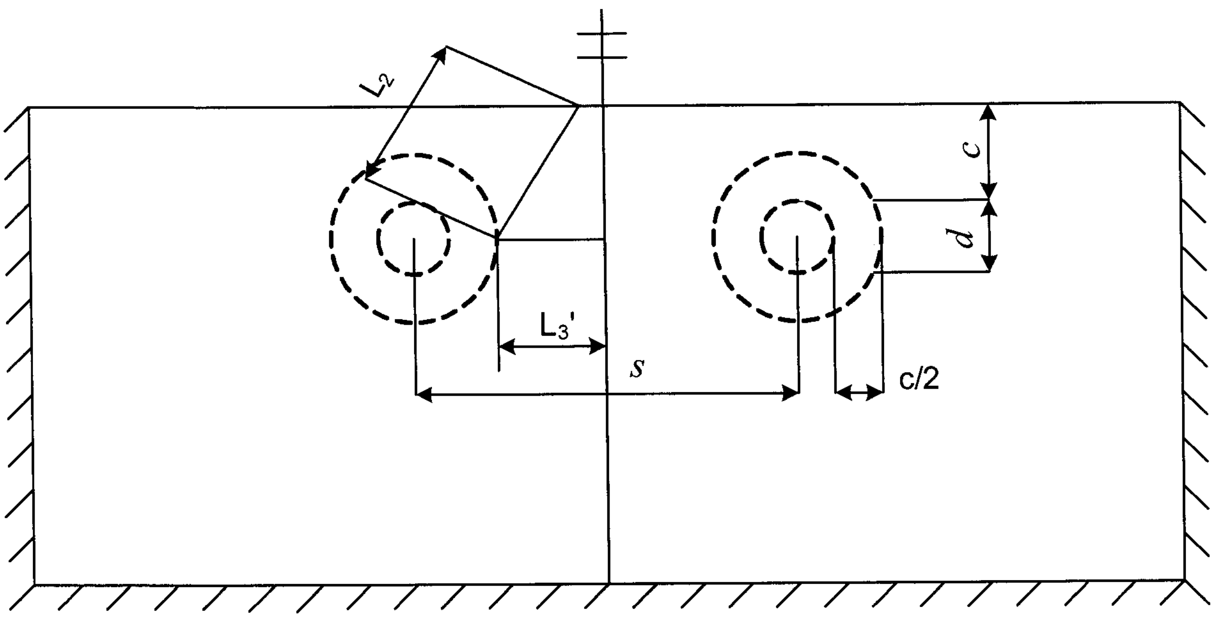

Figure 5.3: Lengths of path 2, L_2, and path 3, L'_3

The values of L_2 and L'_3 are determined from:

$$L_2 = \sqrt{2}\left(c + d/2\right) \tag{5.5}$$

$$L_3' = \left[s - \left(c + d\right)\right]/2 \tag{5.6}$$

Spalling of the concrete cover occurs when length L_2 is smaller than L'_3 (cracks will propagate along the shortest distance.) To set the limiting criterion between these two failure modes, Eqs. 5.5 and 5.6 are equated as follows:

$$L_2 \leq L_3' \quad \Rightarrow \quad c \leq 0.261s - 0.631d \quad \text{or} \quad s \geq 3.828c + 2.414d \tag{5.7}$$

For spacing between reinforcing bars s greater or equal to $3.828c + 2.414d$, spalling occurred before delamination. On the contrary, for rebar spacing s lower than $3.828c + 2.414d$, delamination occurred before spalling. So the governing failure mechanism here is delamination. A similar limiting criterion was derived from the analytical models presented in Chapter 3 (refer to Eq. 3.29). Comparison between the two limiting criteria (Eq. 3.29 and Eq. 5.7) is also presented in Figure 5.2. The analytical model once again gives a much more conservative estimate compared to the finite element model. Figure 5.2 also illustrates the regions in which each failure mechanism governs: (1) delamination followed by longitudinal cracking; (2) longitudinal cracking followed by delamination; and, (3) longitudinal cracking followed by spalling of the cover.

5.3 Parametric analysis

A parametric study was conducted to investigate the influence of the uniaxial compressive strength of concrete f'_c, the ratio of the clear cover of the rc bridge deck to the diameter of the rebar c/d, and the spacing between reinforcing bars s on the amount of corrosion build-up to cause cracking initiation, longitudinal cracking, spalling and delamination of the concrete deck cover. Table 5.3 shows the range of values used in the parametric analysis for each variable.

Table 5.3: Range of values used in parametric analysis

f'_c (MPa)	c (mm)	d (mm)	s (mm)
20, 25, 30			

5.3.1 Influence of f'_c

The effect of the uniaxial compressive strength of concrete f'_c on the values of corrosion build-up necessary to cause damage as described previously was studied by using the finite element model presented in Chapter 3 with f'_c taking values of 20 MPa, 25 MPa, and 30 MPa. The results of the numerical analyses are plotted in Figure 5.4 and tabulated in Table 5.4, where $\Delta d_1/2$ is the level of corrosion build-up to cause cracking initiation, $\Delta d_2/2$ is the level of corrosion build-up to cause longitudinal cracking, $\Delta d_3/2$ is the level of corrosion build-up to cause spalling, and $\Delta d_4/2$ is the level of corrosion build-up to cause delamination.

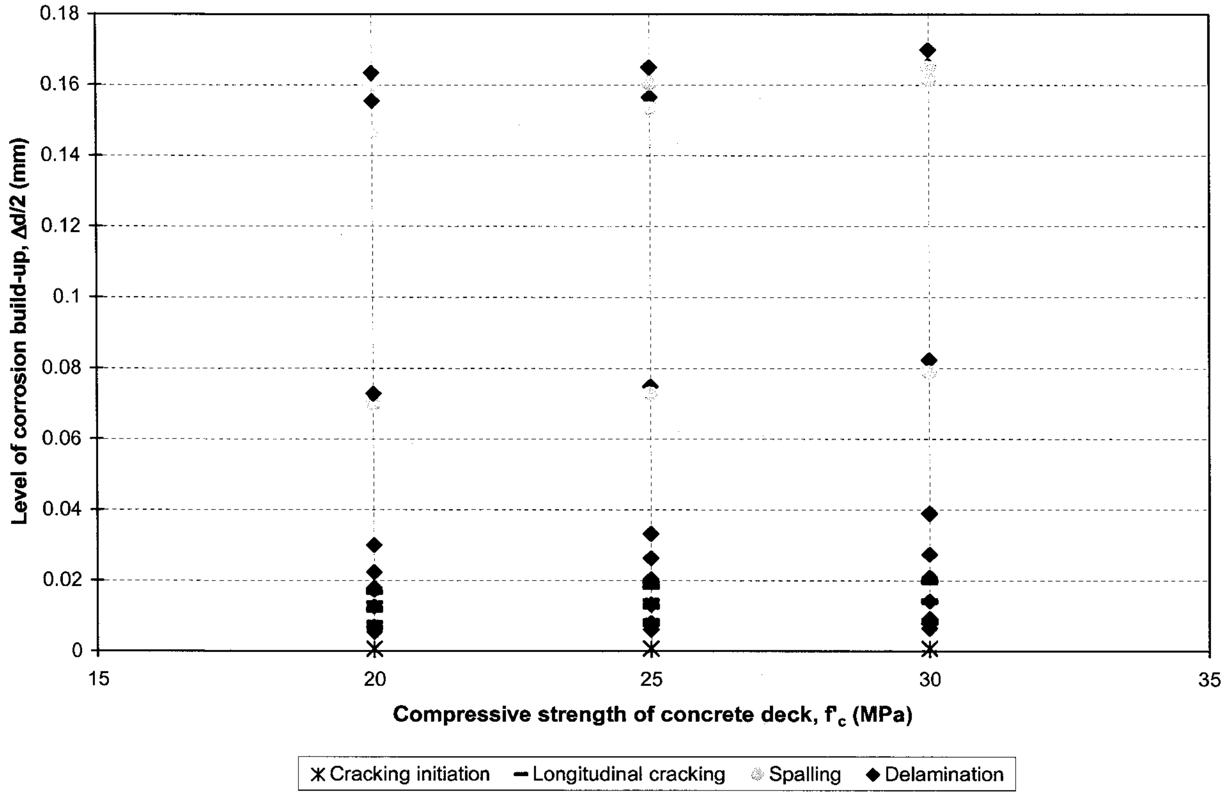

Figure 5.4: Effect of concrete cover f'_c on corrosion-induced damage mechanism

Table 5.4: Values of corrosion build-up causing different failure modes for concrete bridge decks with different f'_c

c (mm)	d (mm)	s (mm)	f'_c (MPa)	$\Delta d_1/2$ (mm)	$\Delta d_2/2$ (mm)	$\Delta d_3/2$ (mm)	$\Delta d_4/2$ (mm)
35	16	80	30	0.0008	0.0090	---	0.0067
35	16	80	25	0.0008	0.0089	---	0.0062
35	16	80	20	0.0007	0.0082	---	0.0056
35	16	86	30	0.0008	0.0089	---	0.0093
35	16	86	25	0.0008	0.0079	---	0.0081
35	16	86	20	0.0007	0.0067	---	0.0071
35	16	115	30	0.0010	0.0085	---	0.0390
35	16	115	25	0.0010	0.0075	---	0.0205
35	16	115	20	0.0009	0.0070	---	0.0175
35	16	173	30	0.0010	0.0080	0.0790	0.0825
35	16	173	25	0.0010	0.0075	0.0730	0.0750
35	16	173	20	0.0009	0.0065	0.0700	0.0730
50	16	80	30	0.0008	0.0145	---	0.0066
50	16	80	25	0.0008	0.0145	---	0.0063
50	16	80	20	0.0007	0.0138	---	0.0056
50	16	116	30	0.0008	0.0143	---	0.0143
50	16	116	25	0.0008	0.0133	---	0.0134
50	16	116	20	0.0007	0.0122	---	0.0128
50	16	140	30	0.0008	0.0139	---	0.0275
50	16	140	25	0.0008	0.0129	---	0.0264
50	16	140	20	0.0007	0.0122	---	0.0225
50	16	230	30	0.0010	0.0145	0.1615	0.1655
50	16	230	25	0.0010	0.0125	0.1535	0.1565
50	16	230	20	0.0009	0.0115	0.1465	0.1555
65	16	80	30	0.0008	0.0196	---	0.0066
65	16	80	25	0.0008	0.0186	---	0.0063
65	16	80	20	0.0007	0.0168	---	0.0056
65	16	146	30	0.0008	0.0201	---	0.0210
65	16	146	25	0.0008	0.0194	---	0.0202
65	16	146	20	0.0007	0.0174	---	0.0181
65	16	170	30	0.0008	0.0197	---	0.0392
65	16	170	25	0.0008	0.0196	---	0.0333
65	16	170	20	0.0007	0.0171	---	0.0302
65	16	287	30	0.0010	0.0195	0.1650	0.1700
65	16	287	25	0.0010	0.0180	0.1605	0.1650
65	16	287	20	0.0009	0.0165	0.1600	0.1635

From the results, it was found that with the increase of f'_c, the values of the level of corrosion build-up to cause the different failure modes also increased slightly (see Figure 5.4) However, the limiting criteria to determine the different failure mechanisms only depended on the values of

c, d, and s (as set by Eqs. 5.3 and 5.7) and were independent of the strength of the bridge deck cover.

5.3.2 Influence of c/d and s

The influence of the ratio of the clear cover of the rc bridge deck to the diameter of the rebar c/d on the values of corrosion build-up to cause cracking initiation, longitudinal cracking, delamination and spalling of the bridge deck was studied by analyzing the data presented in Table 5.1 and Table 5.2.

It was found that the value of the level of corrosion build-up causing cracking initiation, $\Delta d_1/2$, was not affected by changing the ratio c/d; however, it was affected by the diameter of the rebar d, $\Delta d_1/2$ increasing with the increase of d (see Figure 5.5). Parameter $\Delta d_1/2$ indicated the corrosion build-up necessary to initiate cracking right at the interface between the reinforcing steel and concrete, which was more dependent on the tensile strength of the surrounding concrete than on the thickness of the concrete cover itself.

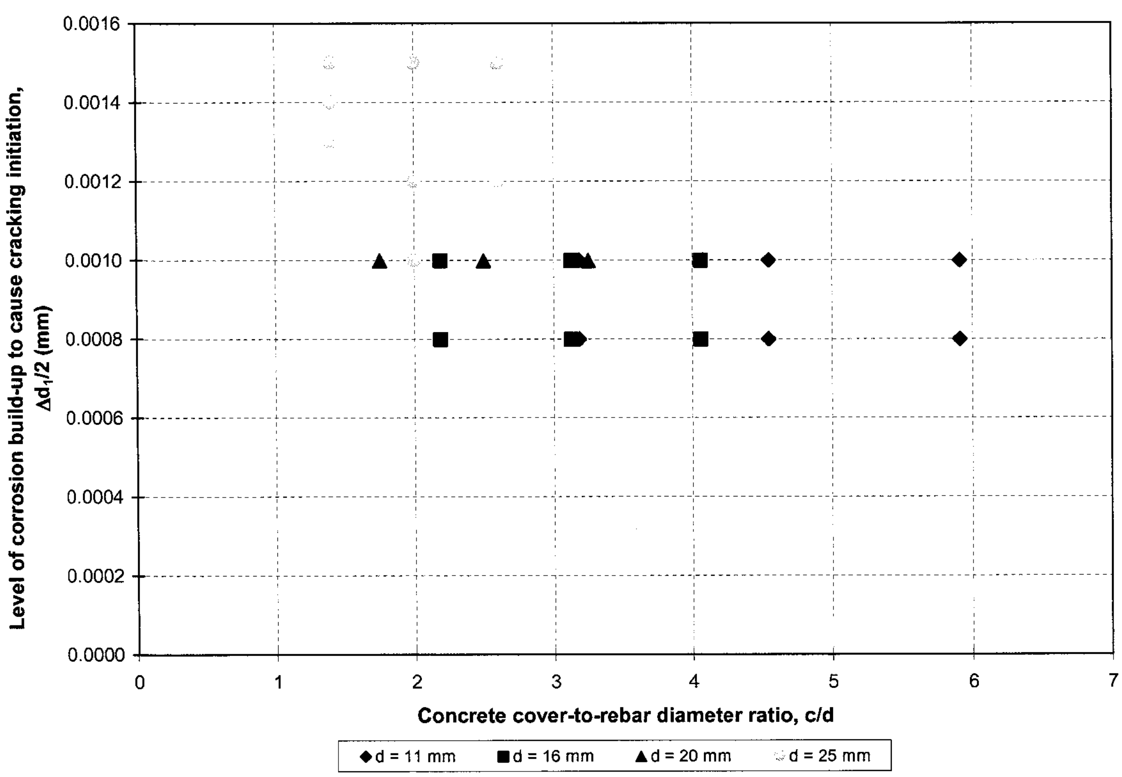

Figure 5.5: Influence of *c/d* on the level of corrosion build-up causing cracking initiation for different rebar diameters *d*

As previously described, the corrosion-induced failure mechanisms simulated by the finite element model were very sensitive to the lengths of the paths through which cracks developed. Therefore, the values of the level of corrosion build-up causing longitudinal cracking, $\Delta d_2/2$, are expected to be affected by the length of path 1 in Figure 5.1, i.e., $L_1 = c$. From the results, it was found that $\Delta d_2/2$ increased as c/d increased (see Figure 5.6). If c/d was unchanged, a higher value of d would lead to higher values of $\Delta d_2/2$. This is due to the fact that when d increases and c/d remains unchanged, the value of c increases, i.e., the length of path 1 in Figure 5.1 also increases, resulting in an increasing value of $\Delta d_2/2$.

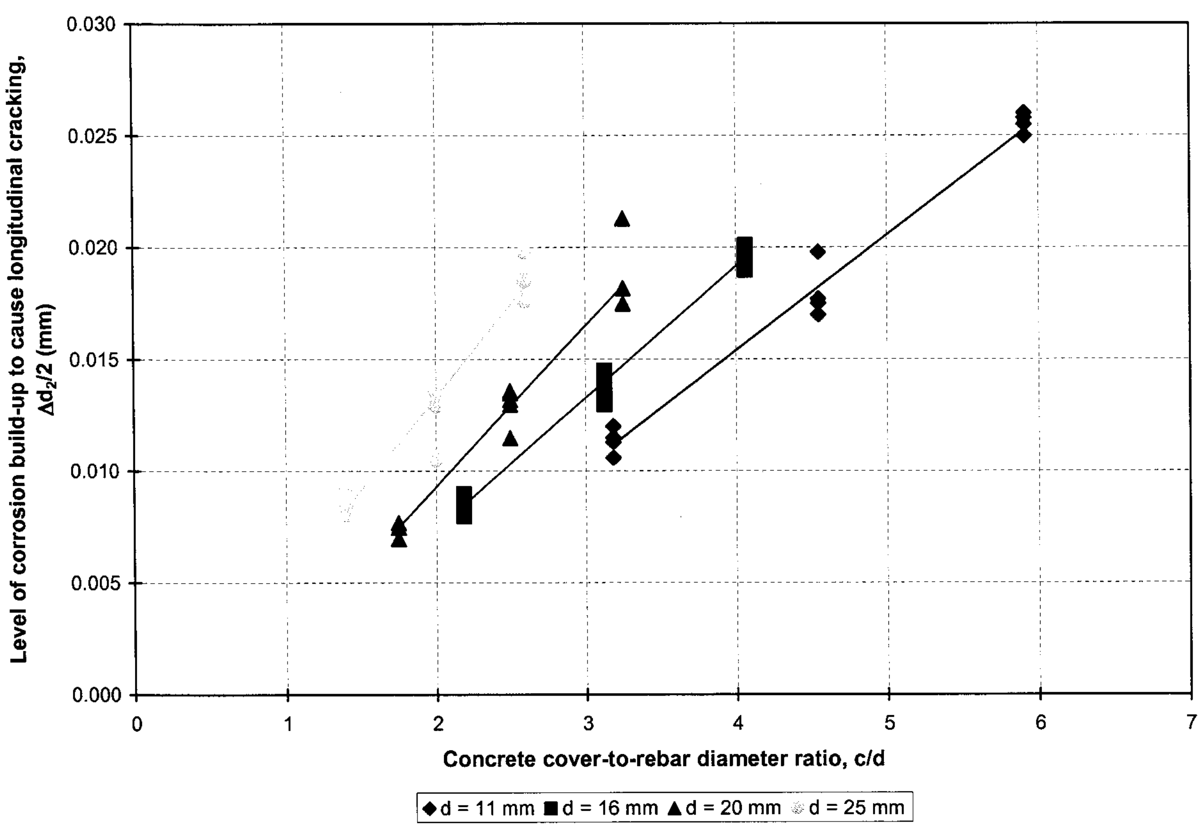

Figure 5.6: Influence of *c/d* on the level of corrosion build-up causing longitudinal cracking for different rebar diameters *d*

The values of corrosion build-up causing delamination, $\Delta d_4/2$, are affected by the length of path 3 in Figure 5.1, i.e., $L_3 = (s-d)/2$. This length is not only affected by the value of the rebar diameter d but also by the value of rebar spacing s. From the finite element analyses, it was found that $\Delta d_4/2$ decreased as d increased when s was fixed (see Figure 5.7 for s = 80 mm), since the length of path 3 decreased too. However, when d and s remained unchanged, the value of c/d had little influence on $\Delta d_4/2$, as illustrated in Figure 5.7. As it can be observed in the figure, the ratio of concrete cover-to-rebar diameter c/d has no impact on the onset of delamination of the bridge deck cover.

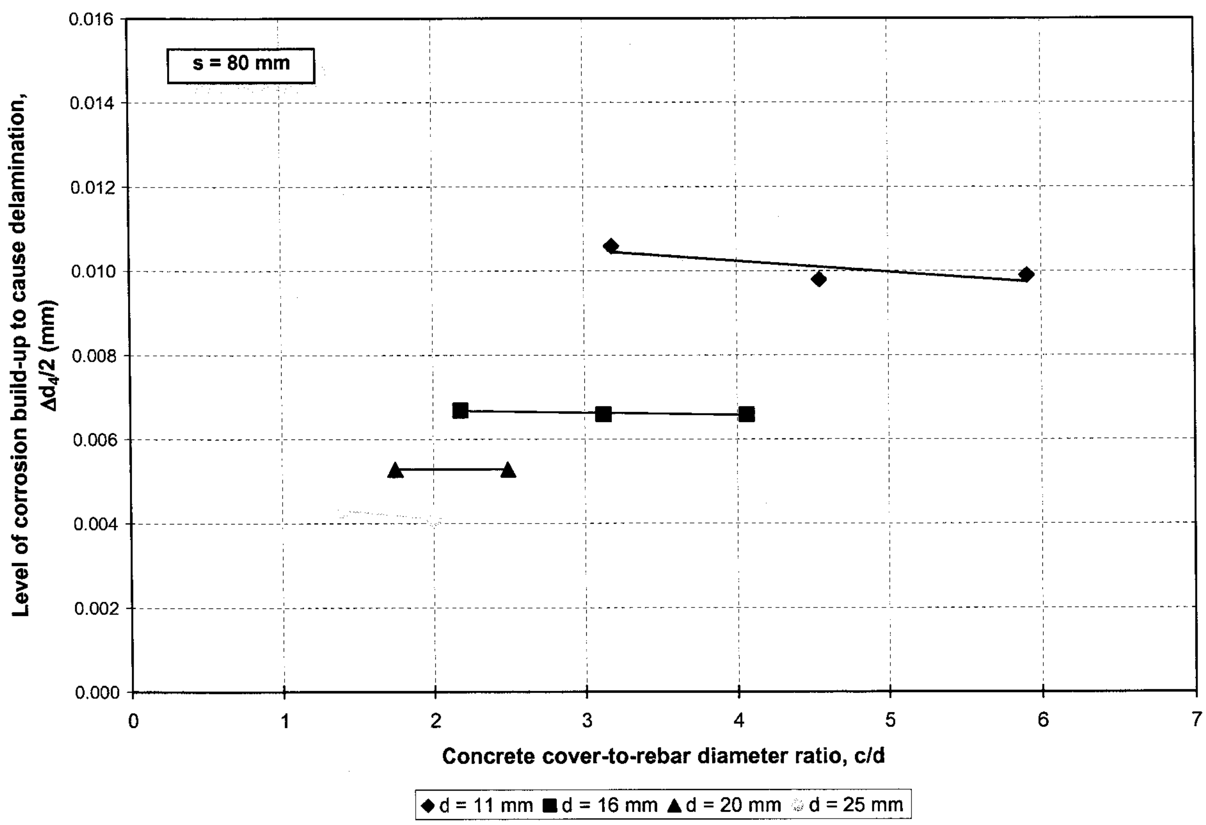

Figure 5.7: Influence of *c/d* on the level of corrosion build-up causing delamination for different rebar diameters *d* and rebar spacing *s* = 80 mm

It was also found that $\Delta d_4/2$ increased as s increased when c and d remained unchanged, since $L_3 = (s-d)/2$ increased too. The influence of s on $\Delta d_4/2$ is illustrated in Figure 5.8 for rebar diameters and concrete covers in the range of 11 to 25 mm and 35 to 65 mm, respectively. It is evident from the figure that the main parameter influencing delamination of the concrete cover is the spacing between reinforcing bars s. The same set of data is plotted in Figure 5.9 against the rebar spacing-to-rebar diameter ratio, s/d. Note that the date plotted in Figure 5.9 will be limited to Eq. (5.7), i.e., for s/d values greater or equal to $3.828c/d + 2.414$, delamination will no longer govern, and spalling will be come the governing failure mechanism.

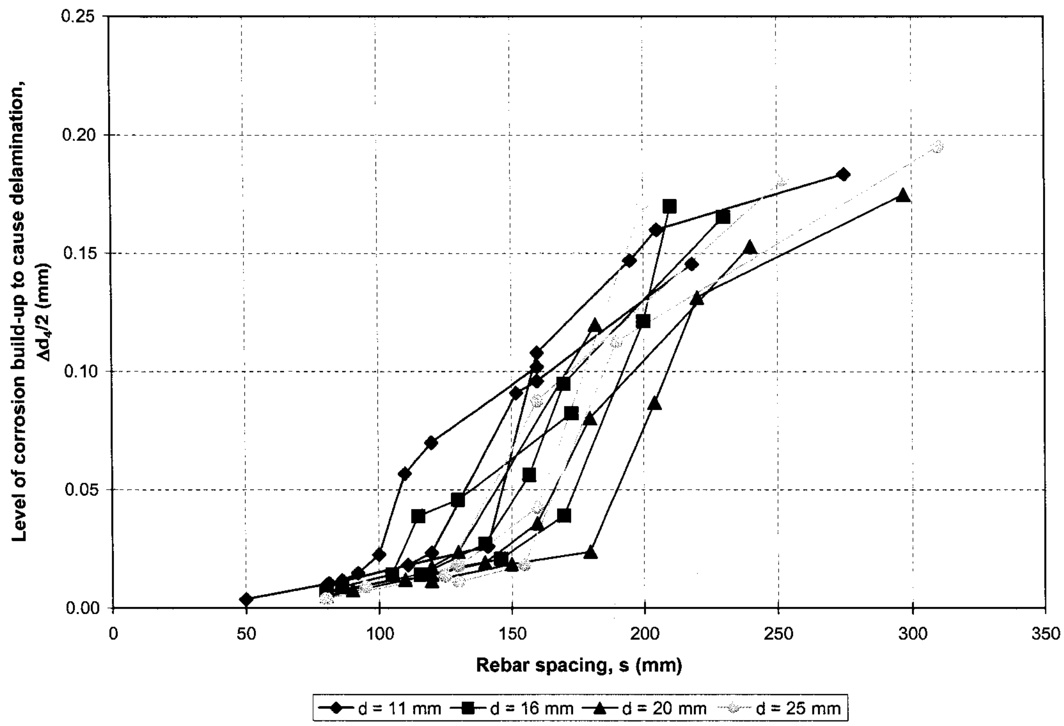

Figure 5.8: Influence of rebar spacing *s* on the level of corrosion build-up causing delamination for different rebar diameters

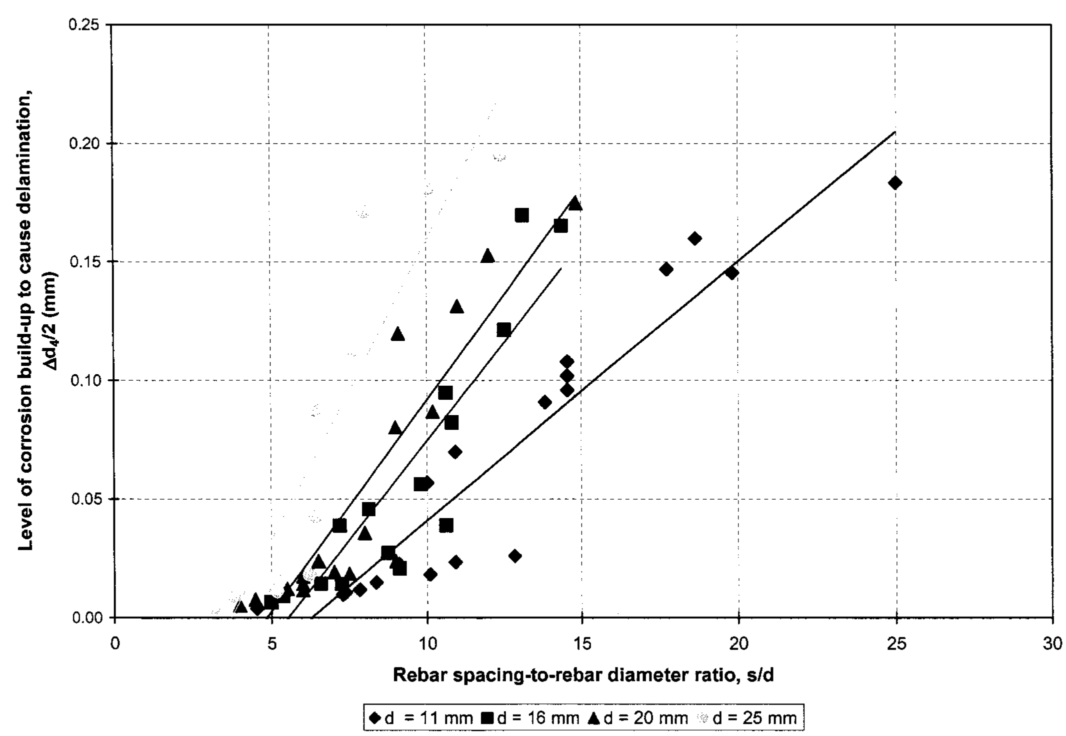

Figure 5.9: Influence of *s*/*d* on the level of corrosion build-up causing delamination for different rebar diameters

The values of corrosion build-up causing spalling $\Delta d_3/2$ depend on the length of path 2 in Figure 5.3, i.e., $L_2 = \sqrt{2}\left(c + d/2\right)$. Therefore, spalling of the concrete cover is influenced by the values taken by c and d. The analyses revealed that $\Delta d_3/2$ increased as c/d increased. If the concrete cover-to-rebar diameter ratio c/d was fixed, a higher value of d led to a higher value of $\Delta d_3/2$. This was due to the fact that when d increases and c/d remains constant, $L_2 = \sqrt{2}\left(c + d/2\right)$ increases, resulting in an increasing value for $\Delta d_3/2$. The influence of c/d on $\Delta d_3/2$ is shown in Figure 5.10.

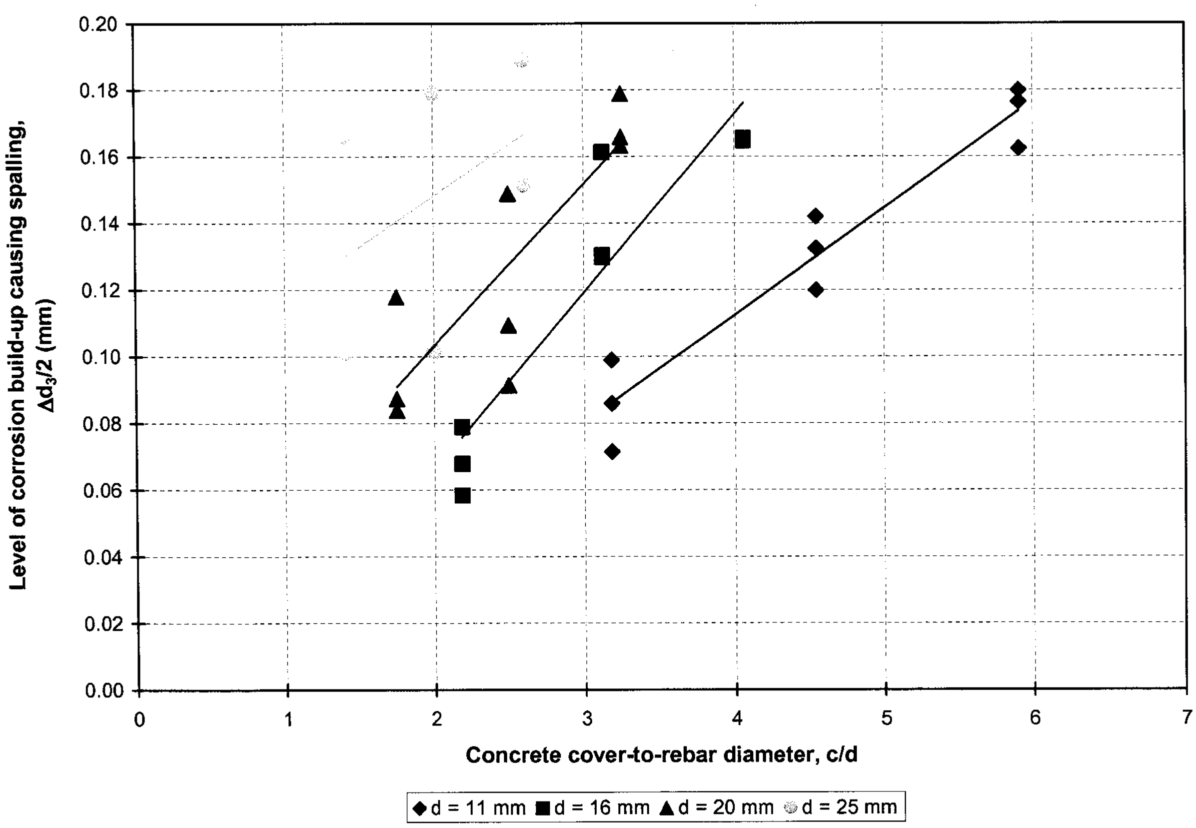

Figure 5.10: Influence of *c/d* on the level of corrosion build-up causing spalling for different rebar diameters

Chapter 6

Modeling rehabilitated rc bridge decks

6.1 Introduction

In this chapter, the effect of rehabilitating an rc bridge deck with an overlay on the corrosion-induced damage of the concrete cover is studied through the use of the finite element model presented in Chapter 4.

6.2 Numerical results

In the analyses, it was assumed that after corrosion-induced damage occurred, the damaged cover of the rc bridge deck was cleared and overlaid with new material. The finite element model presented in Chapter 4 was used to simulate the failure patterns of this rehabilitated rc bridge deck under the action of increasing levels of corrosion build-up around the reinforcing bars. The geometry configuration of the finite element model is shown in Figure , where t denotes the overlay thickness ($t = c + d/2$).

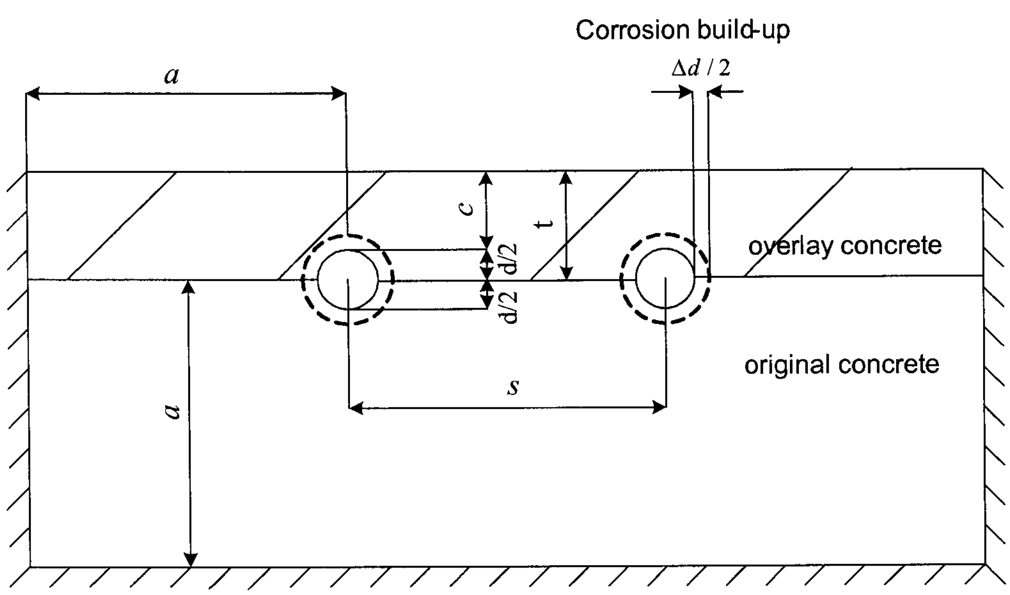

Figure 6.1: Geometry configuration of the rehabilitated rc bridge deck

Two types of overlay were used in the analyses: micro-silica concrete (MSC) overlay and latex-modified concrete (LMC) overlay. Properties for these overlays are tabulated in Table (ACI Committee 546 1996; ACI Committee 548 1994).

Table 6.1: Properties of overlays

Type of overlay	Thickness, t (mm)	f'_c (MPa)	E_c (MPa)
MSC	30–76	52–90	2.8×10^4
LMC	30–76	40	1.7×10^4

Due to the lack of stress-strain relationships for MSC and LMC, it was assumed in the finite element analysis that the overlay materials behave as linear elastic under uniaxial compression until the compressive stress reached 75% of f'_c and that the ultimate plastic strain is 0.0001. It was found from the analysis that the results were not sensitive to these values, because the maximum principal compressive stress obtained at the last time step was approximately 40% to 60% of f'_c. In most cases, the maximum biaxial stresses of the finite elements could not reach the compression yield surface. The uniaxial tensile strength f'_t of MSC and LMC is difficult to assess. For this study, the value was taken as that reported for high-performance concrete (ACI Committee 363 1992):

$$f_t' = 0.59\sqrt{f_c'} \quad \text{(MPa)} \tag{6.1}$$

The fracture energy G_f was taken as that given by Eq. 4.5.

The numerical results of the analyses are tabulated in Table through Table 6.3, where $\Delta d_1/2$ is the level of corrosion build-up causing cracking initiation, $\Delta d_2/2$ is the level of corrosion build-up causing longitudinal cracking, and $\Delta d_4/2$ is the level of corrosion build-up causing delamination of the deck cover.

Table 6.2: Values of corrosion build-up causing different failure modes for an rc bridge deck overlaid with MSC of f'_c = 52 MPa (t = 30–76 mm, d = 16 mm)

c (mm)	d (mm)	s (mm)	$\Delta d_1/2$ (mm)	$\Delta d_2/2$ (mm)	$\Delta d_4/2$ (mm)
22	16	86	0.002500	0.023500	0.008500
22	16	100	0.002500	0.012500	0.015500
22	16	120	0.002500	0.013500	0.021500
22	16	170	0.002500	0.012000	0.088000
68	16	150	0.003000	0.063500	0.020000
68	16	170	0.003000	0.079000	0.025000
68	16	290	0.003000	0.072500	0.071000
68	16	310	0.003000	0.074500	0.083500

Table 6.3: Values of corrosion build-up causing different failure modes for an rc bridge deck overlaid with MSC of f'_c = 90 MPa (t = 30–76 mm, d = 16 mm)

c (mm)	d (mm)	s (mm)	$\Delta d_1/2$ (mm)	$\Delta d_2/2$ (mm)	$\Delta d_4/2$ (mm)
22	16	86	0.004000	0.027000	0.012500
22	16	100	0.004000	0.019000	0.019000
22	16	120	0.004000	0.017000	0.033500
22	16	170	0.004000	0.016000	0.153000
68	16	150	0.004000	0.065000	0.028000
68	16	170	0.004000	0.086500	0.039000
68	16	290	0.004000	0.114500	0.118500
68	16	310	0.004000	0.119500	0.156000

Table 6.4: Values of corrosion build-up causing different failure modes for an rc bridge deck overlaid with LMC of f'_c = 40 MPa (t = 30–76 mm, d = 16 mm)

c (mm)	d (mm)	s (mm)	$\Delta d_1/2$ (mm)	$\Delta d_2/2$ (mm)	$\Delta d_4/2$ (mm)
22	16	86	0.004000	0.035500	0.008000
22	16	100	0.004000	0.030000	0.012000
22	16	120	0.004000	0.019500	0.019500
22	16	170	0.004000	0.017500	0.076500
68	16	150	0.004000	0.065000	0.019500
68	16	170	0.004000	0.076500	0.043500
68	16	290	0.004000	0.121500	0.066500
68	16	310	0.004000	0.093000	0.089000

Table 6.5: Values of corrosion build-up causing different failure modes for an rc bridge deck overlaid with MSC of f'_c = 52 MPa (t = 32–78 mm, d = 20 mm)

c (mm)	d (mm)	s (mm)	$\Delta d_1/2$ (mm)	$\Delta d_2/2$ (mm)	$\Delta d_4/2$ (mm)
22	20	86	0.003000	0.016000	0.007500
22	20	100	0.003000	0.012000	0.010000
22	20	120	0.003000	0.010500	0.019500
22	20	170	0.003000	0.009500	0.082000
68	20	150	0.003000	0.051500	0.018000
68	20	170	0.003000	0.063500	0.021000
68	20	290	0.003000	0.061000	0.063000
68	20	310	0.003000	0.061000	0.073500

Table 6.6: Values of corrosion build-up causing different failure modes for an rc bridge deck overlaid with MSC of f'_c = 90 MPa (t = 32–78 mm, d = 20 mm)

c (mm)	d (mm)	s (mm)	$\Delta d_1/2$ (mm)	$\Delta d_2/2$ (mm)	$\Delta d_4/2$ (mm)
22	20	86	0.004000	0.028000	0.007000
22	20	100	0.004000	0.022000	0.010500
22	20	120	0.004000	0.015000	0.016500
22	20	170	0.004000	0.013500	0.060500
68	20	150	0.004500	0.062500	0.016500
68	20	170	0.004500	0.068000	0.020000
68	20	290	0.004500	0.109500	0.059000
68	20	310	0.004500	0.081500	0.086000

Table 6.7: Values of corrosion build-up causing different failure modes for an rc bridge deck overlaid with LMC of f'_c = 40 MPa (t = 32–78 mm, d = 20 mm)

c (mm)	d (mm)	s (mm)	$\Delta d_1/2$ (mm)	$\Delta d_2/2$ (mm)	$\Delta d_4/2$ (mm)
22	20	86	0.004500	0.019500	0.010000
22	20	100	0.004500	0.015500	0.015500
22	20	120	0.004500	0.013500	0.029500
22	20	170	0.004500	0.012500	0.116000
68	20	150	0.004500	0.051500	0.017000
68	20	170	0.004500	0.094000	0.030000
68	20	290	0.004500	0.087500	0.092500
68	20	310	0.004500	0.082500	0.135500

From the analyses, it was found that after the onset of cracking, cracks propagate along two main directions: the vertical and horizontal directions, which respectively correspond to paths 1 and 3 in Figure . Longitudinal cracking occurred when cracks developed along path 1 and reached the surface of the deck. Delamination occurred when two cracks that initiated from neighbouring reinforcing bars developed along path 3 towards each other. Whereas path 1 is in the overlay, path 3 corresponds to the contact surface between the overlay and the substrate concrete.

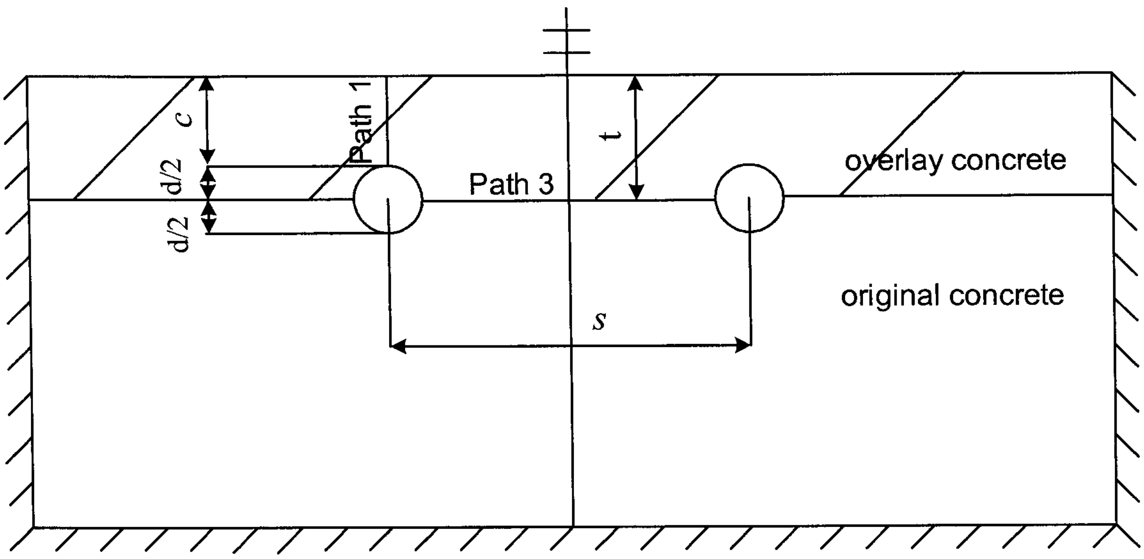

Figure 6.2: Paths 1 and 3 in overlaid rc bridge deck

Depending on the value of the spacing *s* between reinforcing bars, the failure mechanisms of overlaid rc bridge decks due to corrosion build-up can be classified as follows:

1. Delamination followed by longitudinal cracking
2. Longitudinal cracking followed by delamination

When the spacing between reinforcing bars is very small, failure of the overlaid rc bridge deck was governed by delamination followed by longitudinal cracking. With the increase of the spacing between reinforcing bars, failure was governed by longitudinal cracking followed by delamination. The limiting criterion between these two failure modes is similar to Eq. 5.3; however, it was observed that cracks propagated along path 3 at a much faster rate than along path 1. This is mainly due to the fact that the tensile strength of the overlay was higher than the original concrete, and that the contact interfaces between the two materials is a weak plane.

Chapter 7

Propagation models

7.1 Introduction

In this chapter, a comparison of the values of corrosion build-up causing cracking initiation, longitudinal cracking, spalling and delamination of rc bridge decks obtained by the analytical models presented in Chapter 3 and the finite element analyses presented in Chapter 5 and 6 is made. This comparison is presented in the form of simple models for prediction of corrosion-induced crack initiation, longitudinal cracking, spalling, and delamination of the concrete bridge deck cover. These models have been formulated by modifying the analytical models developed in Chapter 3 with correction factors. These factors were obtained by comparing the results from the analytical models for each of the corrosion-induced failure modes with those from the finite element analyses.

The time elapsed since corrosion initiation until one of the previously described failure modes is attained t_p is calculated from Eq. 3.10 by multiplying it by a factor α, i.e.,

$$t_p = \alpha \cdot \frac{\pi}{2}\left[\frac{1}{\rho_r} - \frac{0.523}{\rho_s}\right]^{-1} \cdot \frac{d\Delta d}{s j_r} \tag{7.1}$$

where ρ_r and ρ_s are respectively the densities of hydrated red rust and steel, d is the rebar diameter, s is the spacing between reinforcing bars, j_r is the rate of rust production per unit area, and Δd is the increase in rebar diameter due to accumulation of rust around the bar (this variable will take different values depending on the limit state considered, i.e., crack initiation, longitudinal cracking, spalling and/or delamination.) The values of α have been obtained by dividing the Δd obtained for each failure mechanism in the finite element analyses by that obtained using Eqs. 3.13, 3.21, 3.24, and 3.27, which respectively correspond to the increase in rebar diameter causing cracking initiation, longitudinal cracking, spalling, and delamination. These values of α are presented in the following sections for each of the corrosion-induced failure modes.

7.2 Cracking initiation

The model for initiation of cracking at the surface of the reinforcing bar is formulated from Eq. 3.13 by multiplying it by a correction factor α_1. The proposed model is as follows:

$$\Delta d_1 = \alpha_1 \cdot \frac{1}{2} \frac{(1+\nu)}{E_c} \frac{f_t'}{(c/d)^2 + (c/d) + 0.5} \left[d(1-\nu) + 2c(c/d+1) \right] \tag{7.2}$$

The values of α_1 have been obtained by dividing the Δd_1 resulting from the finite element analyses by that calculated from Eq. 3.13. Values of α_1 obtained for both unprotected and rehabilitated rc bridge decks are presented in the following.

7.2.1 Unprotected rc decks

Table 7.1 and Table 7.2 present correction factors α_1^{u} obtained by comparing the finite element results to those obtained from Eq. 3.13 for an unprotected rc bridge deck. Material properties for the concrete deck are those used in the finite element analyses (f'_c = 30 MPa, f'_t = 1.8 MPa, E_c = 25.7 GPa, ν = 0.2).

Table 7.1: Correction factors α_1^u for Δd_1 for an unprotected rc bridge deck with rebar diameters of 11 and 16 mm

c (mm)	d (mm)	s (mm)	Δd_1 (mm) (FEM)	Δd_1 (mm) (Eq. 3.13)	α_1^u Δd_1 (FEM) / Δd_1 (3.13)
35	11	50	0.0016	0.000920095	1.74
35	11	81	0.0016	0.000920095	1.74
35	11	86	0.0016	0.000920095	1.74
35	11	92	0.0016	0.000920095	1.74
35	11	100	0.0020	0.000920095	2.17
35	11	110	0.0020	0.000920095	2.17
35	11	120	0.0020	0.000920095	2.17
35	11	160	0.0020	0.000920095	2.17
50	11	80	0.0016	0.000923203	1.73
50	11	111	0.0016	0.000923203	1.73
50	11	120	0.0016	0.000923203	1.73
50	11	152	0.0020	0.000923203	2.17
50	11	160	0.0020	0.000923203	2.17
50	11	218	0.0020	0.000923203	2.17
65	11	80	0.0016	0.000924566	1.73
65	11	141	0.0016	0.000924566	1.73
65	11	160	0.0020	0.000924566	2.16
65	11	195	0.0020	0.000924566	2.16
65	11	205	0.0020	0.000924566	2.16
65	11	275	0.0020	0.000924566	2.16
35	16	80	0.0016	0.001330045	1.20
35	16	86	0.0016	0.001330045	1.20
35	16	105	0.0016	0.001330045	1.20
35	16	115	0.0020	0.001330045	1.50
35	16	130	0.0020	0.001330045	1.50
35	16	173	0.0020	0.001330045	1.50
50	16	80	0.0016	0.001338018	1.20
50	16	116	0.0016	0.001338018	1.20
50	16	140	0.0016	0.001338018	1.20
50	16	157	0.0020	0.001338018	1.49
50	16	170	0.0020	0.001338018	1.49
50	16	230	0.0020	0.001338018	1.49
65	16	80	0.0016	0.001341686	1.19
65	16	146	0.0016	0.001341686	1.19
65	16	170	0.0016	0.001341686	1.19
65	16	200	0.0020	0.001341686	1.49
65	16	210	0.0020	0.001341686	1.49

Table 7.2: Correction factors α_1^u for Δd_1 for an unprotected rc bridge deck with rebar diameters of 20 and 25 mm

c (mm)	d (mm)	s (mm)	Δd_1 (mm) (FEM)	Δd_1 (mm) (Eq. 3.13)	α_1^u Δd_1 (FEM) / Δd_1 (3.13)
35	20	80	0.0020	0.001653387	1.21
35	20	90	0.0020	0.001653387	1.21
35	20	110	0.0020	0.001653387	1.21
35	20	120	0.0020	0.001653387	1.21
35	20	130	0.0020	0.001653387	1.21
35	20	182	0.0020	0.001653387	1.21
50	20	80	0.0020	0.001666889	1.20
50	20	120	0.0020	0.001666889	1.20
50	20	140	0.0020	0.001666889	1.20
50	20	160	0.0020	0.001666889	1.20
50	20	180	0.0020	0.001666889	1.20
50	20	240	0.0020	0.001666889	1.20
65	20	120	0.0020	0.001673333	1.20
65	20	150	0.0020	0.001673333	1.20
65	20	180	0.0020	0.001673333	1.20
65	20	204	0.0020	0.001673333	1.20
65	20	220	0.0020	0.001673333	1.20
65	20	297	0.0020	0.001673333	1.20
35	25	80	0.0028	0.002051813	1.36
35	25	95	0.0026	0.002051813	1.27
35	25	130	0.0026	0.002051813	1.27
35	25	160	0.0030	0.002051813	1.46
35	25	200	0.0030	0.002051813	1.46
50	25	80	0.0024	0.002073977	1.16
50	25	125	0.0020	0.002073977	0.96
50	25	160	0.0030	0.002073977	1.45
50	25	252	0.0030	0.002073977	1.45
65	25	130	0.0024	0.00208502	1.15
65	25	155	0.0024	0.00208502	1.15
65	25	190	0.0030	0.00208502	1.44
65	25	310	0.0030	0.00208502	1.44

The results tabulated in Table 7.1 and Table 7.2 are plotted in Figure 7.1 as a function of the concrete cover-to-rebar diameter ratio c/d. The figure illustrates that Δd_1 obtained from the finite element model is up to two times larger to that obtained from the analytical model. The analytical model given by Eq. 3.13, which was formulated under the assumption of linear elastic behaviour, gives conservative values. However, the correction factor α_1^u tends to decrease as the rebar diameter increases (see Figure 7.2)

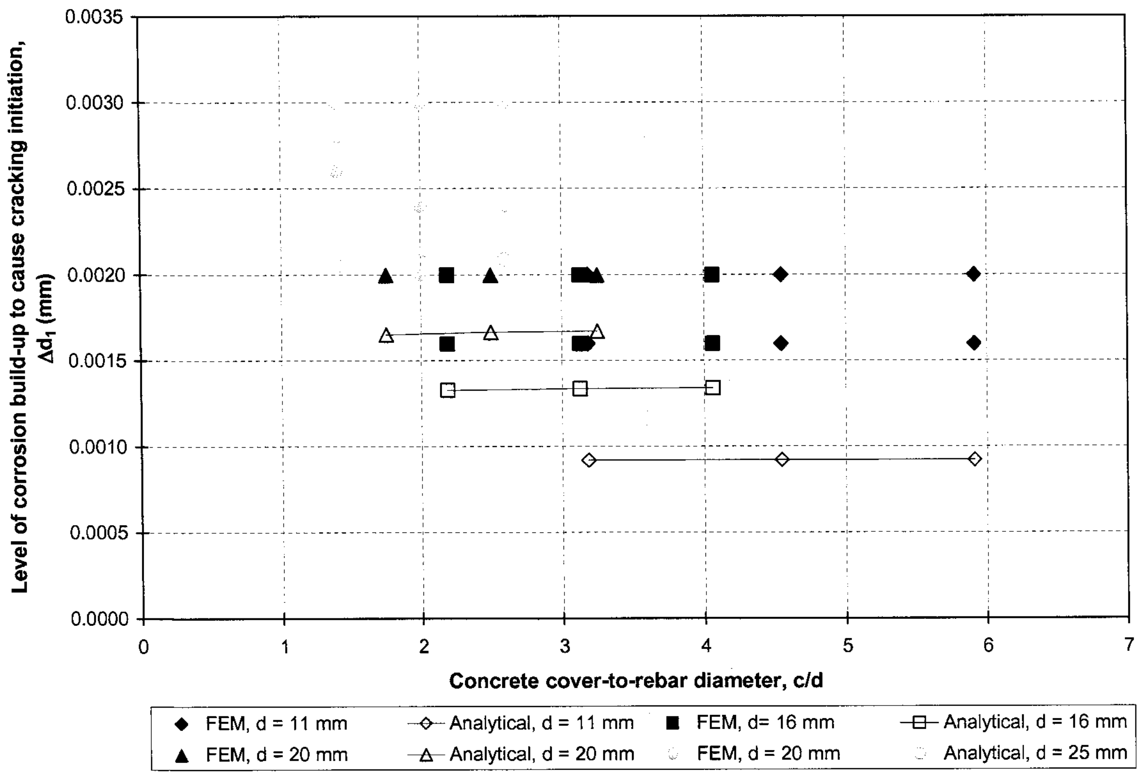

Figure 7.1: Comparison of the level of corrosion build-up to cause cracking initiation between the finite element and analytical models

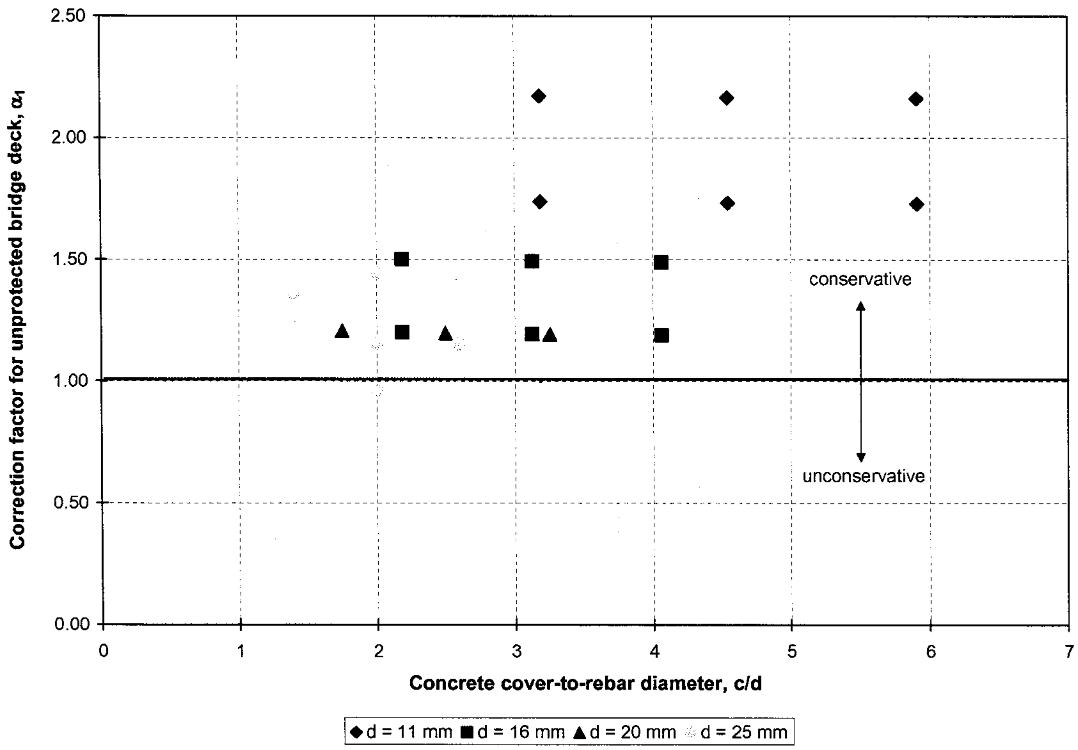

Figure 7.2: Correction factor α_1^u for an unprotected rc bridge deck

7.2.2 Rehabilitated rc decks

Table 7.3, Table 7.4, and Table 7.5 present correction factors α_1^r obtained by comparing the finite element results in Chapter 6 to those obtained from Eq. 3.13 for an overlaid rc bridge deck. Since Eq. 3.13 was formulated under the assumption that the concrete cover behaves as a thick-wall cylinder of uniform material, the analytical results reported in the tables were obtained by assuming that the thick-wall cylinder is made of the overlay material.

Table 7.3: Correction factors α_1^r for Δd_1 for an rc bridge deck overlaid with MSC (f'_c = 52 MPa, f'_t = 4.3 MPa, E_c = 33.8 GPa, ν = 0.2)

c (mm)	d (mm)	s (mm)	Δd_1 (mm) (FEM)	Δd_1 (mm) (Eq. 3.13)	α_1^r Δd_1 (FEM) / Δd_1 (3.13)
22	16	86	0.005	0.002346207	2.13
22	16	86	0.005	0.002346207	2.13
22	16	86	0.005	0.002346207	2.13
22	16	86	0.005	0.002346207	2.13
68	16	150	0.006	0.002399647	2.50
68	16	170	0.006	0.002399647	2.50
68	16	290	0.006	0.002399647	2.50
68	16	310	0.006	0.002399647	2.50
22	20	86	0.006	0.002906	2.07
22	20	100	0.006	0.002906	2.07
22	20	120	0.006	0.002906	2.07
22	20	170	0.006	0.002906	2.07
68	20	150	0.006	0.002993	2.00
68	20	170	0.006	0.002993	2.00
68	20	290	0.006	0.002993	2.00
68	20	310	0.006	0.002993	2.00

Table 7.4: Correction factors α_1^r for Δd_1 for an rc bridge deck overlaid with MSC (f'_c = 90 MPa, f'_t = 5.6 MPa, E_c = 44.6 GPa, ν = 0.2)

c (mm)	d (mm)	s (mm)	Δd_1 (mm) (FEM)	Δd_1 (mm) (Eq. 3.13)	α_1^r Δd_1 (FEM) / Δd_1 (3.13)
22	16	86	0.008	0.002346207	3.41
22	16	100	0.008	0.002346207	3.41
22	16	120	0.008	0.002346207	3.41
22	16	170	0.008	0.002346207	3.41
68	16	150	0.008	0.002399647	3.33
68	16	170	0.008	0.002399647	3.33
68	16	290	0.008	0.002399647	3.33
68	16	310	0.008	0.002399647	3.33
22	20	86	0.008	0.002906	2.75
22	20	100	0.008	0.002906	2.75
22	20	120	0.008	0.002906	2.75
22	20	170	0.008	0.002906	2.75
68	20	150	0.009	0.002993	3.01
68	20	170	0.009	0.002993	3.01
68	20	290	0.009	0.002993	3.01
68	20	310	0.009	0.002993	3.01

Table 7.5: Correction factors α_1^r for Δd_1 for an rc bridge deck overlaid with LMC (f'_c = 40 MPa, f'_t = 3.7 MPa, E_c = 29.7 GPa, ν = 0.2)

c (mm)	d (mm)	s (mm)	Δd_1 (mm) (FEM)	Δd_1 (mm) (Eq. 3.13)	α_1^r Δd_1 (FEM) / Δd_1 (3.13)
22	16	86	0.008	0.002346	3.41
22	16	100	0.008	0.002346	3.41
22	16	120	0.008	0.002346	3.41
22	16	170	0.008	0.002346	3.41
68	16	150	0.008	0.002400	3.33
68	16	170	0.008	0.002400	3.33
68	16	290	0.008	0.002400	3.33
68	16	310	0.008	0.002400	3.33
22	20	86	0.009	0.002906	3.10
22	20	100	0.009	0.002906	3.10
22	20	120	0.009	0.002906	3.10
22	20	170	0.009	0.002906	3.10
68	20	150	0.009	0.002993	3.01
68	20	170	0.009	0.002993	3.01
68	20	290	0.009	0.002993	3.01
68	20	310	0.009	0.002993	3.01

Similar to the unprotected rc bridge deck, it was found that Δd_1 calculated from the finite element analyses was greater than that calculated from the analytical model. The correction factors α_1^r for an overlaid bridge deck range between 2.0 and 3.4 as illustrated in Figure 7.3.

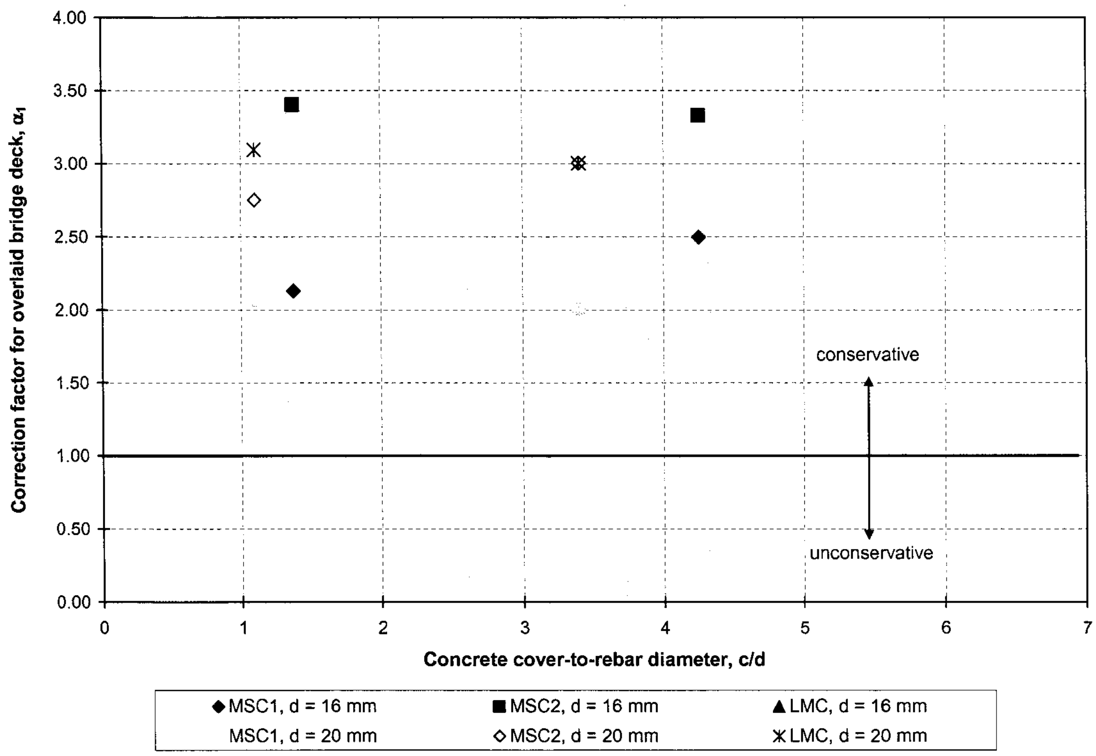

Figure 7.3: Correction factor α_1^r for an overlaid rc bridge deck (MSC1 denotes MSC overlay with f'_c = 52 MPa; MSC2 denotes MSC overlay with f'_c = 90 MPa)

7.3 Longitudinal cracking

The model for longitudinal cracking of the concrete cover is formulated from Eq. 3.21 by multiplying it by a correction factor α_2. The proposed model is as follows:

$$\Delta d_2 = \alpha_2 \cdot \frac{1}{3.33} \frac{(1+\nu)}{E_c} f_t' \frac{(c/d)+0.5}{(c/d)^2+(c/d)} \left[d(1-\nu)+2c(c/d+1) \right] \tag{7.3}$$

The values of α_2 have been obtained by dividing the Δd_2 resulting from the finite element analyses by that calculated from Eq. 3.21. Values of α_2 obtained for both unprotected and rehabilitated rc bridge decks are presented in the following.

7.3.1 Unprotected rc decks

Table 7.6 and Table 7.7 present correction factors α_2^{u} obtained by comparing the finite element results to those obtained from Eq. 3.21 for an unprotected rc bridge deck. Material properties for the concrete deck are those used in the finite element analyses (f'_c = 30 MPa, f'_t = 1.8 MPa, E_c = 25.7 GPa, ν = 0.2).

Table 7.6: Correction factors α_2^u for Δd_2 for an unprotected rc bridge deck with rebar diameters of 11 and 16 mm

c (mm)	d (mm)	s (mm)	Δd_2 (mm) (FEM)	Δd_2 (mm) (Eq. 3.21)	α_2^u Δd_2 (FEM) / Δd_2 (3.21)
35	11	50	0.0226	0.002111065	10.71
35	11	81	0.0212	0.002111065	10.04
35	11	86	0.0212	0.002111065	10.04
35	11	92	0.0230	0.002111065	10.89
35	11	100	0.0226	0.002111065	10.71
35	11	110	0.0240	0.002111065	11.37
35	11	120	0.0240	0.002111065	11.37
35	11	160	0.0230	0.002111065	10.89
50	11	80	0.0396	0.002853078	13.88
50	11	111	0.0354	0.002853078	12.41
50	11	120	0.0350	0.002853078	12.27
50	11	152	0.0350	0.002853078	12.27
50	11	160	0.0340	0.002853078	11.92
50	11	218	0.0340	0.002853078	11.92
65	11	80	0.0520	0.003602521	14.43
65	11	141	0.0516	0.003602521	14.32
65	11	160	0.0510	0.003602521	14.16
65	11	195	0.0500	0.003602521	13.88
65	11	205	0.0500	0.003602521	13.88
65	11	275	0.0510	0.003602521	14.16
35	16	80	0.0180	0.002300792	7.82
35	16	86	0.0178	0.002300792	7.74
35	16	105	0.0164	0.002300792	7.13
35	16	115	0.0170	0.002300792	7.39
35	16	130	0.0170	0.002300792	7.39
35	16	173	0.0160	0.002300792	6.95
50	16	80	0.0290	0.003026095	9.58
50	16	116	0.0286	0.003026095	9.45
50	16	140	0.0278	0.003026095	9.19
50	16	157	0.0260	0.003026095	8.59
50	16	170	0.0270	0.003026095	8.92
50	16	230	0.0290	0.003026095	9.58
65	16	80	0.0392	0.003765924	10.41
65	16	146	0.0402	0.003765924	10.67
65	16	170	0.0394	0.003765924	10.46
65	16	200	0.0380	0.003765924	10.09
65	16	210	0.0390	0.003765924	10.36

Table 7.7: Correction factors α_2^u for Δd_2 for an unprotected rc bridge deck with rebar diameters of 20 and 25 mm

c (mm)	d (mm)	s (mm)	Δd_2 (mm) (FEM)	Δd_2 (mm) (Eq. 3.21)	α_2^u Δd_2 (FEM) / Δd_2 (3.21)
35	20	80	0.0154	0.002466442	6.24
35	20	90	0.0150	0.002466442	6.08
35	20	110	0.0150	0.002466442	6.08
35	20	120	0.0150	0.002466442	6.08
35	20	130	0.0150	0.002466442	6.08
35	20	182	0.0140	0.002466442	5.68
50	20	80	0.0264	0.003175027	8.31
50	20	120	0.0272	0.003175027	8.57
50	20	140	0.0270	0.003175027	8.50
50	20	160	0.0260	0.003175027	8.19
50	20	180	0.0260	0.003175027	8.19
50	20	240	0.0230	0.003175027	7.24
65	20	120	0.0426	0.003905193	10.91
65	20	150	0.0364	0.003905193	9.32
65	20	180	0.0350	0.003905193	8.96
65	20	204	0.0350	0.003905193	8.96
65	20	220	0.0350	0.003905193	8.96
65	20	297	0.0350	0.003905193	8.96
35	25	80	0.0186	0.002689833	6.91
35	25	95	0.0172	0.002689833	6.39
35	25	130	0.0174	0.002689833	6.47
35	25	160	0.0160	0.002689833	5.95
35	25	200	0.0170	0.002689833	6.32
50	25	80	0.0258	0.003373586	7.65
50	25	125	0.0258	0.003373586	7.65
50	25	160	0.0270	0.003373586	8.00
50	25	252	0.0210	0.003373586	6.22
65	25	130	0.0396	0.004089392	9.68
65	25	155	0.0352	0.004089392	8.61
65	25	190	0.0370	0.004089392	9.05
65	25	310	0.0370	0.004089392	9.05

The results tabulated in Table 7.6 and Table 7.7 are plotted in Figure 7.4 as a function of the concrete cover-to-rebar diameter ratio c/d. The figure illustrates that Δd_2 obtained from the finite element model is up to fourteen times larger to that obtained from the analytical model for large values of c/d. As the concrete cover-to-rebar diameter ratio decreases to around 1.5, the difference is reduced to a factor of six (see Figure 7.5)

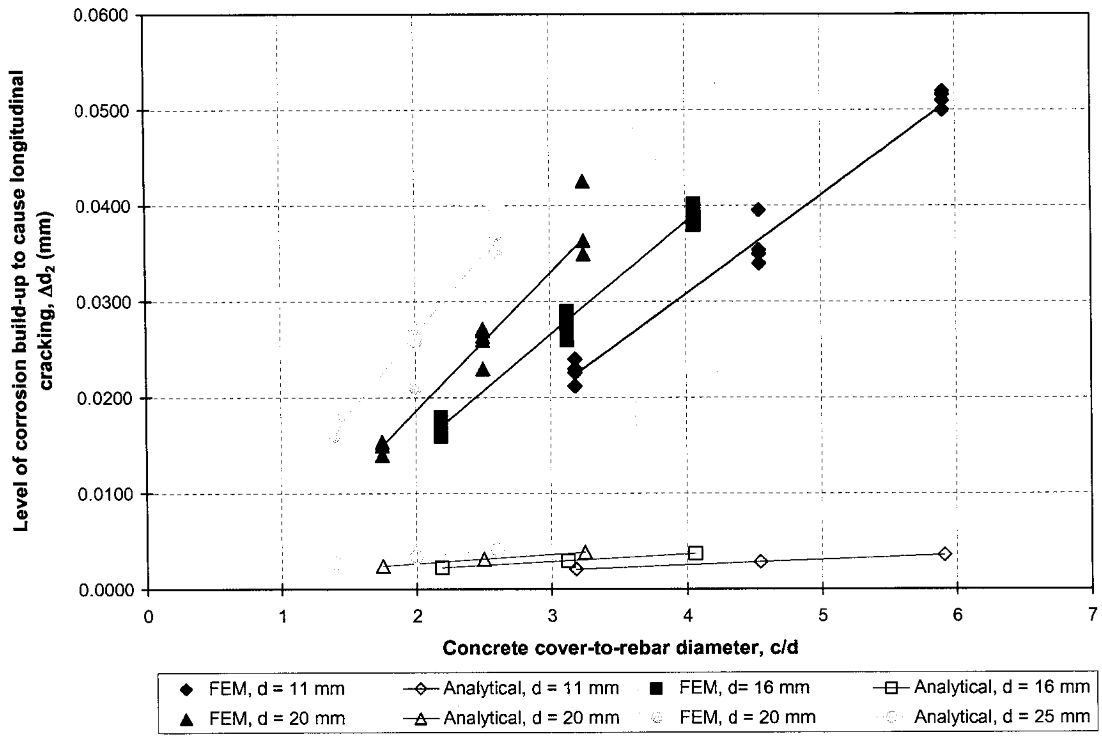

Figure 7.4: Comparison of the level of corrosion build-up to cause longitudinal cracking between the finite element and analytical models

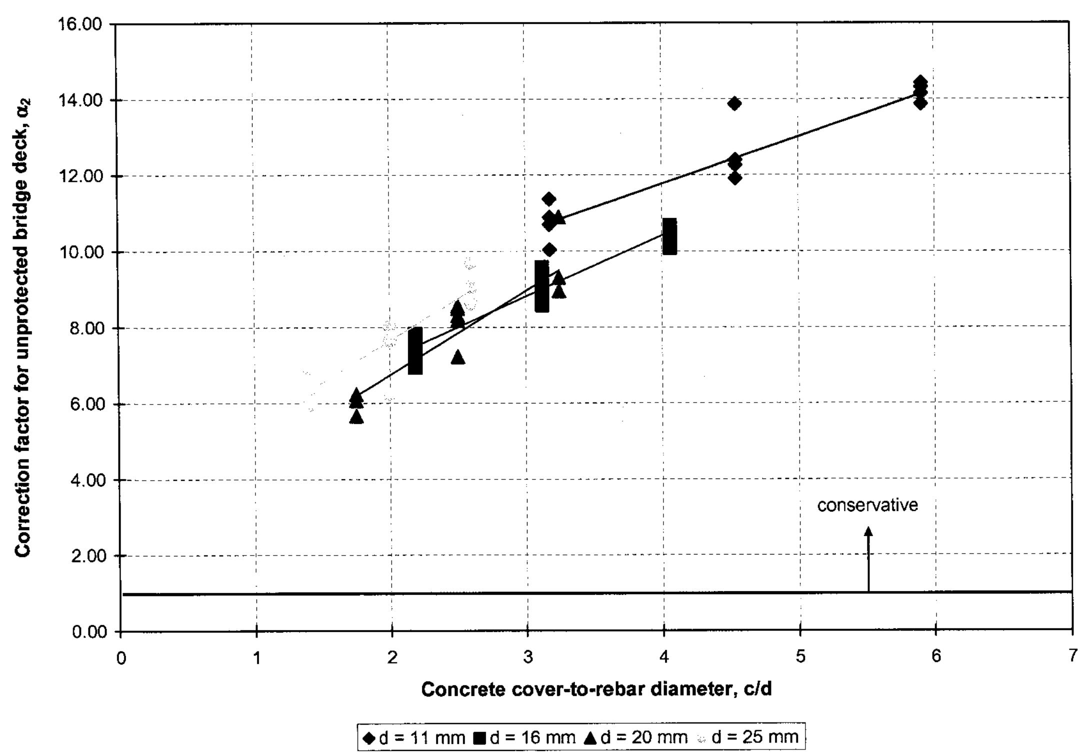

Figure 7.5: Correction factor α_2^u for an unprotected rc bridge deck

The finite element model can carry some tensile stresses after cracking has occurred; on the other hand, the tensile stresses calculated from the analytical model drop to zero after reaching f'_t, since the model does not account for any softening behaviour. The finite element model can therefore accommodate much higher levels of corrosion build-up before cracks reach the surface of the deck.

7.3.2 Rehabilitated rc decks

Figure 7.8, Figure 7.9, and Figure 7.10 present correction factors α_2^r obtained by comparing the finite element results in Chapter 6 to those obtained from Eq. 3.21 for an overlaid rc bridge deck. Since Eq. 3.21 was formulated under the assumption that the concrete cover behaves as a thick-wall cylinder of uniform material, the analytical results reported in the tables were obtained by assuming that the thick-wall cylinder is made of the overlay material.

Table 7.8: Correction factors α_2^r for Δd_2 for an rc bridge deck overlaid with MSC (f'_c = 52 MPa, f'_t = 4.3 MPa, E_c = 33.8 GPa, ν = 0.2)

c (mm)	d (mm)	s (mm)	Δd_2 (mm) (FEM)	Δd_2 (mm) (Eq. 3.21)	α_2^r Δd_2 (FEM) / Δd_2 (3.21)
22	16	86	0.047	0.003	15.43
22	16	86	0.025	0.003	8.21
22	16	86	0.027	0.003	8.86
22	16	86	0.024	0.003	7.88
68	16	150	0.127	0.007	18.14
68	16	170	0.158	0.007	22.57
68	16	290	0.145	0.007	20.72
68	16	310	0.149	0.007	21.29
22	20	86	0.032	0.003	9.42
22	20	100	0.024	0.003	7.07
22	20	120	0.021	0.003	6.18
22	20	170	0.019	0.003	5.59
68	20	150	0.103	0.007	14.22
68	20	170	0.127	0.007	17.53
68	20	290	0.122	0.007	16.84
68	20	310	0.122	0.007	16.84

Table 7.9: Correction factors α_2^r for Δd_2 for an rc bridge deck overlaid with MSC (f'_c = 90 MPa, f'_t = 5.6 MPa, E_c = 44.6 GPa, ν = 0.2)

c (mm)	d (mm)	s (mm)	Δd_2 (mm) (FEM)	Δd_2 (mm) (Eq. 3.21)	α_2^r Δd_2 (FEM) / Δd_2 (3.21)
22	16	86	0.054	0.003	17.72
22	16	100	0.038	0.003	12.47
22	16	120	0.034	0.003	11.16
22	16	170	0.032	0.003	10.50
68	16	150	0.130	0.007	18.57
68	16	170	0.173	0.007	24.72
68	16	290	0.229	0.007	32.72
68	16	310	0.239	0.007	34.15
22	20	86	0.056	0.003	16.49
22	20	100	0.044	0.003	12.95
22	20	120	0.030	0.003	8.83
22	20	170	0.027	0.003	7.95
68	20	150	0.125	0.007	17.25
68	20	170	0.136	0.007	18.77
68	20	290	0.219	0.007	30.23
68	20	310	0.163	0.007	22.50

Table 7.10: Correction factors α_2^r for Δd_2 for an rc bridge deck overlaid with LMC (f'_c = 40 MPa, f'_t = 3.7 MPa, E_c = 29.7 GPa, ν = 0.2)

c (mm)	d (mm)	s (mm)	Δd_2 (mm) (FEM)	Δd_2 (mm) (Eq. 3.21)	α_2^r Δd_2 (FEM) / Δd_2 (3.21)
22	16	86	0.071	0.003	23.30
22	16	100	0.060	0.003	19.69
22	16	120	0.039	0.003	12.80
22	16	170	0.035	0.003	11.49
68	16	150	0.130	0.007	18.57
68	16	170	0.153	0.007	21.86
68	16	290	0.243	0.007	34.72
68	16	310	0.186	0.007	26.57
22	20	86	0.039	0.003	11.48
22	20	100	0.031	0.003	9.13
22	20	120	0.027	0.003	7.95
22	20	170	0.025	0.003	7.36
68	20	150	0.103	0.007	14.22
68	20	170	0.188	0.007	25.95
68	20	290	0.175	0.007	24.15
68	20	310	0.165	0.007	22.77

Corrections factors α_2^r obtained for Δd_2 are much higher for an overlaid rc deck than for an unprotected one (see Figure 7.6). Whereas for low concrete cover-to-rebar diameter ratios (between 1 and 2), both set of analyses for unprotected and overlaid decks show the same correction factor α_2 (around six), the values of α_2 go up to 35 for c/d values greater than 4 for the overlaid deck analyses.

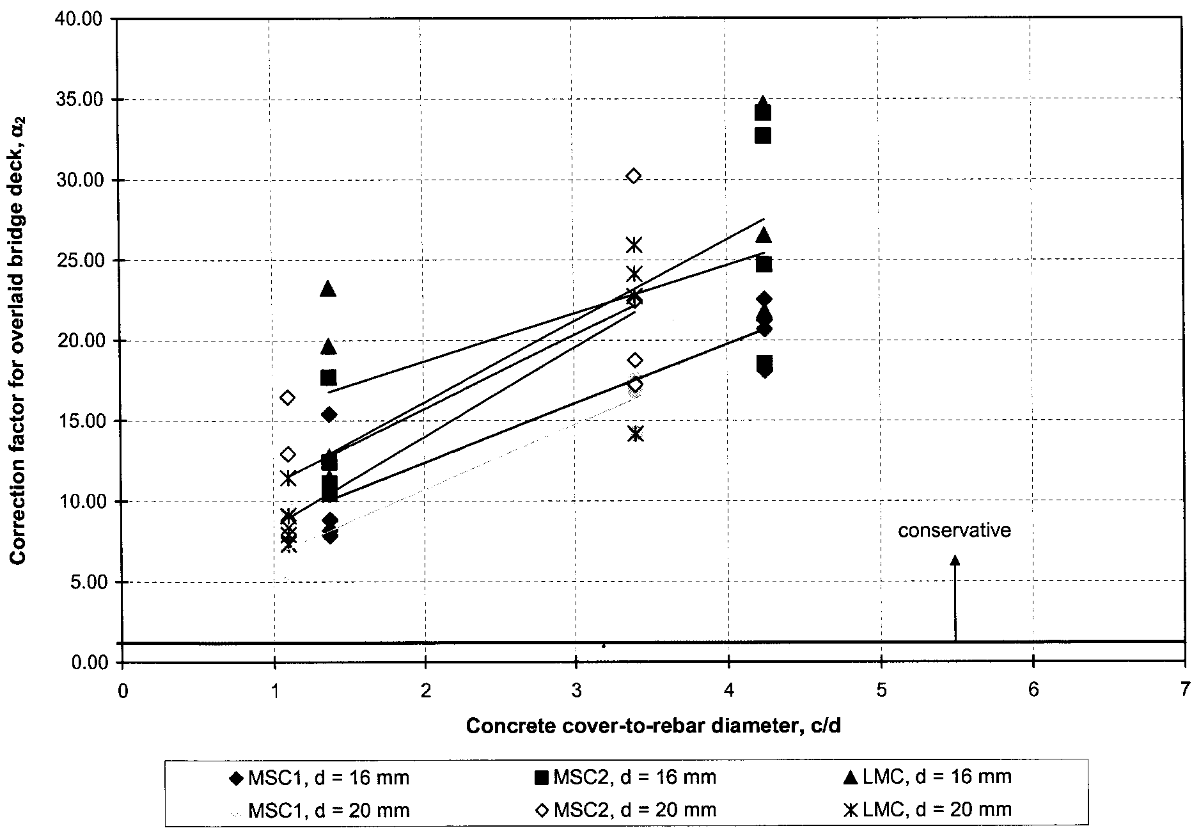

Figure 7.6: Correction factor α_2^r for an overlaid rc bridge deck (MSC1 denotes MSC overlay with f'_c = 52 MPa; MSC2 denotes MSC overlay with f'_c = 90 MPa)

7.4 Spalling

The model for spalling of the concrete cover is formulated from Eq. 3.24 by multiplying it by a correction factor α_3. The proposed model is as follows:

$$\Delta d_3 = \alpha_3 \cdot \frac{(1+\nu)}{E_c} f_t' \frac{(c/d + 0.5)}{(c/d)^2 + (c/d)} \left[d(1-\nu) + 2c(c/d+1) \right] \tag{7.4}$$

The values of α_3 have been obtained by dividing the Δd_3 resulting from the finite element analyses by that calculated from Eq. 3.24. Values of α_3 obtained for an unprotected rc bridge decks are presented in the following subsection. No values were obtained for an overlaid rc bridge deck, since the finite element analyses for this case only showed longitudinal cracking and delamination as the governing failure mechanisms.

7.4.1 Unprotected rc decks

Table 7.11 and Table 7.12 present correction factors α_3^u obtained by comparing the finite element results to those obtained from Eq. 3.24 for an unprotected rc bridge deck. Material properties for the concrete deck are those used in the finite element analyses (f'_c = 30 MPa, f'_t = 1.8 MPa, E_c = 25.7 GPa, ν = 0.2).

Table 7.11: Correction factors α_3^u for Δd_3 for an unprotected rc bridge deck with rebar diameters of 11 and 16 mm

c (mm)	d (mm)	s (mm)	Δd_3 (mm) (FEM)	Δd_3 (mm) (Eq. 3.24)	α_3^u Δd_3 (FEM) / Δd_3(3.24)
35	11	110	0.1430	0.007029845	20.34
35	11	120	0.1720	0.007029845	24.47
35	11	160	0.1980	0.007029845	28.17
50	11	152	0.2400	0.009500751	25.26
50	11	160	0.2650	0.009500751	27.89
50	11	218	0.2840	0.009500751	29.89
65	11	195	0.3250	0.011996395	27.09
65	11	205	0.3530	0.011996395	29.43
65	11	275	0.3600	0.011996395	30.01
35	16	115	0.1170	0.007661636	15.27
35	16	130	0.1360	0.007661636	17.75
35	16	173	0.1580	0.007661636	20.62
50	16	157	0.2600	0.010076895	25.80
50	16	170	0.2610	0.010076895	25.90
50	16	230	0.3230	0.010076895	32.05
65	16	200	0.3310	0.012540526	26.39
65	16	210	0.3300	0.012540526	26.31

Table 7.12: Correction factors α_3^u for Δd_3 for an unprotected rc bridge deck with rebar diameters of 20 and 25 mm

c (mm)	d (mm)	s (mm)	Δd_3 (mm) (FEM)	Δd_3 (mm) (Eq. 3.24)	α_3^u Δd_3(FEM) / Δd_3 (3.24)
35	20	120	0.1750	0.008213252	21.31
35	20	130	0.1680	0.008213252	20.45
35	20	182	0.2360	0.008213252	28.73
50	20	160	0.1830	0.010572839	17.31
50	20	180	0.2190	0.010572839	20.71
50	20	240	0.2980	0.010572839	28.19
65	20	204	0.3270	0.013004294	25.15
65	20	220	0.3320	0.013004294	25.53
65	20	297	0.3580	0.013004294	27.53
35	25	160	0.2020	0.008957143	22.55
35	25	200	0.3320	0.008957143	37.07
50	25	160	0.2030	0.011234043	18.07
50	25	252	0.3580	0.011234043	31.87
65	25	190	0.3030	0.013617676	22.25
65	25	310	0.3780	0.013617676	27.76

The results tabulated in Table 7.11 and Table 7.12 are plotted in Figure 7.7 as a function of the concrete cover-to-rebar diameter ratio c/d. The figure illustrates that Δd_3 obtained from the finite element model is up to thirty times larger to that obtained from the analytical model. Correction factors α_3^u fall between the ranges of 20 to 30 for any value of c/d, as shown in Figure 7.8.

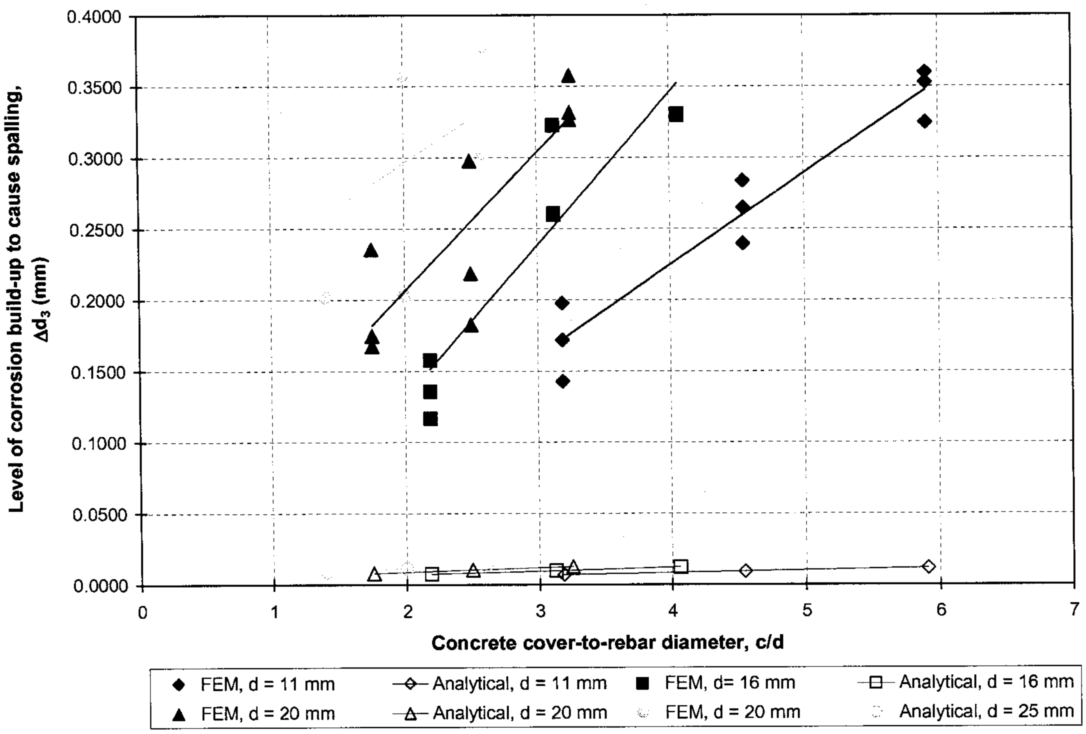

Figure 7.7: Comparison of the level of corrosion build-up to cause spalling between the finite element and analytical models

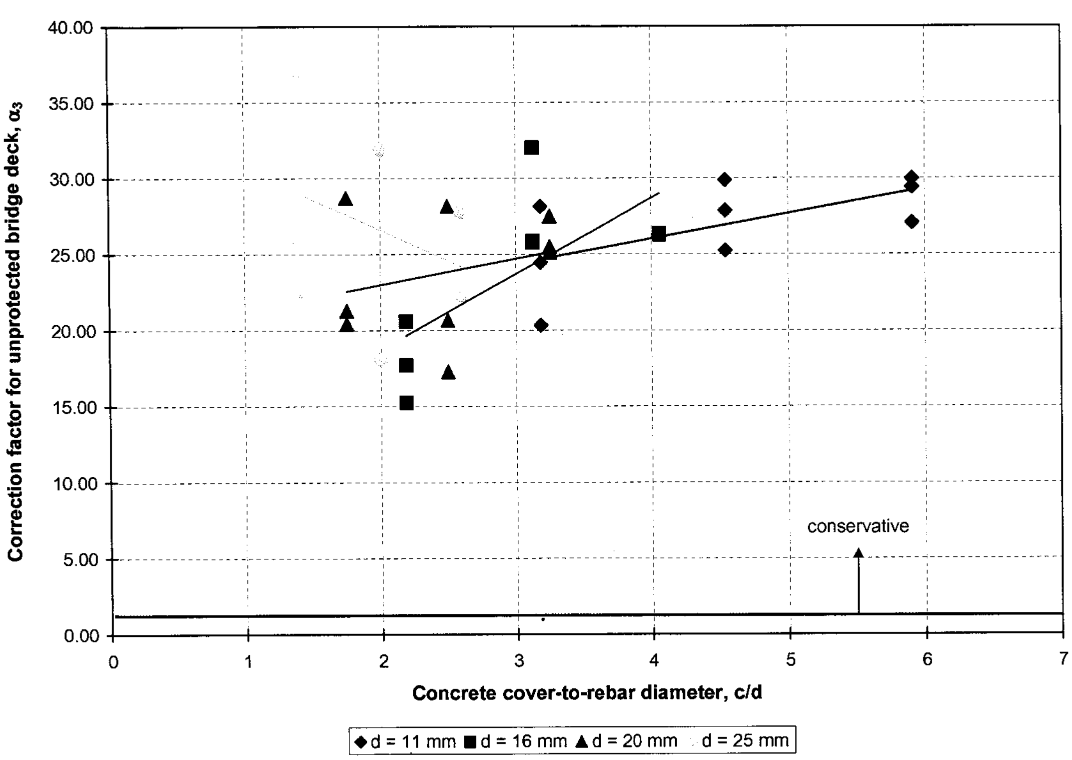

Figure 7.8: Correction factor α_3^u for an unprotected rc bridge deck

7.5 Delamination

The model for delamination of the concrete cover is formulated from Eq. 3.27 by multiplying it by a correction factor α_4. The proposed model is as follows:

$$\Delta d_4 = \alpha_4 \cdot \frac{1}{2}\frac{(1+\nu)}{E_c} f_t^{'} \frac{(s/d)-1}{(c/d)^2+(c/d)}\left[d(1-\nu)+2c(c/d+1)\right] \quad (1.1)$$

The values of α_4 have been obtained by dividing the Δd_4 resulting from the finite element analyses by that calculated from Eq. 3.27. Values of α_4 obtained for both unprotected and rehabilitated rc bridge decks are presented in the following.

7.5.1 Unprotected rc decks

Table 7.13 and Table 7.14 present correction factors α_4^{u} obtained by comparing the finite element results to those obtained from Eq. 3.27 for an unprotected rc bridge deck. Material properties for the concrete deck are those used in the finite element analyses (f'_c = 30 MPa, f'_t = 1.8 MPa, E_c = 25.7 GPa, ν = 0.2).

Table 7.13: Correction factors α_4^u for Δd_4 for an unprotected rc bridge deck with rebar diameters of 11 and 16 mm

c (mm)	d (mm)	s (mm)	Δd_4 (mm) (FEM)	Δd_4 (mm) (Eq. 3.27)	α_4^u Δd_4 (FEM) / Δd_4 (3.27)
35	11	50	0.008	0.003	2.30
35	11	81	0.021	0.006	3.49
35	11	86	0.024	0.007	3.63
35	11	92	0.030	0.007	4.24
35	11	100	0.045	0.008	5.88
35	11	110	0.114	0.009	13.27
35	11	120	0.140	0.009	14.80
35	11	160	0.204	0.013	15.78
50	11	80	0.020	0.006	3.32
50	11	111	0.037	0.009	4.28
50	11	120	0.047	0.009	5.04
50	11	152	0.182	0.012	15.08
50	11	160	0.192	0.013	15.05
50	11	218	0.291	0.018	16.42
65	11	80	0.020	0.006	3.37
65	11	141	0.052	0.011	4.74
65	11	160	0.216	0.013	17.04
65	11	195	0.294	0.016	18.78
65	11	205	0.320	0.017	19.39
65	11	275	0.367	0.022	16.34
35	16	80	0.013	0.006	2.35
35	16	86	0.019	0.006	2.98
35	16	105	0.029	0.008	3.66
35	16	115	0.078	0.009	8.84
35	16	130	0.092	0.010	9.06
35	16	173	0.165	0.014	11.80
50	16	80	0.013	0.006	2.37
50	16	116	0.029	0.009	3.29
50	16	140	0.055	0.011	5.11
50	16	157	0.113	0.012	9.23
50	16	170	0.190	0.013	14.20
50	16	230	0.331	0.019	17.81
65	16	80	0.013	0.005	2.40
65	16	146	0.042	0.011	3.76
65	16	170	0.078	0.013	5.93
65	16	200	0.243	0.016	15.38
65	16	210	0.340	0.017	20.40

Table 7.14: Correction factors α_4^u for Δd_4 for an unprotected rc bridge deck with rebar diameters of 20 and 25 mm

c (mm)	d (mm)	s (mm)	Δd_4 (mm) (FEM)	Δd_4 (mm) (Eq. 3.27)	α_4^u Δd_4 (FEM) / Δd_4 (3.27)
35	20	80	0.011	0.005	1.94
35	20	90	0.016	0.006	2.47
35	20	110	0.025	0.008	3.00
35	20	120	0.035	0.009	3.84
35	20	130	0.048	0.010	4.78
35	20	182	0.240	0.015	16.23
50	20	80	0.011	0.005	2.01
50	20	120	0.029	0.009	3.27
50	20	140	0.039	0.011	3.69
50	20	160	0.072	0.012	5.84
50	20	180	0.161	0.014	11.42
50	20	240	0.306	0.019	15.79
65	20	120	0.023	0.009	2.70
65	20	150	0.038	0.011	3.34
65	20	180	0.048	0.014	3.46
65	20	204	0.174	0.016	10.91
65	20	220	0.263	0.017	15.17
65	20	297	0.350	0.024	14.57
35	25	80	0.009	0.005	1.66
35	25	95	0.018	0.007	2.73
35	25	130	0.036	0.010	3.60
35	25	160	0.085	0.013	6.68
35	25	200	0.342	0.017	20.73
50	25	80	0.008	0.005	1.66
50	25	125	0.027	0.009	3.00
50	25	160	0.175	0.012	14.42
50	25	252	0.362	0.020	17.74
65	25	130	0.022	0.009	2.41
65	25	155	0.037	0.011	3.20
65	25	190	0.225	0.014	15.52
65	25	310	0.390	0.025	15.58

The results tabulated in Table 7.13 and Table 7.14 are plotted in Figure 7.9 as a function of the reinforcing bar spacing-to-rebar diameter ratio s/d. The figure illustrates that Δd_4 obtained from the finite element model is up to twenty times larger to that obtained from the analytical model for values of s/d greater than 20. Correction factors α_4 reduce to around two for s/d values lower than 5 (see Figure 7.10)

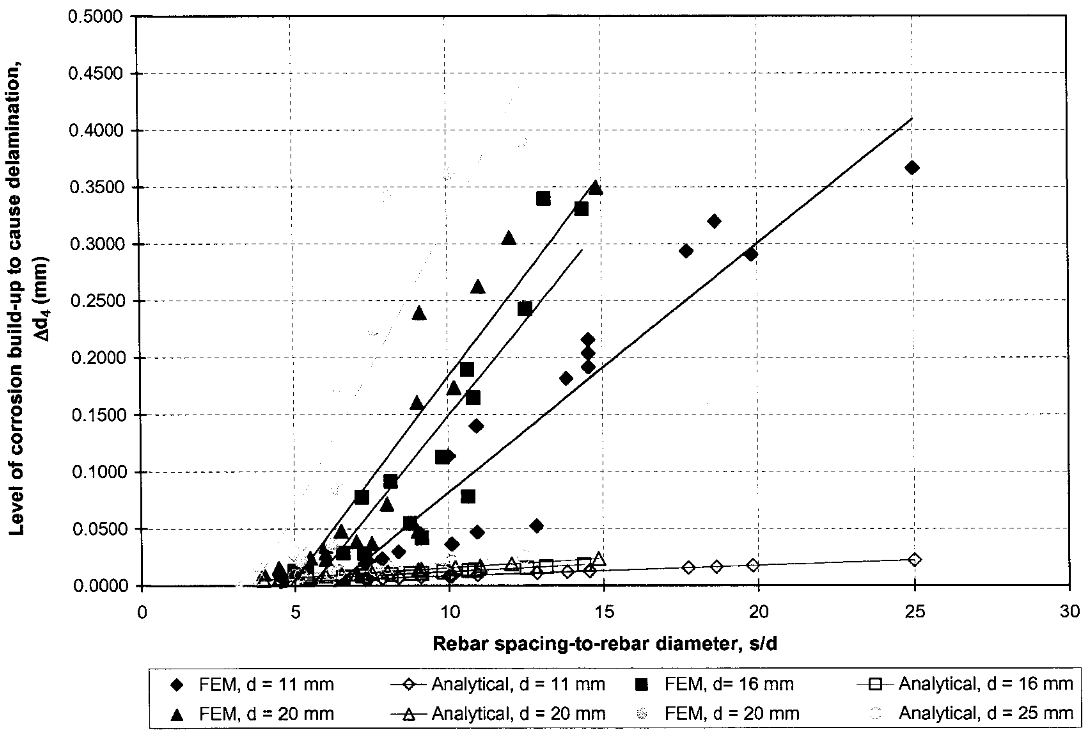

Figure 7.9: Comparison of the level of corrosion build-up to cause delamination between the finite element and analytical models

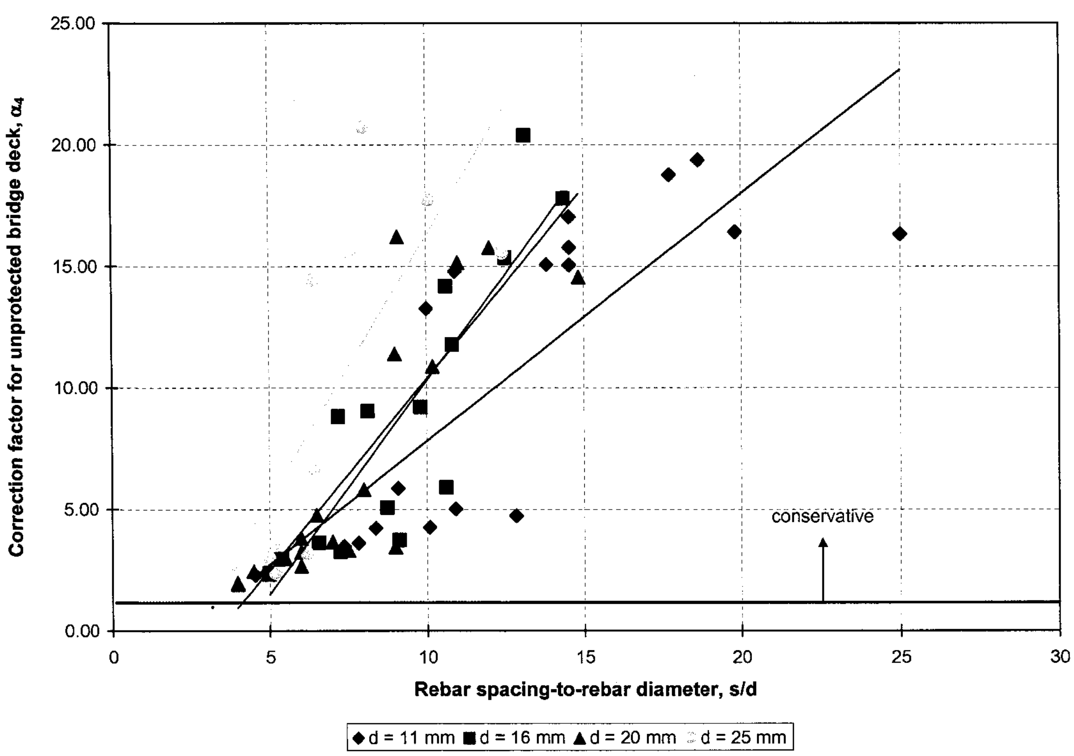

Figure 7.10: Correction factor α_4^u for an unprotected rc bridge deck

7.5.2 Rehabilitated rc decks

Table 7.15, Table 7.16, and Table 7.17 present correction factors α_4^r obtained by comparing the finite element results in Chapter 6 to those obtained from Eq. 3.27 for an overlaid rc bridge deck. Since Eq. 3.27 was formulated under the assumption that the concrete cover behaves as thick-wall cylinder of uniform material, the analytical results reported in the tables were obtained by assuming that the thick-wall cylinder is made of the overlay material.

Table 7.15: Correction factors α_4^r for Δd_4 for an rc bridge deck overlaid with MSC (f'_c = 52 MPa, f'_t = 4.3 MPa, E_c = 33.8 GPa, ν = 0.2)

c (mm)	d (mm)	s (mm)	Δd_4 (mm) (FEM)	Δd_4 (mm) (Eq. 3.27)	α_4^r Δd_4(FEM) / Δd_4(3.27)
22	16	86	0.017	0.012	1.44
22	16	86	0.031	0.012	2.62
22	16	86	0.043	0.012	3.63
22	16	86	0.176	0.012	14.87
68	16	150	0.040	0.021	1.95
68	16	170	0.050	0.024	2.12
68	16	290	0.142	0.042	3.38
68	16	310	0.167	0.045	3.70
22	20	86	0.015	0.012	1.29
22	20	100	0.020	0.014	1.41
22	20	120	0.039	0.018	2.21
22	20	170	0.164	0.027	6.19
68	20	150	0.036	0.020	1.79
68	20	170	0.042	0.023	1.81
68	20	290	0.126	0.042	3.02
68	20	310	0.147	0.045	3.28

Table 7.16: Correction factors α_4^r for Δd_4 for an rc bridge deck overlaid with MSC (f'_c = 90 MPa, f'_t = 5.6 MPa, E_c = 44.6 GPa, ν = 0.2)

c (mm)	d (mm)	s (mm)	Δd_4 (mm) (FEM)	Δd_4 (mm) (Eq. 3.27)	α_4^r Δd_4 (FEM) / Δd_4 (3.27)
22	16	86	0.025	0.012	2.11
22	16	100	0.038	0.014	2.68
22	16	120	0.067	0.018	3.81
22	16	170	0.306	0.026	11.75
68	16	150	0.056	0.021	2.73
68	16	170	0.078	0.024	3.30
68	16	290	0.237	0.042	5.64
68	16	310	0.312	0.045	6.92
22	20	86	0.014	0.012	1.20
22	20	100	0.021	0.014	1.49
22	20	120	0.033	0.018	1.87
22	20	170	0.121	0.027	4.56
68	20	150	0.033	0.020	1.64
68	20	170	0.040	0.023	1.72
68	20	290	0.118	0.042	2.83
68	20	310	0.172	0.045	3.83

Table 7.17: Correction factors α_4^r for Δd_4 for an rc bridge deck overlaid with LMC (f'_c = 40 MPa, f'_t = 3.7 MPa, E_c = 29.7 GPa, ν = 0.2)

c (mm)	d (mm)	s (mm)	Δd_4 (mm) (FEM)	Δd_4 (mm) (Eq. 3.27)	α_4^r Δd_4 (FEM) / Δd_4 (3.27)
22	16	86	0.016	0.012	1.35
22	16	100	0.024	0.014	1.69
22	16	120	0.039	0.018	2.22
22	16	170	0.153	0.026	5.88
68	16	150	0.039	0.021	1.90
68	16	170	0.087	0.024	3.68
68	16	290	0.133	0.042	3.17
68	16	310	0.178	0.045	3.95
22	20	86	0.020	0.012	1.71
22	20	100	0.031	0.014	2.19
22	20	120	0.059	0.018	3.34
22	20	170	0.232	0.027	8.75
68	20	150	0.034	0.020	1.69
68	20	170	0.060	0.023	2.59
68	20	290	0.185	0.042	4.43
68	20	310	0.271	0.045	6.04

Unlike the case of the unprotected rc bridge deck, it was found that correction factors α_4 for an overlaid rc bridge deck are much lower (in the range of 1 to 8) and do not display such a strong dependency to the value of the rebar spacing-to-rebar diameter ratio s/d (see Figure 7.11)

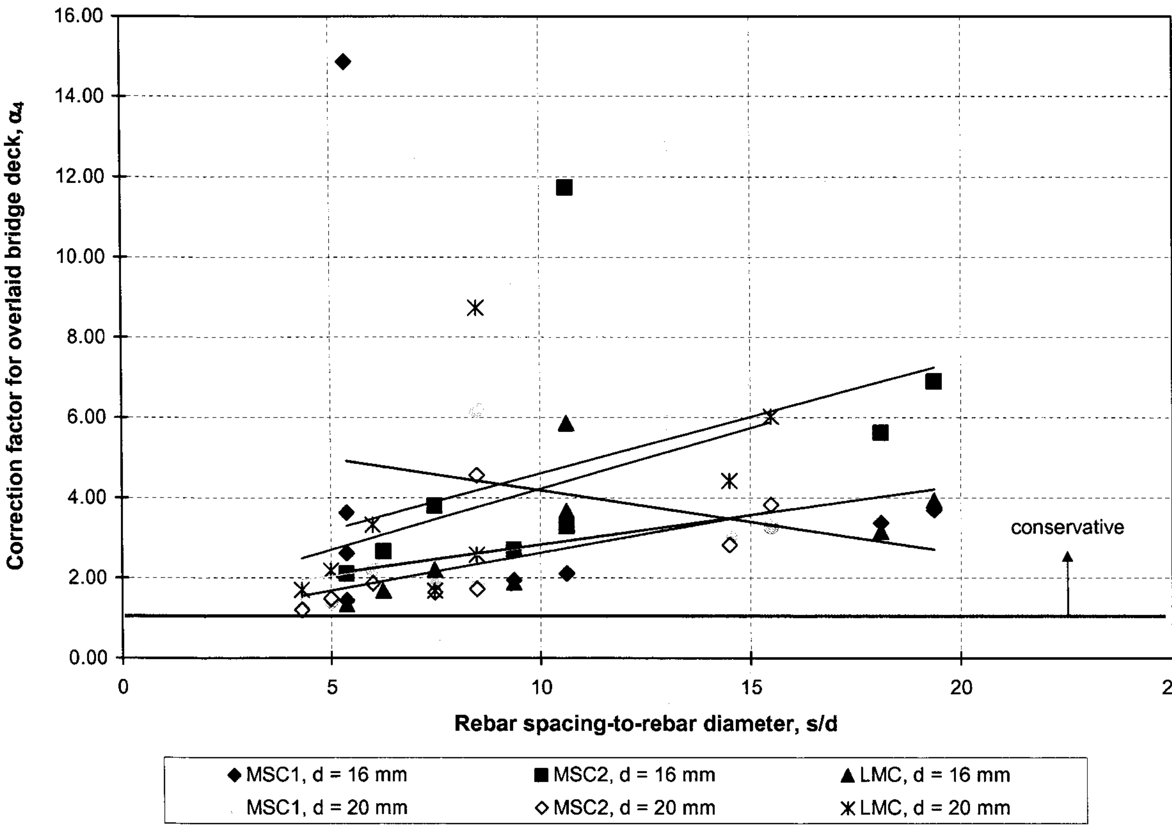

Figure 7.11: Correction factor α_4^r for an overlaid rc bridge deck (MSC1 denotes MSC overlay with f'_c = 52 MPa; MSC2 denotes MSC overlay with f'_c = 90 MPa)

Chapter 8

Concluding remarks

8.1 Summary of findings

A finite element model for simulating corrosion-induced damage in reinforced concrete bridge deck was developed in order to predict the values of corrosion build-up necessary to cause cracking initiation, longitudinal cracking, delamination, and/or spalling. The objective of this study was to present, discuss and evaluate the different failure mechanisms of reinforced concrete bridge decks due to corrosion build-up on the reinforcement as a function of different geometric configurations of the reinforcing bars in the concrete deck cover. It was an objective to establish the relation between the governing design variables of the mechanical problem, namely concrete cover, reinforcing bar diameter and spacing between rebars.

Two kinds of constitutive models for plain concrete, the smeared crack model and the damaged plasticity model, of the ABAQUS/STANDARD material library were used in this study to simulate the nonlinear behavior of the damaged concrete. In the smeared crack model, a Mohr-Coulomb type compression yield surface with a crack detection failure surface was used. When the principal stress components of concrete are predominately compressive, the response of the concrete is modeled by an elastic-plastic theory, using a simple form of yield surface in terms of the first and second stress invariants. An associated flow and isotropic hardening rule are used. For modeling cracking in concrete, damage elasticity is then used. In the damaged plasticity model, the concepts of isotropic damaged elasticity in combination with isotropic tensile and compressive plasticity are used to represent the nonlinear behavior of concrete. It assumes that the main two failure mechanisms are tensile cracking and compressive crushing of the concrete material.

Comparing the two constitutive models in the finite element analysis resulted in almost the same values of corrosion build-up to initiate cracking at the concrete/steel interface; however, when simulating cracking propagation, the damaged plasticity model was more robust from a computational standpoint, since it could accommodate more displacement increments before it encountered numerical difficulties due to the extensive cracking of the concrete cover.

According to St. Venant's Principle, the difference between the stresses caused by statically equivalent load systems is insignificant at distances greater than the largest dimension of the area over which the loads are acting. In this study, corrosion product accumulation was input as displacement increments along the surface of the rebar. Therefore, the effect of corrosion build-up can be seen as a localized effect around the rebar. If restraints are applied to the model sufficiently away from the rebar, they would have little effect on the damage caused by the corrosion build-up. From the finite element analysis conducted, the distance from the centre of the rebar to the restrained boundary, a, was selected as $a \geq 3c$, where c is the concrete cover, and $c \approx 1.4d$ to $c \approx 6d$, d being the rebar diameter.

Based on the finite element model presented in Chapter 4, a parametric study was conducted to investigate the influence of the modulus of elasticity of concrete E_c, the uniaxial compressive strength of concrete f_c', the ratio of the clear cover of the reinforced concrete bridge deck to the diameter of the rebar c/d and the spacing between rebars s on the values of corrosion build-up to cause cracking initiation, longitudinal cracking, delamination and/or spalling of the concrete bridge deck cover.

The different failure mechanisms of the unprotected concrete bridge deck caused by corrosion build-up of the reinforcing bars for different geometric configurations were studied. As the rebar spacing s increased, the obtained failure mechanisms of the rc bridge decks due to corrosion build-up could be classified as follows:

i. delamination, followed by longitudinal cracking

ii. longitudinal cracking, followed by delamination

iii. longitudinal cracking, followed by spalling

It was found that the governing failure mechanisms were sensitive to the lengths of the paths through which cracks developed. Governing failure mechanisms were determined by these lengths evaluated as a function of *c*, *d* and *s*. From the finite element results, it was found that:

1. With the increase of f_c' as well as E_c, the values of the corrosion build-up causing cracking initiation, longitudinal cracking, delamination and spalling of the concrete cover increased too. However, the limiting criteria to determine the different failure mechanisms only depended on *c, d,* and *s*, and they were independent of the strength of the bridge deck cover.
2. The value of corrosion build-up causing cracking initiation $\Delta d_1/2$ was almost not affected by changing *c/d*; however, it was affected by the diameter of the rebar *d*, increasing with an increase in *d*.
3. The values of corrosion build-up causing longitudinal cracking $\Delta d_2/2$ increased as *c/d* increased. If *c/d* remained constant, a higher value of *d* led to a higher value of $\Delta d_2/2$.
4. The values of corrosion build-up causing delamination $\Delta d_4/2$ decreased as *d* increased when *s* was fixed. However, when *d* and *s* were fixed, changing *c/d* had little influence on $\Delta d_4/2$. It was also found that $\Delta d_4/2$ increased as *s* increased when *c* and *d* remained constant.
5. The values of the corrosion build-up causing spalling $\Delta d_3/2$ increased as *c/d* increased. If *c/d* was unchanged, a higher value of *d* led to a higher value of $\Delta d_3/2$.

A comparison of the values of corrosion build-up necessary to cause cracking initiation, longitudinal cracking, delamination and spalling of the reinforced concrete bridge deck obtained from the analytical model presented in Chapter 3 and the finite model presented in Chapter 4 was made. Correction factors were obtained by comparing these two models. It was found that Δd_1 calculated from the finite element model was greater than that calculated from the analytical model. The correction factor for Δd_1 by comparing the finite element model to the analytical model was around 0.96 to 2.17 and decreased as the rebar diameter increased.

As Δd_1, the values of Δd_2, Δd_3 and Δd_4 calculated from the finite element model were greater than those calculated from the analytical model. The correction factor for Δd_2 was around 5.7 to

14, the correction factor for Δd_3 was around 15.3 to 37, and the correction for Δd_4 was around 1.7 to 21.

For modeling an overlaid rc bridge deck, a finite element model similar to that used for the unprotected rc bridge deck was used. It was found that the failure mechanisms of the repaired rc bridge deck as the rebar spacing s increased could also be classified as follows:

i. delamination, followed by longitudinal cracking

ii. longitudinal cracking, followed by delamination

Unlike the unprotected rc bridge deck, after cracking initiation, there were only two damage patterns for an overlaid rc bridge deck: longitudinal cracking and delamination. Here the governing failure mechanisms were also found to depend on the lengths of the paths through which cracks propagate. However, the value of the limiting criterion was higher than that in the unprotected case. This was due to the fact that the repair material had much higher tensile strength than the substrate concrete.

Similar to the unprotected rc bridge deck, it was found that Δd_1 calculated from the finite element model for an overlaid rc bridge deck was greater than that calculated from the analytical model for unprotected reinforced bridge deck. The correction factor for Δd_1 by comparing the finite element model to the analytical model was around 2.0 to 3.4. The correction factor for Δd_2 for an overlaid bridge deck was around 7 to 35, and the correction factor for Δd_4 was around 1.3 to 15.

This study has led to the following conclusions:

i. The proposed finite element model was successful in predicting the different failure mechanisms with different geometric configurations of the reinforcing bars of a reinforced concrete bridge deck.

ii. Corrosion-induced damage modes of the rc bridge deck was a combination of two failure patterns. There were three types damage modes and the actual values of s that led to the different failure modes depended on the actual concrete cover-to-rebar diameter ratio c/d and the rebar spacing-to-rebar diameter ratio s/d. A similar pattern of failure was predicted with the analytical models formulated in Chapter 3.

iii. After cracking initiation, the failure patterns were very sensitive to the lengths of the paths through which cracks developed. The values of the level of corrosion build-up causing longitudinal cracking, $\Delta d_2/2$, and spalling, $\Delta d_3/2$, increased as c/d increased. However, the values of corrosion build-up causing delamination, $\Delta d_4/2$, were found to be dependent on s/d, increasing as s/d increased.

8.2 Recommendations for future work

Modeling corrosion-induced damage in rc bridge decks is a very complex problem, not only because of the nonlinear behavior of cracked concrete, but also because of the uncertainties associated to the corrosion build-up geometry. To enhance model simulation, further work is suggested in the following:

1. Experimental testing of repair materials to better understand their constitutive behavior under load and fracture properties.
2. In this study, only damage due to corrosion build-up around the reinforcement was studied. In reality, the damage is aggravated by other factors, such as live and dead loads, impact and vibration loading, temperature and shrinkage-induced stresses, and freeze-thaw cycles. These factors should also be considered in addition to the corrosion build-up around the reinforcement to better assess damage of rc bridge decks.
3. Corrosion damage of the rc bridge deck is a time-dependent process, not only due to corrosion build-up around the reinforcement varying with time, but also due to the time-dependent deformation characteristic of concrete. For simplicity, this study assumed that corrosion build-up varied linearly with time, and the strain-stress relation of concrete was time-independent. For further study, the corrosion build-up rate as well as the time-dependent behavior of concrete, i.e., creep of concrete, should also be considered to get more realistic results.

References

ACI Committee 318. (1999). "Building Code Requirements for Structural Concrete and Commentary." American Concrete Institute.

ACI Committee 363. (1992). "State-of-the-Art Report on High-Strength Concrete." American Concrete Institute.

ACI Committee 546. (1996). "Concrete Repair Guide." *ACI 546R-96*, American Concrete Institute.

ACI Committee 548. (1994). "Guide for Polymer Concrete Overlays." *ACI 548.5R-94*, American Concrete Institute.

ASCE Task Committee on Concrete and Masonry Structure (1982). "State of the art report on finite element analysis of reinforced concrete."

Bažant, Z. P. (1979). "Physical model for steel corrosion in concrete sea structures-application." *Journal of the Structural Division*, 105(ST6), 1155-1166.

Bažant and Oh. (1983). "Crack Band Theory for Fracture of concrete." *Materials and Structures*, RILEM. V.16 No. 94,1983

Bažant (1988). "Nonlocal Smeared Cracking Model for Concrete Fracture." *Journal of Structural Engineerinl*, ASCE, V. 114, No.11., No. 1988. 2493-2510

Bhushan L. Karihaloo (1995). *Fracture Mechanics and Structural Concrete*, Longman Scientific & Technical. 49-58.

CAN/CSA-S6-00 (2000). *Canadian Highway Bridge Design Code*. National Standard of Canada, CSA International , Toronto, ON, 2000.

CEB-FIP Model Code (1993), Lausanne, Switzerland.

Chidiac, S.E., Noruziaan, B., and Mailvaganam, N. P. (1997) "Service prediction of reinforced concrete repair systems." *Technical report for National Research Council Canada Institute for Research in Construction, Report No. DC961121.1.*

Cope et al (1980) "Modeling of Reinforced Concrete Behaviour for Finite Element Analysis of Bridge slabs." *Numerical Methods for Nonlinear Problems 1* (Taylor C. et al Editors), Pineridge Press, Swansea, 457-470

Dagher, H. J., and Kulendran, S. (1992). "Finite element modeling of corrosion damage in concrete structures." *ACI Structural Journal*, 89(6), 699-708.

de Borst, R. and Nauta. P. (1985). "Non-orthogonal Cracks in a Smeared Finite Element Model." *Engineering Computation* 2, 1985 35-46

de Borst, R. (1987)."Smeared Cracking, Plasticity, Creep and Thermal Loading- a Unified Approach." *Computation Method Application*, 87(62), 89-110

de Borst, R. (2002). "Fracture in quasi-brittle material: a review of continuum damage-based approaches." *Engineering Fracture Mechanics* 69(2002) 95-112.

Hansen, E.J., and Saouma, V.E. (1999). "Numerical Simulation of Reinforced Concrete Deterioration: Part II-- Steel Corrosion and Concrete cracking." *ACI Materials Journal*, 96(3), 331-338.

Herrmann, G., and Kestin, J. (1989). "On the Thermodynamic Foundations of a Damage Theory in Elastic Solids, Cracking and Damage-Strain Localization and Size effect" (J. Mazars et al Editors), 228-232

Hibbit, Karlsson & Sorensen Inc. (2004). "ABAQUS/Standard User's Manual." Pawtucket, Rhode Island.

Hilleborg, A., M. Modeer, and P. E. Petersson, (1976). "Analysis of Crack Formation and Crack Growth in Concrete by Means of Fracture Mechanics and Finite Elements," *Cement and Concrete Research*, vol. 6, 773-782, 1976.

Hsuan-The Hu, Fu-Ming Lin, and Yih-Yuan Jan (2004). "Nonlinear finite element analysis of reinforced concrete beams strengthened by fiber-reinforced plastics." *Composite Structures*, 63 (2004), 271-281

Isenberg J, editor. *Finite Element Analysis of Reinforced Concrete Structures II.* ASCE, New York, 1993. 203-32, 392-401.

Kolmar and Mehlhorn (1984). "Comparison of Shear Stiffness Formulations For CRaked Reinforced Concrete Elemnet." *International Conference on Computer-Aided Analysis and Design of Concrete Structures* (Damjanie F et al Editors), Part 1 Pineridge Press, Swansea, 133-147.

Lee, J., and G. L. Fenves, (1998)."Plastic-Damage Model for Cyclic Loading of Concrete Structures," *Journal of Engineering Mechanics*, vol. 124, no. 8, 892-900.

Liu, Y., and Weyers, R.E. (1998)."Modeling the time-to-corrosion cracking in chloride contaminated reinforced concrete structures." *ACI Materials Journal*, 95(3), 675-681.

Lubliner, J., J. Oliver, S. Oller, and E. Oñate, (1989). "A Plastic-Damage Model for Concrete," *International Journal of Solids and Structures*, vol. 25, 299-329.

Joseph W. Tedescoa, J. Michael Stallings, Mahmoud El-Mihilmy (1999). " Finite element method analysis of a concrete bridge repaired with fiber reinforced plastic laminates." *Computers and Structures* 99 (72), 379-407.

Martín-Pérez, B. (1999). "Service Life Modelling of R.C. Highway Structures Exposed to Chlorides," Ph.D., University of Toronto, Toronto.

McLeish, A. (1986). "Cracking due to corrosion." *Technical Note No. 1632*, Taywood Engineering.

Molina, F. J., Alonso, C., and Andrade, C. (1993). "Cover cracking as a function of bar corrosion: part 2 - numerical model." *Materials and Structures*, 26, 532-548.

Morinaga, S. (1988). "Prediction of service lives of reinforced concrete buildings based on the rate of corrosion." *Special report No. 23*, Institute of Technology, Shimuzu Corporation.

Neville, A. M. (1981). *Properties of Concrete*, Longman Scientific & Technical.

Newhouse, C.D., and Weyers, R.E. (1996). "Modeling the measured time to corrosion cracking." in *Techniques to Assess the Corrosion Activity of Steel Reinforced*

Concrete Structures, ASTM STP 1276, N.,S. Berke, E. Escalante, C.K. Nmai, and D. Whiting (Editors),3-22

Ngo, D. and Scordelis, A.C. (1967). "Finite element analysis of reinforced concrete beams." *ACI Structural Journal* 64(14), 152–163.

Noghabai, K. (1996). "Environmental effects on bond in reinforced concrete structures." in Durability of Building Material and Components 7 (Vol.1), C. Sjostrom (Editor), E & FN Spon, London, UK, 605-614

Rashid, Y.R. (1968). "Analysis of prestressed concrete pressure vessels." *Nuclear Engineering and Design* 7(4), 334–344.

Reich, Cervenka, and Saouma, (1997) "MERLIN, A Three-Dimensional Finite Element Program Based on a Mixed-Iterative Solution Strategy for Problems in Elasticity, Plasticity, and Linear and Nonlinear Fracture Mechanics." *Technical Report*, EPRI, Palo Alto, Calif.

Rosenberg, A., Hansson, C. M., and Andrade, C. (1989). "Mechanisms of corrosion of steel in concrete." Materials Science of Concrete I, J. Skalny, ed., Westerville, OH, 285-313.

Saenz, LP. (1964) "Discussion of 'Equation for the stress-strain curve of concrete' by Desayi P, Krishnan S." *ACI Structural Journal*, 64(61), 1229-1235.

Schlangen, E. (1993). *Experimental and Numerical Analysis of Fracture Processes in Concrete*, Dissertation, Delft University of Technology, Delft

Suidan, M. and Schnobrich, W.C. (1973). "Finite Element Analysis of Reinforced Concrete", *Journal of Structural Engineerinl*, ASCE, V. 99,1973, 2109-2122

Joseph W. Tedescoa, J. Michael Stallings, Mahmoud El-Mihilmy (1999) "Finite element method analysis of a concrete bridge repaired with fiber reinforced plastic laminates"

Computers and Structures 72 (1999) 379-407

Tepfers, R. (1979). "Cracking of concrete cover along anchored deformed reinforcing bars." *Magazine of Concrete Research*, 31(106), 3-12.

Tepfers, R. (1982). "Tensile lap splices with confining reinforcement." Bond in Concrete, P. Bartos, ed., London, 318-330.

Timoshenko, S. (1956). *Strength of Materials. Part II: Advanced Theory and Problems.*, Princeton, New Jersey.

van Mier, J.G.M. (1991). "Mode-I fracture of concrete: discontinuous crack growth and crack interface grain bridging." *Cement and Concrete Research* 21(1991), 1–15.

Vecchio, F. J. and Collins, M.P. (1982). "The response of reinforced concrete to in-plane shear and normal stresses." Report No. 82-03, Department of Civil Engineering , University of Toronto, Canada

Vecchio, F. J. (1989). "Nonlinear finite element analysis of reinforced concrete membranes." *ACI Structural Journal*, 89(2), 26-35

Vecchio, F. J., and Bucci, F. (1999). "Analysis of repaired reinforced concrete structures," *Journal of Structural Engineering,* 125(6), 380-407.

Weyers et al (1993) *Concrete Bridge Protection, Repair, and Rehabilitation Relative to Reinforcement Corrosion: A Methods Application Manual*, SHRP-S-360, Strategic Highway Research Program, National Research Council.

Weyers , R.E. (1998) "Service life model for concrete structures in chloride-laden environments." *ACI Materials Journal,* 95(4),445-453

Williamson, S. J., and Clark, L. A. (2000). "Pressure required to cause cover cracking of concrete due to reinforcement corrosion." *Magazine of Concrete Research*, 52(6), 455-467.

Yokozeki et al. (1997). " A rational model to predict the service life of RC structures in marine environment." in *Durability of Concrete, ACI SP-170 (Volume 1)*, V.M. Malhotra(Editor), ACI, Detroit,777-799

Zienkiewicz, O.C., and Taylor, R.L. (2000). *The finite element method, Vol. 2*, Oxford ; Boston ; Butterworth-Heinemann.